UNIVERSITY OF CALIFORNIA SAN DIEGO

SAN DIEGO STATE UNIVERSITY

Transcriptional Profiling of Memory in Cardiac Interstitial Cells and Pulmonary Response to Vaping

A dissertation submitted in partial satisfaction of the

requirements for the degree

Doctor of Philosophy

in

Biology

by

Oscar Enrique Hernandez Echeagaray

Committee in charge:

University of California San Diego

Professor Barry Grant

Professor Åsa Gustafsson

San Diego State University

Professor Mark A. Sussman, Chair

Professor Faramarz Valafar

Professor Robert Zeller

2022

The dissertation of Oscar Enrique Hernandez Echeagaray is approved, and it is acceptable in quality and form for publication on microfilm and electronically.

_____

_____

_____

_____

_____

Chair

University of California San Diego

San Diego State University

2022

DEDICATION

I would like to dedicate this dissertation to the noteworthy individuals whose support, influence and impact in my life made it possible for me to move forward towards completion even in the darkest of times. Crystal Goodman who has been a “sister in the time of adversity” and whose long friendship, support and positive attitude helps me believe that everything is possible. Eric Bredesen whose patience, love and unconditional support continues to be motivate me to this day. Valerie McElroy whose unique perspectives and thirst for knowledge adds nuance to any subject regardless how complex. Keren Gutierrez for the continuous interest and care displayed weekly, but particularly in the times of crisis. Jack Tung for the professional advice and support. Pamuela Aaliyah Halliwell for your sound advice and for always looking after my emotional health. Tim Kosloski for your long standing friendship, and always helping me to get out of my comfort zone.

To my parents Oscar Hernandez Bello and Raquel Echeagaray Jimenez for their examples of work ethics, diligence and moral resolution which molded me into the person I am today and inspired me to set improving standards in different aspects of my life. To my sisters Raquel and Linda Hernandez Echeagaray.

To all who have been part of this journey with me: Thank you for your support and faith in me.

EPIGRAPH

"For an abundance of wisdom brings an abundance of vexation,

So that whoever increases knowledge increases pain"

Ecclesiastes 1:18

TABLE OF CONTENTS

LIST OF ABBREVIATIONS

RNA	Ribonucleic acid
RNA-Seq	RNA Sequencing
sc/snRNA-Seq	Single-cell and nuclei RNA sequencing
c-kit	Tyrosine-protein kinase Kit or CD117
cCICs	cKit+ cardiac interstitial cells
SASP	Secretory Associated Senescence Phenotype factors
LVAD	Left Ventricle Assisting Device
Vst	Variance Stabilizing Transformation
UMI	Unique Molecular Identifier
PC	Principal Component
DEG	Differentially Expressed Genes
GO	Gene Ontology
FGF2	Fibroblast Growth Factor 2
GLB1	Beta galactosidase 1
HGF	Hepatocyte Growth Factor
KEGG	Kyoto Encyclopedia of Genes and Genomes
MAPK	Mitogen-activated protein kinases pathway
ECM	Extracellular Matrix
Wnt	Wingless-related integration site
UMAP	Uniform Manifold Approximation and Projection
E-cig	Electronic Cigarette
EVALI	E-cig or vaping product use-associated lung injury
CVD	Cardiovascular Disease
ARDS	Acute Respiratory Distress Syndrome
PG/VG	Propylene Glycol/Vegetable Glycerin
FMD	Flow-Mediated Dilation
VEGF	Vascular Endothelial Growth Factor

TLR9	Toll-like receptor 9
ROS	Reactive Oxygen Species
DHE	Dihydroethidium
eNOS	Endothelial Nitric Oxide Synthase
NOX2	NADPH Oxidase Subunit 2
iPSC	Induced Pluripotent Stem Cell
MYLK	Myosin Light Chain Kinase
TNNI3	Troponin I3
AMPK	AMP-activated protein kinase
ACC	Acetyl-CoA carboxylase
MCA	Mouse Cell Atlas
VAPI	Vaping-Associated Pulmonary Injury
ECAD	Epithelial-cadherin
Aq5	Aquaporin 5
DCs	Dendritic Cells
NK cells	Natural Killer Cells
AT1	Alveolar Cells Type 1
AT2	Alveolar Cells Type 2
NV sample	Non-Vaped sample
V sample	Vaped sample
THC	Tetrahydrocannabinol
MAST	Model-based Analysis of Single-cell Transcriptomics
EF	Ejection Fraction
FS	Fractional Shortening
LV_Mass	Left Ventricular Mass
LV_Vold	Left Ventricular Volume diastole
LV_Vols	Left Ventricular Volume systole
LVIDd	Left Ventricular Interior Diameter diastole

LVIDs	Left Ventricular Interior Diameter systole
IVSd	Intraventricular Septum diastole
IVSs	Intraventricular Septum systole
LVPWd	Left Ventricular Posterior Wall diastole
LVPWs	Left Ventricular Posterior Wall systole
H&E	Harris Hematoxylin and Eosin-Phloxine
PAS	Periodic Acid Schiff
RAGE	Receptor for Advanced Glycation End products
IL-6	Interleukin 6
IL-1B	Interleukin 1B
HMGB1	High mobility group box protein 1
FN	Fibronectin

LIST OF FIGURES

LIST OF TABLES

ACKNOWLEDGEMENTS

First, I would like to acknowledge and express my gratitude to my mentor, Dr. Mark A. Sussman, for his continuous support, and guidance. The warm welcome and rigorous environment I found in the Sussman group, let me develop personally and professionally. The mentorship, resources, liberty and backing you provided throughout the years allowed me to advance my career as a scientist with my ingenuity and willingness as the only limitations. Choosing his lab was one of the best decisions I could have taken. Thanks for taking a chance on me.

I would like to thanks my committee members, Dr. Robert Zeller, Dr. Faramarz Valafar, Dr. Åsa Gustafsson and Dr. Barry Grant. Your guidance, invaluable input, and expertise is greatly appreciated. I feel honored to have you as part of my committee.

I would like to acknowledge the National Institute of Health and San Diego State University, for financial support of my research. I would also like to extent my gratitude to CMB Joint Doctoral Administrator Patricia Swinford, Director of the SDSU/UCSD Joint Doctoral Program Dr. Marina G. Kalyuzhnaya and the SDSU Biology Department.

To current and past members of the Sussman lab and the G-unit, thanks for creating a harmonious and joyful work environment. Special thanks to Dr. Natalie Gude for her trust, support and wisdom. Dr. Joi Weeks thank you for your resilience and the legacy that continues to motivate me and former members of the G-unit. Thanks to the G-Unit Christina Payne, Kristine Nguyen and Nick Vallez for always making research an enjoyable experience. Special thanks to current members of the Sussman Lab Carolina Esquer, Fareheh Firouzi, Clarissa Savko, Grant Shain, Andrea Gallo and all the undergrads who continue to move forward even through the worst of a pandemic. I have felt fortunate of working with all of you.

Chapter 1, with slight modifications, is a reprint of the material as it appears in Regenerative Medicine, Vol. 14, No. 9. Transcribing the heart: Faithfully interpreting cardiac transcriptional insights. Echeagaray Oscar and Sussman Mark Alan. The dissertation author was the primary author and investigator on this manuscript.

Chapter 2, with slight modifications, is a reprint of the material as it appears in Genomics, Vol. 113, Issue 6, 2021. Transcriptional features of biological age maintained in human cultured cardiac interstitial cells. Oscar Echeagaray, Taeyong Kim, Alex Casillas, Megan Monsanto, and Mark Sussman. The dissertation author was the primary author and investigator on this manuscript.

Chapter 3, with slight modifications, is a reprint of the material as it will appear in Current Opinion in Cardiology, 2022. Cardiovascular consequences of vaping. Oscar Echeagaray, Clarissa Savko, Andrea Gallo, and Mark Sussman. The dissertation author was the primary author and investigator on this manuscript.

Chapter 4, with slight modifications, is a reprint of the material as it appears in Life Science Alliance, Vol. 5, No. 2, 2021. Fundamentals of vaping-associated pulmonary injury leading to severe respiratory distress. Carolina Esquer, Oscar Echeagaray, Fareheh Firouzi, Clarissa Savko, Grant Shain, Pria Bose, Abigail Rieder, Sophie Rokaw, Andrea Witon-Paulo, Natalie Gude, Mark A Sussman. The dissertation author was the primary co-author and investigator on this manuscript.

VITA

2022	Doctor of Philosophy, University of California San Diego and San Diego State University
2021-2022	Research Fellow, San Diego State University
2019-2022	Research Specialist II, San Diego State University
2018-2021	Teaching Associate, San Diego State University
2016-2018	Scholar Research, San Diego State University
2015-2016	Research Assistant, San Diego State University
2011	Master of Science, Research Institute in Nutrition and Development (CIAD), Mexico
2008	Bachelor of Science, Technologic Institute of Mazatlan, Mexico

PUBLICATIONS

Echeagaray O, Savko C, Gallo A, Sussman M. 2022. "Cardiovascular consequences of vaping". Current Opinions in Cardiology. (In press)

Esquer, C., **Echeagaray, O**., Firouzi, F., Savko, C., Shain, G., Bose, P., Rieder, A., Rokaw, S., Witon-Paulo, A., Gude, N. & Sussman, M. A. Fundamentals of vaping-associated pulmonary injury leading to severe respiratory distress. Life Sci. Alliance 5, e202101246 (2022).

Echeagaray, O., Kim, T., Casillas, A., Monsanto, M. & Sussman, M. Transcriptional features of biological age maintained in human cultured cardiac interstitial cells. Genomics 113, 3705–3717 (2021).

Monsanto, M. M., Wang, B. J., Ehrenberg, Z. R., **Echeagaray, O**., White, K. S., Alvarez, R., Fisher, K., Sengphanith, S., Muliono, A., Gude, N. A. & Sussman, M. A. Enhancing myocardial repair with CardioClusters. Nat. Commun. 11, 1–20 (2020).

Huang, C., Mendez, N., **Echeagaray, O. H**., Weeks, J., Wang, J., Yao, S., Blair, S. L., Gude, N., Trogler, W. C., Carson, D. A., Hayashi, T. & Kummel, A. C. Immunostimulatory TLR7 Agonist-Nanoparticles Together with Checkpoint Blockade for Effective Cancer Immunotherapy. Adv. Ther. 3, 1900200 (2020).

Echeagaray, O. & Sussman, M. A. Transcribing the heart: faithfully interpreting cardiac transcriptional insights. Regen. Med. 14, 805–810 (2019).

Huang, C.-H., Mendez, N., **Echeagaray, O. H**., Weeks, J., Wang, J., Vallez, C. N., Gude, N., Trogler, W. C., Carson, D. A., Hayashi, T. & Kummel, A. C. Conjugation of a Small-Molecule TLR7 Agonist to Silica Nanoshells Enhances Adjuvant Activity. ACS Appl. Mater. Interfaces 11, 26637–26647 (2019).

Wang, J., Huang, C., **Echeagaray, O. H**., Amirfakhri, S., Blair, S. L., Trogler, W. C., Kummel, A. C. & Chen, C. C. Microshell Enhanced Acoustic Adjuvants for Immunotherapy in Glioblastoma. Adv. Ther. 1900066, 1900066 (2019).

Broughton, K., Korski, K., **Echeagaray, O**., Adamson, R., Dembitsky, W., Lu, Z., Schaefer, E. & Sussman, M. A. Safety profiling of genetically engineered Pim-1 kinase overexpression for oncogenicity risk in human c-kit+ cardiac interstitial cells. Gene Ther. (2019) doi:10.1038/s41434-019-0084-5.

Broughton, K. M., Khieu, T., Nguyen, N., Rosa, M., Mohsin, S., Quijada, P., Wang, B. J., **Echeagaray, O. H**., Kubli, D. A., Kim, T., Firouzi, F., Monsanto, M. M., Gude, N. A., Adamson, R. M., Dembitsky, W. P., Davis, M. E. & Sussman, M. A. Cardiac interstitial tetraploid cells can escape replicative senescence in rodents but not large mammals. Commun. Biol. 2, 205 (2019).

Korski, K. I., Kubli, D. A., Wang, B. J., Khalafalla, F. G., Monsanto, M. M., Firouzi, F., **Echeagaray, O. H**., Kim, T., Adamson, R. M., Dembitsky, W. P., Gustafsson, Å. B. & Sussman, M. A. Hypoxia Prevents Mitochondrial Dysfunction and Senescence in Human c-Kit + Cardiac Progenitor Cells. Stem Cells (2019) doi:10.1002/stem.2970.

Kim, T., **Echeagaray, O. H**., Wang, B. J., Casillas, A., Broughton, K. M., Kim, B. H. & Sussman, M. A. In situ transcriptome characteristics are lost following culture adaptation of adult cardiac stem cells. Sci. Rep. 8, 1–9 (2018).

Hernández-Echeagaray O.E., Hernández-Cornejo R., Harfush-Meléndez M. and Garcia- Gasca A. 2012. Evaluation of Sex Ratios of the Olive Ridley Sea Turtle (Lepidochelys olivacea) on the Arribada Nesting Beach, La Escobilla, Mexico. Marine Turtle Newsletter 133: 12-16

HONORS AND AWARDS

2021-2022 University Graduate Fellowship

2018-2022 Supplement to Promote Diversity in Health-Related Research (PA-18-586)

2018 Laser Capture Microdisection Workshop Training Award

2009-2011 Postgraduate Fellowship by the National Counsel of Science and Technology (CONACyT)

2004-2008 Academic Achievement Scholarship by the Secretary of Public Education (SEP)

SCIENTIFIC PRESENTATIONS

2021 Transcriptional features of biological age maintained in cultured cardiac interstitial cells. AHA Scientific Sessions 2021

2021 Transcriptional features of biological age maintained in cultured cardiac interstitial cells. AHA Basic Cardiovascular Sciences 2021

2018 Tridimensional clustering enhances preservation of both transcriptional identity and heterogeneity for adult cardiac stem cells. AHA Scientific Sessions 2018: Chicago

2018 In situ transcriptome characteristics are lost following culture adaptation of adult cardiac stem cells. Alternative Muscle Club Conference 2018: San Diego

2018 Localized immune transcriptional response to intratumorally administrated TLR7 agonist conjugates. Experimental Biology Conference 2018: San Diego

2018 Transcriptional Impact of CT26 Secretions on RAW 264.7 cells Toll-Like Receptor Response. San Diego State University Student Research Symposium

2017 Developing a Reliable Readout of TLR 7 Activation via Cytokine and Chemokine Transcript Levels. San Diego State University Student Research Symposium

2017 Nanoshells Enabled Tumor Ablation in Combination with Immunotherapy. San Diego State University/UC San Diego Moores Cancer Center Partnership Meeting

FIELDS OF STUDY

Major Field: Cell and Molecular Biology

ABSTRACT OF THE DISSERTATION

Transcriptional Profiling of Memory in Cardiac Interstitial Cells and Pulmonary Response to Vaping

by

Oscar Enrique Hernández Echeagaray

Doctor of Philosophy in Biology

University of California San Diego, 2022

San Diego State University, 2022

Professor Mark A. Sussman, Chair

Information technology continues to shape and transform biological research. Bioinformatic research and methods are as diverse and divergent as the biological issues aimed to solved, with RNA sequencing becoming a prominent tool to derive key breakthroughs. This dissertation capitalizes on the adoption of transcriptional platforms and various bioinformatics

analysis to comprehend biological "memory" of cells expanded *ex vivo* for therapeutic approaches and evaluate spatial lung reprograming in a vaping-induced pulmonary injury inhalation model.

Ex vivo expansion of cells is necessary in regenerative medicine to generate large populations for therapeutic use. Adaptation to culture conditions prompt an increase in transcriptome diversity and decreased population heterogeneity in cKit+ cardiac interstitial cells (cCICs). The "transcriptional memory" influenced by cellular origin remains unexplored and is likely to differ between neonatal versus senescent input cells undergoing culture expansion. The work presented in this dissertation demonstrates that age, pathology and the cellular stress associated to the in vivo tissue microenvironment persist after culture adaptation, influencing targets of 1) cell cycle, 2) senescence associated secretory phenotype (SASP), 3) RNA transport, and 4) ECM-receptor/fibrosis.

Vaping continues to increase worldwide. Promoted as a "healthier" alternative to traditional smoking, emerging evidence indicates "healthier" should not be confused with "harmless". Findings in this dissertation demonstrate pulmonary consequences of vaping after chronic direct inhalation exposure. Profound pathological changes to upper airway, lung tissue architecture, and cellular structure are evident within 9 week of exposure. Marked histologic changes include increased parenchyma tissue density, cellular infiltrates proximal to airway passages, alveolar rarefaction, increased collagen deposition, and bronchial thickening with elastin fiber disruption. Transcriptional reprogramming includes significant changes to gene families coding for xenobiotic response, glycerolipid metabolic processes, and oxidative stress. This vaping-induced pulmonary injury model demonstrates mechanistic underpinnings of vaping-related pathologic injury.

Novel technologies are required to circumvent limitations associated with basic cardiopulmonary biology. Transcriptional profiling platforms continues to produce data essential for advancement of therapeutic approaches. Collectively, studies in this dissertation holds the potential to improve in vitro expansion protocols critical for adoptive transfer approaches, restore transcriptional phenotypes in vivo and ultimately to improve efficiency of therapeutic approaches after vaping or cardiac injury.

CHAPTER 1
Transcribing the heart: Faithfully interpreting cardiac transcriptional insights

1.1 The rise of bioinformatics

Information technology has shaped our society in multiple fronts, particularly in the field of regenerative medicine. Coalescence of biology and informatics continues to have a broad impact, from revolutionizing the way science is communicated to the experimental approaches used to gain insight in the biomedical field. The amount of biological data generated today is unprecedented, with sources ranging from sequencers to smartwatches. The formal hybridization of computer science, information engineering and statistics to analyze and interpret biological data is known as bioinformatics. Because of this wide-range definition, bioinformatic research and methods are as diverse and divergent as the biological issues they are resolving, with RNA sequencing being a prominent tool to develop transcriptional datasets and derive key breakthroughs in the field of regenerative medicine. Considering the limited reparative capacity of the adult mammalian heart, concentrated efforts have focused upon gathering bioinformatic knowledge to advance regenerative medicine in this information age. Transcriptional profiles provide suitable phenotypical readouts critical for understanding basic cell biology necessary to improve clinical efficacy of cardiogenic therapeutic approaches after injury.

In the last few years key contributions have explored the cardiac transcriptome (See Table 1.1). Myocardial subpopulations (myocytes, interstitial cells, endothelial cells, fibroblasts, leucocytes) have been transcriptionally and epigenetically profiled at different stages of development at baseline and following myocardial infarction[1]. Effects of topological changes which take place after injury on cardiac fibroblast have been described in conjunction with the chromatin states associated[2]. The cell surface receptome of cardiac progenitor cells has been characterized using RNA sequencing (RNA-Seq) and proteomic profiling[3,4]. These approaches provide valuable insights but are limited by selective isolation strategies or indirect transcriptome

flattening as a result of bulk RNA isolation approaches. Complex biological systems such as the myocardium possess a cellular heterogeneity spectrum across multiple distinct populations that can only be revealed by single cell level analyses.

1.2 Analyzing cardiac heterogeneity

Pioneering approaches to tackle cardiac heterogeneity used single cells qPCR to study cardiac fibroblasts[5]. Massively parallel transcriptional profiling of individual cells by single-cell RNA-Seq (scRNA-Seq) unmasks heterogeneity concealed by bulk sequencing of population averages and the limitations of sc-qPCR. Implementation of scRNA-Seq has been used to infer cell lineages, identify subpopulations, and highlight cell-specific biological characteristics[6–12]. Specifically, single-cell/nuclei RNA-Seq reveals novel cell relationships in the context of hematopoietic stem cells[10,11], lymphoid and adipocyte cells[13], describes the immune cell repertoire in atherosclerosis[14], neural dynamics in newborns[15] and is used as a tool to optimize differentiation protocols[16].Most notably in the cardiac context, scRNA-Seq has proven to be a valuable tool for: 1) identification of cardiac nonmyocyte transcriptional heterogeneity in the uninjured murine heart and the substantial loss of identity markers of in vitro expanded cells compared with their freshly isolated ancestors[17,18], 2) optimization cardiomyocytes reprograming protocols[19]; 3) defining cardiomyocytes chamber-specific transcriptional signatures in developmental stages[6,20]; 4) assessing differentiation capacity of enriched c-kit populations[21], 5) lineage tracing myofibroblast populations[22] and; 6) unveiling culture expansion effects upon transcriptome diversity and heterogeneity critical for adoptive transfer protocols[18].

Collectively, these findings together, establish a remarkable initial framework to study the biological role, diversity, interplay and drift of the identified cardiac subpopulations. Cardiac

biology presents unique challenges in resolving the standing questions in the field. For instance, a truly unbiased analysis of the transcriptional heterogeneity of the cardiac interstitial population remains to be done, as previous approaches may have overlooked modestly represented populations or were based upon protocols that preemptively depleted for specific cell types[17]. Monolayer culture protocols decrease native heterogeneity and impact the overall transcriptome, therefore alternative in vitro expansion protocols need to be developed and tested[18]. Cell size and cardiomyocyte morphology tend to be noncompatible with various single-cell RNA-Seq platforms, particularly droplet base systems. Transcriptional profiling of single nuclei cardiomyocytes has been performed to circumvent size incompatibility[23], yet the impact of ploidy and nucleation states in the transcriptional phenotype remains elusive. Functional baseline heterogeneity of all cardiac populations needs to be described and annotated during the evolution of various types of cardiac injury and in the aging heart to truly understand the cardiac intercellular dynamics. The impact of ploidy states in cardiac homeostasis recently reported[24] defines an emerging aspect of basic cardiac biology requiring further exploration to establish the impact of ploidy upon functional divergence in the mammalian myocardium. Novel technological platforms and creative bioinformatic analysis are proving invaluable to resolve these longstanding issues and gain insights in cardiac regenerative medicine.

1.3 Advancing transcriptional platforms

Cardiomyocyte cell morphology, cryopreservation of limited samples, adequate selection of transcriptional platform and data availability are but a few of the difficulties that add to the complexity of analyzing cardiac populations at a single-cell resolution. Overwhelming as these challenges may appear, the tools to move forward already exist and others continue to be developed (Table 1.1). Recently, single-nuclei RNA-Seq has revealed long intergenic noncoding RNA

regulation of cell cycle stress response in cardiomyocyte[23], differentiated myoblasts[25] and other applications[15,26]. Cryopreservation remains a technical challenge for preparation of limited samples for storage, nevertheless protocols continue to being tested in various cell types and tissues to confirm minimal impact upon transcriptional profiles[23,27]. Robustness of scRNAseq platforms and lineage-specific transcription factor lineage reconstruction has been performed in a massive collaborative effort to make publicly available organism-wide transcriptional representation of murine diversity (Tabula muris)[28]. Slide-Seq, a high spatial resolution tool has been developed to assess transcriptional topology in tissue[29]. BRB-Seq and Div-Seq stand among the recently developed tools used in barcoding and demultiplexing bulk RNA-Seq[13] and Edu labeling of single nuclei to capture cellular dynamics[15]. These platforms in conjunction with non-transcriptional methodologies such as single-cell immunoblotting[12], mass cytometry[14] and ATAC-Seq[1], have the potential to solve long standing questions associated cardiac transcriptome-proteome relationships, post-transcriptional modifications and impact of chromatin states upon the transcriptome and discrete cardiac populations.

1.4 The targeted bioinformatics approach

Technological availability and technical access are not the only challenges to overcome in bioinformatic analyses of the cardiac transcriptome (Figure 1.1). Appropriate methods to generate and curate biological data, as well as subsequent steps of quality control, analysis, interpretation, and representation are integral elements of bioinformatic technology transfer. As with any experimental approach, it begins with an adequate experimental design which keeps in mind the strengths and limitations of the platform selected to generate biological data. Datasets derived for transcriptome analysis are by definition ‘big’ enough to require nonconventional computational approaches, increasing the risk of getting lost in an ocean of information. While exploratory

analysis is always required, targeted analysis and computational approaches should be outlined at early stages of design to mitigate the risk of drifting away from a coherent and focused conclusion.

Just as with platform selection, the analyses available hold advantages and drawbacks. For instance, dimensionality reduction (principal component analysis, t-distributed stochastic neighbor embedding, and uniform manifold approximation and projection[30] are useful in hierarchical, unsupervised and phenotypic clustering of single cells and identity annotation[12,14,23]. Gene expression data can yield information on frequency distribution[14], gene set enrichment[14], intercellular communication analysis[16,17], differential gene expression, gene ontology, pathway enrichment analysis[16], cell surface signature analysis[3], gene correlation and network analysis[23], cellspecific transcription factor enrichment and networks[28], spanning-tree progression analysis of density-normalized events[20], and pseudotime analysis[12,19,26,31,32]. Depending on the platform used for RNA-Seq, beside transcript quantification, isoform detection, genetic, transcriptomic variant calling[33] and organ spatial reconstruction[34] can also be performed.

Analysis selection will largely depend upon hypothesis or biological questions to be resolved, with a serious challenge being the noticeable disconnect between biologist/clinicians who know which critical biological questions to pursue versus bioinformatics specialists who are versed in the advantages and limitations of bioinformatic approaches available. Bridging communication between these two groups is imperative to avoid underutilization of datasets, maximize the yield of information, design cost-effective experiments, and prevent data misinterpretation.

1.5 Conclusion

Outside of the biological context, ‘transcription’ is defined as a process associated with faithful and systematic recording of information in written form; the process of data documentation

with promising potential to draw accurate interpretations. The mammalian heart remains an elusive and challenging target to generate translational approaches in regenerative biology. However, with ever-evolving technology, appropriate bioinformatic approaches, and collective efforts and synergistic communication, the field will overcome current challenges and accurately transcribe what the heart has to say.

1.6 Translational Perspective

Novel technologies are required to circumvent limitations associated with basic cardiac biology. Transcriptional profiling platforms continues to produce phenotypical data essential for advancement of therapeutic approaches. Accurate interpretation of multivariate transcriptional data holds the potential to improve in vitro expansion protocols critical for adoptive transfer approaches, restore transcriptional phenotypes in vivo and ultimately to improve efficiency of cardiac regenerative and therapeutic approaches after injury. Unique challenges in the study of the cardiac transcriptome continue to be addressed such as: cardiomyocyte morphology, cryopreservation of limited samples and adequate selection of transcriptional platform at a single-cell resolution. Still much remains to be done, with development and implementation of novel transcriptional platforms and creative bioinformatic analysis as essential elements to resolve standing questions in the field of cardiac regenerative medicine.

1.7 Acknowledgements

This work was supported by NIH grants R01HL135661-02. Chapter 1, with slight modifications, is a reprint of the material as it appears in Regenerative Medicine, Vol. 14, No. 9. Transcribing the heart: Faithfully interpreting cardiac transcriptional insights. Echeagaray Oscar

and Sussman Mark Alan. The dissertation author was the primary author and investigator on this manuscript.

Table 1.1 Chronology of cardiac research and technological progress in transcriptional analysis.

Expansion of literature associated with cardiac transcriptome and technical advances in transcriptome analysis and platforms by year.

Year	Area	Citation	Brief description
2014	Cardiac Transcriptome	[5]	Characterization of the cardiac fibroblast transcriptome
2015		[20]	Lineage tracing of cardiac progenitor cells and cells derived from mouse embryonic stem cells
2016		[6]	Transcriptional analysis of cardiac cells isolated throughout cardiac development
2016		[22]	Lineage tracing and transcriptional analysis of myofibroblasts
2016		[24]	Single nuclei RNASEQ on human myoblasts
2017		[21]	Single cell transcriptional analysis of cKit+ cells
2017		[19]	Fibroblast to cardiomyocyte reprograming efficiency assessed by transcriptional analysis
2017		[1]	Multicellular analysis of sorted populations by bulk RNASEQ
2017		[23]	Single nuclei transcriptional analysis of cardiomyocytes
2018		[16]	Endothelial differentiation efficiency from induced pluripotent stem cells assessed by scRNASEQ
2018		[27]	Compendium on single-cell transcriptional data of various mouse tissues
2018		[17]	Transcription analysis of cardiac nonmyocyte populations
2018		[29]	Immune characterization of healthy and atherosclerotic cells using scRNASEQ
2018		[2]	Implications of topological states in cardiac fibroblasts
2018		[18]	Impact of culture adaptation on the in situ transcriptome of cardiac interstitial cells
2019		[3]	Cardiac progenitor cells transcriptional signatures evaluated by bulk RNASEQ
2016	Technical Advancement	[15]	Protocol design to assess the transcriptome of recently dividing cells
2017		[26]	Impact of cryopreservation on sample transcriptional profile
2019		[13]	Protocol design for cost-efficient bulk RNASEQ
2019		[14]	Dimensionality reduction of single-cell data using uniform manifold approximation and projection (UMAP)
2019		[28]	Development of platform to identify spatial transcripts in tissue

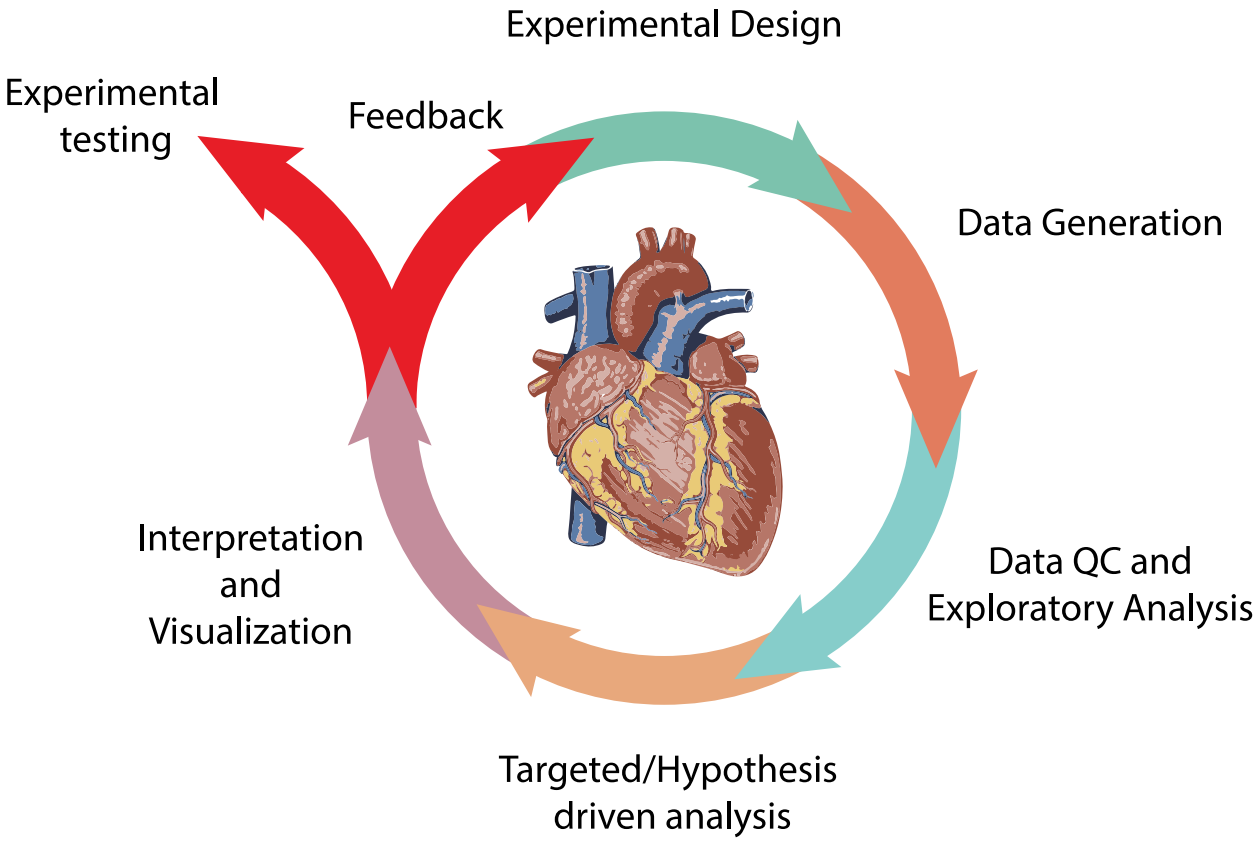

Figure 1.1 The bioinformatic process in the analysis of the cardiac transcriptome.

CHAPTER 2
Transcriptional features of biological age maintained in human cultured cardiac interstitial cells

2.1 Abstract**:**

Ex vivo expansion of cells is necessary in regenerative medicine to generate large populations for therapeutic use. Adaptation to culture conditions prompt an increase in transcriptome diversity and decreased population heterogeneity in cKit+ cardiac interstitial cells (cCICs). The "transcriptional memory" influenced by cellular origin remained unexplored and is likely to differ between neonatal versus senescent input cells undergoing culture expansion. Transcriptional profiles derived from single cell RNASEQ platforms characterized human cCIC derived from neonatal and adult source tissue. Bioinformatic analysis revealed contrasting imprint of age influencing targets of 1) cell cycle, 2) senescence associated secretory phenotype (SASP), 3) RNA transport, and 4) ECM-receptor/fibrosis. A small subset of cCICs exist in a transcriptional continuum between "youthful" phenotype and the damaged microenvironment of LVAD tissue in which they were embedded. The connate transcriptional phenotypes offer fundamental biological insight and highlights cellular input as a consideration in culture expansion and adoptive transfer protocols.

2.2 Keywords:

In vitro expansion, Senescence, Biological age, Single cell RNASEQ, Culture adaptation, Transcriptional memory

2.3 Introduction:

Single cell transcriptional analysis is a powerful tool to derive biological insights by inferring cellular phenotypic characteristics. Single cell methodologies are now routinely employed to interrogate cell populations for biological properties, complex cellular interactions, and evaluate potential of next-generation *ex vivo* cell-based therapeutics[35–37]. Our group found that standard culture conditions prompt concurrent acquisition of transcriptome diversity, merging commonality, and loss of original cell identity markers in murine cKit+ cardiac interstitial cells (cCICs)[38]. However, migration toward transcriptome homogeneity in cCIC cultures may be limited by replicative senescence evidenced by "transcriptional memory". Simply put, adaptation to culture conditions is likely subject to the biological age of the input cell population[24,39]. Cardiac cell therapies require *in vitro* expansion, with adoptive transfer protocols relying on culture expansion as an essential step to ensure adequate cell supply and potential *ex vivo* enhancement[40–43]. Culture expansion influences upon donor cells have been previously reported but characterization and understanding of these effects remains limited[44,45].

The influence of biological age upon adaptation to *in vitro* culture can be examined by comparing cCIC derived from chronologically young versus aged myocardial tissue samples. Human subject tissues provide the "gold standard" for translational relevance, with neonatal cCIC exhibiting a youthful phenotype relative to cells derived from aged and failing hearts[39]. Human cCICs derived from ventricular tissue of neonate or adults undergoing left ventricular assisted device (LVAD) implantation were used as input for *in vitro* expansion and subsequent single cell transcriptional profiling. Transcriptional reprogramming prompted by culture of human cCICs would ordinarily lead toward increased commonality[38], but adaptability may be limited by the tissue of origin reflected in neonatal versus damaged/senescent myocardium microenvironments.

Therefore, the guiding hypothesis was that age and/or condition of origin is represented by "transcriptional memory" profiling as well as population heterogeneity characteristics of cCICs undergoing in vitro expansion. Although cell identity markers are indeed diminished by in vitro expansion, transcriptome profiling reveals segregation of neonatal versus LVAD-derived cCICs through bioinformatic analyses. Transcriptional features intrinsic to the origin microenvironment of donor cells remains despite the artificial culture environment, either neonatal or senescent/pathologic. Retention of transcriptional phenotypic signature of origin furthers understanding into moderate efficacy of select cell-based therapeutic strategies and provides and highlights the importance of cellular adaptation for strategic design of adoptive transfer protocols and treatments involving donated cells.

2.4 Materials and Methods:

2.4.1 Neonatal and Adult cCIC Isolation

Neonatal cKit$^+$ cardiac interstitial cells (cCIC) were derived from nonsurgically obtained postmortem cardiac tissue. Adult human cCICs cell lines for individual isolates from two patients undergoing surgical implantation of a left ventricular assist device (LVAD).

Table 2.1 Sample passages and medical history

SAMPLE	SEX	AGE	PASSAGE	MEDICAL HISTORY
H16-114	Female	60	5	Hypothyroidism Acute and Chronic systolic and fiastolic heart failure
H13-65	Male	54	5	Pathological sample from patient not available
NEONATAL	Male		5	N/A

The study was designed in accordance with The Code of Ethics of the World Medical Association (Declaration of Helsinki) and approved by the institutional review committees at San Diego State University along with the institutional review board (#120686). Neonatal heart tissue procured from post-mortem infants (spontaneously deliver that did not survive), with informed consent from family members, was provided by a commercial source (Novogenix Laboratories) and used for isolation of human cardiac cells. LVAD derived samples were received from consenting patients with institutional review board (IRB) approval following NIH guidelines for human subjects' research. All patients were fully consented to donate explanted tissue sessions prior to surgery. Cells were isolated as previously published, and expanded to replicate standard conditions[38,46,47].

Briefly, heart samples were mechanically minced into 1-mm3 pieces and digested in collagenase II (150 U mg/mL, Worthington, LS004174) followed by brief low-speed (850 rpm for 2 minutes) centrifugation to remove cardiomyocytes and tissue debris. The supernatant was subjected to magnetic-activated cell sorting using c-kit–conjugated microbeads (Miltenyi Biotec,

#130-091-332), and c-kit– enriched cells were plated in human c-kit CIC media. Neonatal and LVAD derived cCICs were incubated at 37°C in 5% CO2 to passage 5 and used for single cell RNASEQ (scRNASEQ). Media used in the study are listed in Table S1. Media used in the study contained: 10% ES FBS (16141061, Gibco), 1% Penicillin-Streptomycin-Glutamine (100X, 10378016, Gibco), 5 mU/mL human erythropoietin (H5166, Sigma), 10 ng/mL human recombinant basic FGF (GMP100-18B, Peprotech), 0.2 mMol/L L-Glutathione (10007461, Cayman) in F12 HAM's (1x) (SH30026.01, HyClone).

Table 2.2 Human cKit+ Cardiac Interstitial Cells Medium

	COMPONENT	CATALOG NUMBER
HUMAN CKIT+ CARDIAC INTERSTITIAL CELLS MEDIUM	10% ES FBS	16141061, Gibco
	1% Penicillin-Streptomycin-Glutamine (100X)	10378016, Gibco
	5 mU/mL human erythropoietin	H5166, Sigma
	10 ng/mL human recombinant basic FGF	GMP100-18B, Peprotech
	0.2 mMol/L L-Glutathione	10007461, Cayman
	F12 HAM's (1x)	SH30026.01, HyClone

2.4.2 Library generation and Sequencing

Single-cell RNA-Seq libraries were generated by loading Neonatal and LVAD derived cells suspension on a Chromium™ Controller (10x Genomics) and prepared using Chromium ™ Single Cell 3′ Library & Gel Bead Kit v2 (10x Genomics) following manufacturer's protocol. Library fragment size was determined with Agilent Bioanalyzer High Sensitivity DNA Kit (average library size: 450–490 bp). The sequencing libraries were quantified by quantitative PCR (KAPA Biosystems Library Quantification Kit for Illumina platforms P/N KK4824) and Qubit 3.0

with dsDNA HS Assay Kit (Thermo Fisher Scientific). Libraries were sequenced at the UC San Diego IGM Genomics Center utilizing an Illumina HiSeq2500 with 2 × 75 paired-end kits using the following read length: 98 bp Read1, 8 bp i7 Index, and 26 bp Read2. Single cells libraries were processed concurrently and pooled together after sample indexing and prior sequencing to prevent batch effect.

Raw sequencing data was processed and aligned with the Cell Ranger pipeline (10X Genomics, Version 3.0.1). Sequencing reads were aligned to the human genome GRCh38-3.0.0. Libraries were aggregated and sequencing depth normalized using CellRanger Version 3.0.1.

2.4.3 Single cell selection and quality control

Cells with fewer than 200 genes were filtered out to avoid inclusion of empty droplets in downstream analysis. Based on UMI and gene detection distribution droplets multiplets were excluded using the Interquartile Range Rule (Values over the third quartile and 1.5 the interquartile range are consider outliers). Cell with more than 10% of mitochondrial gene UMI count and genes detected in fewer than three cells were filtered out using Seurat R Package (v3.2.0)[48]. The first 12 principal components were found to be significant to perform dimensionality reduction. Preparations derived from in vitro studies yielded 4722 barcoded cells for analysis, from which 2943, and 1779 corresponded to LVAD and Neonatal derived, respectively. Final removal of unwanted sources of variation and batch effect correction strategies included normalization of sequencing depth of samples on CellRanger Version 3.0.1 and on Seurat (v3.2.0) LogNormalization of the data that normalizes the feature expression measurements for each cell by the total expression, followed by identification and scaling of single cell variable features using the “Variance Stabilizing Transformation” (vst) selection method.[48,49].

2.4.4 Dimensionality Reduction and Unsupervised Clustering

Approximately 2000 variable genes were selected based on their expression and dispersion. Prior dimensionality reduction, data was scaled to mean expression equal to 0 and variance across cells equal to 1. Principal component analysis was performed on the scaled data as a linear dimensionality reduction approach. The first 12 most significant principal components (PCs) were selected for non-linear dimensional reduction and unsupervised clustering using a complementary methods including supervised PC selection, Jackstraw statistical and heuristic approaches[50].

2.4.5 Differential expression analysis

Differential expression analysis was done using Wilcoxon rank sum test and selecting for a threshold of 0.05 for an adjusted p-value and a log (FC) >0.25 was used to define statistically significant and differentially expressed genes (DEGs).

2.4.6 Gene ontology analysis

Gene ontology(GO) enrichment analysis for DEGs lists derived from Neonatal, LVAD and Intermediate cells was performed using the enrichGO and compareCluster functions of clusterProfiler (3.16.1) R package[51]. GO term enrichment was calculated with a minimum annotation size of 10 and a maximum of 500 genes, selecting for GO terms with p-value cutoff of 0.05 using BH method.

2.4.7 RNA velocity and pseudotime analysis

RNA velocity was performed to explore the transitional states of Neonatal and LVAD derived cCICs. Expression data from 4722 cells was used to generate a cds object to process through monocle3[52–54]. Analysis were performed using 12 PCs for dimensionality reduction and trajectory inference.

2.4.8 Gene expression module scores

Modules scores for single cells were calculated for Secretory Associated Senescence Phenotype factors (SASPs), Growth Factors, Interleukins, Receptors and Ligands and genes involved in the regulation of Wnt pathway, using the AddModuleScore function in the Seurat R package. Cell Cycle score and analysis was performed as described by the Satija group[55] based on the cell cycle markers developed for scRNA-SEQ analysis[56].

Table 2.3 Gene targets per module score.

	SASPs	Growth Factors	Interleukins	Receptors and ligands	Wnt Regulation Score
Marker	IL6	AREG	IL6	ICAM1	PSMA4
	IL1B	EREG	IL7	ICAM3	PSMB3
	MIF	NRG1	IL1A	TNFRSF11B	PSMA1
	NRG1	EGF	IL1B	TNFRSF1A	PSMA3
	FGF2	FGF2	IL13	TNFRSF10C	PSMD8
	HGF	HGF	IL15	FAS	PSMD2
	FGF7	FGF7		PLAUR	PSMB1
	VEGFA	VEGFA		IL6ST	PSMC1
	ANG	ANG		EGFR	PSMD13
	CXCL12	KITLG			PSMB6
	IGFBP3	CXCL12			PSMC3
	IGFBP4	PIGF			PSMB2
	IGFBP6	NGF			PSMB7
	IGFBP7	IGFBP2			PSMA7
	MMP1	IGFBP3			PSME2
	TIMP2	IGFBP4			PSMB5
	SERPINE1	IGFBP6			RBX1
	PLAT	IGFBP7			PSMA5
	CTSB				CTNNB1
	ICAM1				RUVBL1
	ICAM3				HDAC1
	TNFRSF11B				CAV1
	TNFRSF1A				PSMD3
	FAS				SNX3
	IL6ST				CDC42
	EGFR				RHOA
					CALM1
					PFN1
					AP2M1

2.4.9 KEGG pathway analysis

DEG lists in ENTREZ ID format from Neonatal and LVAD samples were used as input for pathway analysis. DEGs fold changes were used to identify pathways upregulated in Neonatal or LVAD samples. The pathview R package (V1.28.1) was used to integrate transcriptional data and visualize relevant pathway paths.

2.4.10 Data availability

scRNA-Seq data generated in this study has been uploaded to the NCBI Gene Expression Omnibus (GEO) database under the Accession No. **GSE164026**.

2.5 Results:

2.5.1 Connate transcriptional profiles segregate Neonatal and LVAD derived cells after culture expansion.

cCICs were derived as previously described[46] from human neonatal cardiac samples or adult heart failure patients undergoing surgical LVAD implantation (See Methods). Single cell suspensions of neonatal or LVAD cCICs were processed in a droplet single cell RNA-SEQ platform (10x Genomics) (Fig. 2.1a). Unsupervised clustering revealed 11 clusters (Clusters 0-10) in the aggregated samples (Fig 2.1b). Transcriptional segregation of neonatal and LVAD cCICs was evident through dimensionality reduction approaches (Fib. 2.1c). The transcriptional divide was more pronounced in Neonatal/LVAD ratios between each cluster after normalization to input, with 3 clusters being composed of primarily neonatal cCICs (Clusters 1, 2 and 6), 6 clusters LVAD (Clusters 0, 3-5, 7 and 10) and only 2 clusters being comprised of both neonatal and LVAD cells (Cluster 8 and 9)(Fig. 2.1d). Cluster 0 displayed the highest cell frequency with 875 cells, with clusters 0-7 making up ~90% of the analyzed cells (Fig. 2.1e). Consistent with our previous observations[38] and expression data from the cellular milieu in the adult human heart[57], both neonatal and LVAD cells showed loss of expression for cell identity markers characteristic of freshly isolated cCICs (Data not shown). However, differential expression analysis revealed 577 differentially expressed genes (DEGs) characteristic of each group (Fig. 2.1f). Collectively,

neonatal and LVAD derived cCICs lost cell identity markers upon ex vivo expansion yet retain a distinct transcriptional signature connate to their origin.

2.5.2 Neonatal cells transcriptome associated with higher cell cycle progression and proliferation

Cultured cells expressed cell cycle and proliferation genes at a higher proportion than freshly isolated parental cells[38,39]. Assessment of biological age transcriptional imprint in cultured populations was performed through cell cycle scoring using previously developed using markers for scRNA-SEQ analysis[56] (Fig. 2.2a). Analysis revealed 35.5% and 39.6% of neonatal cells to be in G2M and S phases of the cell cycle respectively, while 63.5% of LVAD cells were scored in G1 phase (Fig. 2.2b). Neonatal cCICs displayed approximately two-fold increase in cells in G2M and S phases compared to LVAD cells. The opposite was observed in LVAD cells in G1 showing a 2.5-fold change increase in comparison to neonatal cells. Neonatal cCICs expressed higher levels of G2M genes[56] (Fig. 2.2c) and at a higher rates, as illustrated by expression of MKI67 and CCND1, markers consistently associated with cell proliferation. MKI67 was expressed in 35.9% of neonatal cCICs with only to 12.6% LVAD derived cells expressing it. The increase was consistent with the ~2.5-fold increase in Cyclin D1 previously reported in cells comparably prepared[39,58] (Fig. 2.2d and 2.2e). These results demonstrate that a cell cycle imprint associated with biological age persists after culture and is sufficient to surmount influences of culture adaptation.

2.5.3 Senescence Associated Secretory Phenotype factors overexpressed in LVAD derived cells

Cellular senescence is not limited to replicative arrest, as detrimental effects have been documented in vitro and *in vivo* upon intracellular regulation and the microenvironment surrounding senescent cells[59]. Expression of Senescence Associated Secretory Phenotype factors

(SASPs)[59] was surveyed in culture expanded cCICs to assess widespread changes consequential to biological age and pathology. Overexpression was characteristic in LVAD-derived cells for interleukins (IL6, IL1B), inflammatory factors (MIF) and growth factors and regulators (NRG1, FGF2, HGF, FGF7, VEGFA, ANG, CXCL12, IGFBP3, IGFBP4, IGFBP6 and IGFBP7), proteases (MMP1, TIMP2, PLAT and CTSB) and soluble receptors/ligands (ICAM1, ICAM3, TNFRSF11B, TNFRSF1A, FAS, IL6ST and EGFR) (Fig. 2.3a). Interestingly, SERPINE1 has been associated with coronary heart disease but was overexpressed in neonatal cells. Additional SASPs markers were evaluated showing mild to consistent upregulation on LVAD derived cells, with the exception of TGFB1 (Data not shown)[60]. Pseudotime analysis using Monocle3 established the progression of cultured cells from distinct origins in clusters 8 and 9 (Fig. 2.1d and 2.3b). Using expression of SASPs and ODC1 as a target critical for development[61], the transcriptional trajectory between neonatal and LVAD derived cells was defined, pseudotime abstract units were calculated, and directionality of the system was authenticated (Fig. 2.3b, 2.3c). LVAD derived cells positioned in the terminal leaves of the pseudotime plot consistent with the transcriptional profile of their aged origin. Further confirmation using expression of 39 genes generated SASP (26 genes), growth factor (18 genes), interleukin (6 genes), and receptor and ligands (9 genes) scores for each cell in our dataset (See Methods). Neonatal cells scored lower for growth factors, receptors and ligands and overall SASPs targets, while maintaining a similar score of interleukin expression (Fig. 2.3d). Beta galactosidase 1 (GLB1) was expressed in 0.28% of neonatal cCICs with to 0.5% LVAD derived cells expressing it. The increase observed in LVAD samples was consistent with the increase observed in senescence markers p16 and GLB1 previously reported by our group in cells comparably prepared[62]. Overexpression of Fibroblast Growth Factor 2 (FGF2) and Hepatocyte Growth Factor (HGF) along with other secretory targets in LVAD cCICs is consistent with

previous observations[46] (Fig. 2.3e). Collectively, these results support transcriptional imprinting in LVAD derived cells resulting from prolonged cellular stress *in vivo* prompts acquisition of a widespread senescent profile that is absent in neonatal cCICs.

2.5.4 LVAD cCICs deregulate elements of RNA transport pathway

Pathways associated with the transcriptional imprint of biological age delineate mechanisms in which biological age promotes and/or correlates with SASP and impairment of cell cycle. Significantly identified DEGs and fold-changes obtained through differential expression analysis (Fig. 2.1f), were cross-referenced with the Kyoto Encyclopedia of Genes and Genomes (KEGG). KEGG pathway analysis and single cell expression confirmed LVAD-derived cCICs downregulate key elements of RNA transport pathways compared to neonatal samples (Fig. 2.4a). Targets upregulated in neonatal cells included nuclear pore complex components TPR and UBC9 (encoded by the UBE21 gene), the transcription initiation factors 4E-BP, eIF1 and eIF4G (encoded by the EIF4EBP1, EIF1 and EIF4G1 genes respectively), units of the exon-junction complex Upf3 and SRm160 (encoded by the UPF3A and SRRM1 genes respectively) and the superoxide dismutase IPOB (encoded by SOD-2). Interestingly, only eEF1A (encoded by the EEF1A1 gene) which plays a role in translation, recruitment of t-RNA and nuclear export was upregulated in LVAD samples.

Consistent with their origin and biology, neonatal and LVAD cCICs did not show expression of Fcγ receptors typical of hematopoietic lineages. However, KEGG pathway analysis revealed expression of targets downstream the Fcγ receptors and involved in FcγR mediated phagocytosis in neonatal cells (Fig. 2.4b). Neonatal targets included secondary signaling molecule SPHK cell, cell cycle regulator CDC42 and the filipodia associated MyosinX (encoded by SPHK1,

CDC42 and MYO10 genes respectively). Podosome forming protein Gelsolin was upregulated in LVAD samples.

Fewer DEGs matched with the mitogen-activated protein kinases (MAPK) pathway. In contrast to the repression observed in other pathways, LVAD cells displayed upregulation of receptor tyrosine kinases and growth factors (Fig. 2.3e and 2.4c). Consistent with SASPs findings there was an increase in the expression of Interleukin 1B and its receptor, which role in heart disease has been documented [63]. Collectively, these results indicate that cell cycle and SASPs transcriptional features retained after culture adaptation correlate with deregulated RNA processing, transport capacity and enhanced growth factor sensitivity in LVAD cells.

2.5.5 LVADs cCICs show a pre-fibrotic and ECM upregulated phenotype

Collagen expression, deposition, and cross-linking is associated with the progression of heart failure [64], myocardial stiffness[65] and increase in adventitial fibrosis in LVAD patients [66]. KEGG analysis revealed ECM-Receptor interaction as an additional pathway predominantly upregulated in LVAD cells (Fig. 2.5a). Except for Collagen IV, multiple extracellular matrix and cell adhesion proteins were upregulated in LVAD derived cCICs including collagens, THBS2, Laminin and Fibronectin as revealed by single cell expression (Fig. 2.5b). Periostin and TCF21, both markers of activated cardiac fibroblasts[67,68], showed higher expression level in LVAD derived cells and were positioned in the terminal leaves of pseudotime plot compared to neonatal cCICs (Fig. 2.5c and 2.5d). Co-expression analysis verified robustness of observations not driven by spurious expression of single fibroblast or ECM markers. Fibrotic shift in LVAD cells is consistent with co-expression of fibroblast and ECM markers (Fig. 2.5e). Collectively, these results demonstrate LVAD derived cCICs are primed with a fibrotic phenotype.

2.5.6 Intermediate subsets overexpress Wnt regulators and maintain a hybrid phenotype

A subset of neonatal and LVAD cCICs representing approximately 9% of analyzed cells which we refer to as "Intermediate cells" (aggregate of clusters 8 and 9) with the rest of the clusters being exclusively Neonatal or LVAD. Intermediate cells converged to a common transcriptome (Fig. 2.6a), with differential expression analysis as well as gene ontology analysis revealing additional insights. Differential expression analysis revealed 733 DEGs upregulated in the Intermediate group (517 and 534 DEGs for LVAD and neonatal respectively; Fig. 2.6b), which were used as input for GO term analysis. Annotation by cellular components reveals enrichment for focal adhesion and cell-substrate junction components in LVAD cells, whereas elevated metabolic activity as well as enrichment for ATP synthase complex and mitochondrial respiratory chain elements in neonatal and Intermediate cells (Data not shown). DEGs annotation for molecular function revealed prominent oxidase, ATP synthase and transmembrane activity GO terms in Intermediate cells, while oxidoreductase activity and various ECM binding GO terms typified the Neonatal and LVAD derived cells respectively (Data not shown). Congruent with results from KEGG pathway analysis, annotation by biological process reveal LVAD cells were enriched with ECM organization and interleukin GO terms, while neonatal cells show GO terms associated with initiation and regulation of RNA translation (Data not shown). Regulators of Wnt signaling were prominently featured in GO terms of intermediate cells (Fig. 2.6c) as confirmed by expression of 29 genes. Wnt regulation-associated transcript expression and calculated score was highest for intermediate cells while neonatal and LVAD expression score distributions were both lower (Fig. 2.6d and 2.6e). Wnt signaling is activated upon myocardial infarction consistent with participation during inflammation and fibrosis [69]. Further examination of the intermediate population revealed five subclusters with a consistent relative even split in cell distribution between Neonatal and LVAD populations (Data not shown). The hybrid transcriptional profile of

intermediate cells overlapping with both neonatal and LVAD populations reveals a mixture of SASPs, cell cycle, fibrosis and RNA transport markers. (Fig. 2.6f-h). These results together indicate the intermediate subset exhibits a hybrid phenotype drift characterized by Wnt pathway regulation and reprogramming that transcriptionally segregates these cells from the parental isolates.

2.6 Discussion:

Consequences of disease as well as age exert profound influences upon cells including alteration of gene expression, metabolism, functional competency, replicative potential, and more [70,71]. Certain features of aged cells are exacerbated or mitigated by environmental conditions in host tissues such as oxidative stress, nutrient status, inflammatory / cytokine production, and pathological changes [59,72–74]. Many of these conditions can be recapitulated in cell culture studies with treatments that mimic the aged tissue environment [75,76]. Studies using established cell lines to study biological consequences of aging are of limited value for extrapolation to the complex in vivo mileau. *In situ* studies have provided significant insight regarding adaptations and distinct features of aged cells [77–79], but whether the characteristic phenotypic state of aged cells is retained following isolation and culture expansion is poorly understood. Moreover, conditions of culture expansion inherently favor cells with the highest proliferative and survival potential. Thus, it is unclear to what extent culture expansion allows hallmarks of aging to persist when harvesting cellular samples from aged tissue and subjecting them to multiple passages after initial isolation.

Biological characterizations of cultured cells are often used as a proxy for their in vivo counterparts to correlate phenotypic properties and identify cellular responses [75]. However, even in the case of primary cultured derived directly from tissue explants there is evidence of rapid adaptation to culture conditions, selective pressure, and loss of differentiated characteristics [80]. Such changes are particularly evident at the transcriptional level, where our group previously documented increased gene expression diversity together with loss of identifying cell markers in primary isolations of cCICs subjected to *in vitro* expansion [38]. Thus, many distinct hallmarks of primary cells vanish in the wake of Darwinian selection occurring *in vitro* with serial passaging. However, our previous study [38] compared freshly isolated cells versus derivative cultured

counterparts from young healthy mice. Whether cells derived from an aged environment coupled to chronic pathological stress would be capable of similar transcriptional reprogramming leading to a 'rejuvenated' profile exhibiting reduction of senescence and/or functional impairment markers remains to be explored. The decision to use human heart primary explants was based upon the impaired biological phenotype of aged cCIC from previous studies [39] supporting the premise that cells isolated from heart failure patients were most likely to show persistent irreversible transcriptional signatures when compared to identically prepared neonatal cells. The yield of cells obtained (4722 total cells, 1779 neonatal and 2943 LVAD) is sufficient for bioinformatic analyses.

Neonatal cells exhibit enhanced growth kinetics and telomere length compared to LVAD derived cCICs[39] consistent with our findings of autochthonous transcriptional features in cultured cCICs segregating with biological age (Fig. 2.1). Neonatal cCICs displayed higher frequency and expression levels of G2M genes, including cell proliferation markers like MKI67 and CCND1, and cell cycle regulators CDC8A and CDC20 (Fig. 2.2c). LVAD derived cCICs retained a widespread senescent profile, in particular high expression of proinflammatory interleukins such as IL6 and IL1B, and other SASPs elements like TNF receptors and insulin like growth factor binding proteins (Fig. 2.3a). Pathway and co-expression analysis of fibroblast markers Ddr2, Tcf21, Vimentin, Periostin and Collagen deposition markers indicated a primed fibrotic phenotype in senescent cells (Fig. 2.5). Cell cycle scoring, expression together with SASPs pseudotime analysis (Fig. 2.3) established the transcriptional trajectory from youthful to LVAD-derived senescent cells.

Cellular senescence is associated with deregulation of RNA processing, shuttling, splicing and translation [81,82]. Deterioration of the cellular microenvironment from aging or chronic stress is associated with defective RNA processing in human peripheral blood leukocytes [83]. Consistent

with the literature, KEGG pathway analysis results revealed downregulation of RNA transport pathway in LVAD derived samples such as nuclear basket protein TPR and exon junction UPF3A, with only EEF1A1 (a RNA transcription regulator) gene upregulated in LVAD samples (Fig. 2.4). In contrast, neonatal cCICs exhibit a proliferative profile with upregulation of RNA transport pathway members. These findings demonstrate a persistent impairment of essential RNA transcriptional processing capabilities in LVAD-derived cCIC that is refractory to culture adaptation (Fig. 2.7).

The intermediate cell population represents an aggregate group with intriguing hybrid transcriptional signature features. To our knowledge, the intermediate transcriptional profile of a pre-fibrotic senescent cultured cell subset exhibiting both decreased ECM transcripts and high Wnt pathway regulation has not been previously reported (Fig. 2.5 and 2.6). However, a novel cardiac fibroblast population with strong Wnt-signaling was previously identified by transcriptional profiling [84,85]. These intermediate cells may represent a fraction of neonatal cells starting to senesce in vitro converging with LVAD derived cCICs reactivated in culture. Alternatively, the intermediate population could be arising simultaneously out of both neonatal as well as LVAD groups due to selective pressure of the culture environment.

This study highlights an often overlooked consideration, namely retention of "transcriptional memory" of cells undergoing culture expansion. Influences of age-associated imprinting upon transcriptome plasticity continues to be explored [86] and intersection with culture adaptation remains poorly understood. Clearly, biological aging impacts upon the transcriptome signature of cCIC as shown in this report, consistent with diminished replicative capacity of human cCICs in vitro [24]. Previous evaluation of various cCICs isolation and expansion protocols revealed a high degree of transcriptome similarity with individual donor profiles accounting for major

differences [87].Persistent senescence characteristics are an important limitation for autologous use of aged donor cells in therapeutic treatments. Cell-based interventional strategies need to consider the autochthonous state of the parental origin cells and the impact upon efficacy for engraftment and functional improvement in the clinical setting. Incorporation of ex vivo protocols has been successful to augment the functional potential of aged cells [88]. For example, hypoxic conditions mimicking physiological oxygen tension increased self-renewal, replicative capacity and mitochondrial function of cultured cCIC [89]. Genetic modification with Pim-1 kinase has been shown to 'rejuvenate' human cCIC and enhance reparative potential in adoptive transfer studies [62,90]. Cardiac organoids, cardiac-tissue-like-constructs and CardioClusters all are approaches to facilitate cell-to-cell communications in three-dimensional tissue microenvironments [91–93]. Future strategies for cellular therapeutics should strive to retain youthful phenotypes and/or reprogram senescent adult cells to overcome imprinting from their origin that otherwise compromises desirable functional capabilities.

Findings presented in this report are unavoidably constrained by human sample availability, biology, and costs of analyses. Human genetic diversity is an inherent variable unique to each patient that cannot be controlled but can only be assessed with large individual sample numbers. Along similar lines, samples of aged heart tissue will inevitably exhibit a spectrum of concurrent pathological features ranging from mild to severe. In our experimental design the use of aged tissue from LVAD patients was intended to represent a heart pushed to the limit of biological exhaustion indicative of advanced age and stress for maximum impact upon the derived cCICs. At the other end of the aging spectrum, availability of fresh human cardiac tissue at early developmental stages is always challenging due to ethical and legal concerns. Last, but not least, is the expense and expertise costs associated with scRNA-Seq experimentation and bioinformatic

analyses. Integration of our findings with published non-failing non-human heart scRNASEQ datasets[57] was attempted to increase our sample population. However, comparative assessments with pre-existing datasets provided negligible insights due to multiple factors including differences in isolation protocol, culture conditions, single cell preparation, and interspecies biological compatibility with our samples. Findings presented herein represent an important initial foray into exploring relative forces of cellular origin versus culture adaptation, with a clear need for incorporation of appropriate datasets using cultured cCICs derived from multiple sources including healthy adult hearts to extend the biological continuum in future studies.

2.7 Acknowledgements

This work was supported by NIH grants R01HL135661-02. Chapter 2, with slight modifications, is a reprint of the material as it appears in Genomics, Vol. 113, Issue 6, 2021. Transcriptional features of biological age maintained in human cultured cardiac interstitial cells. Oscar Echeagaray, Taeyong Kim, Alex Casillas, Megan Monsanto, and Mark Sussman. The dissertation author was the primary author and investigator on this manuscript.

2.8 Figures

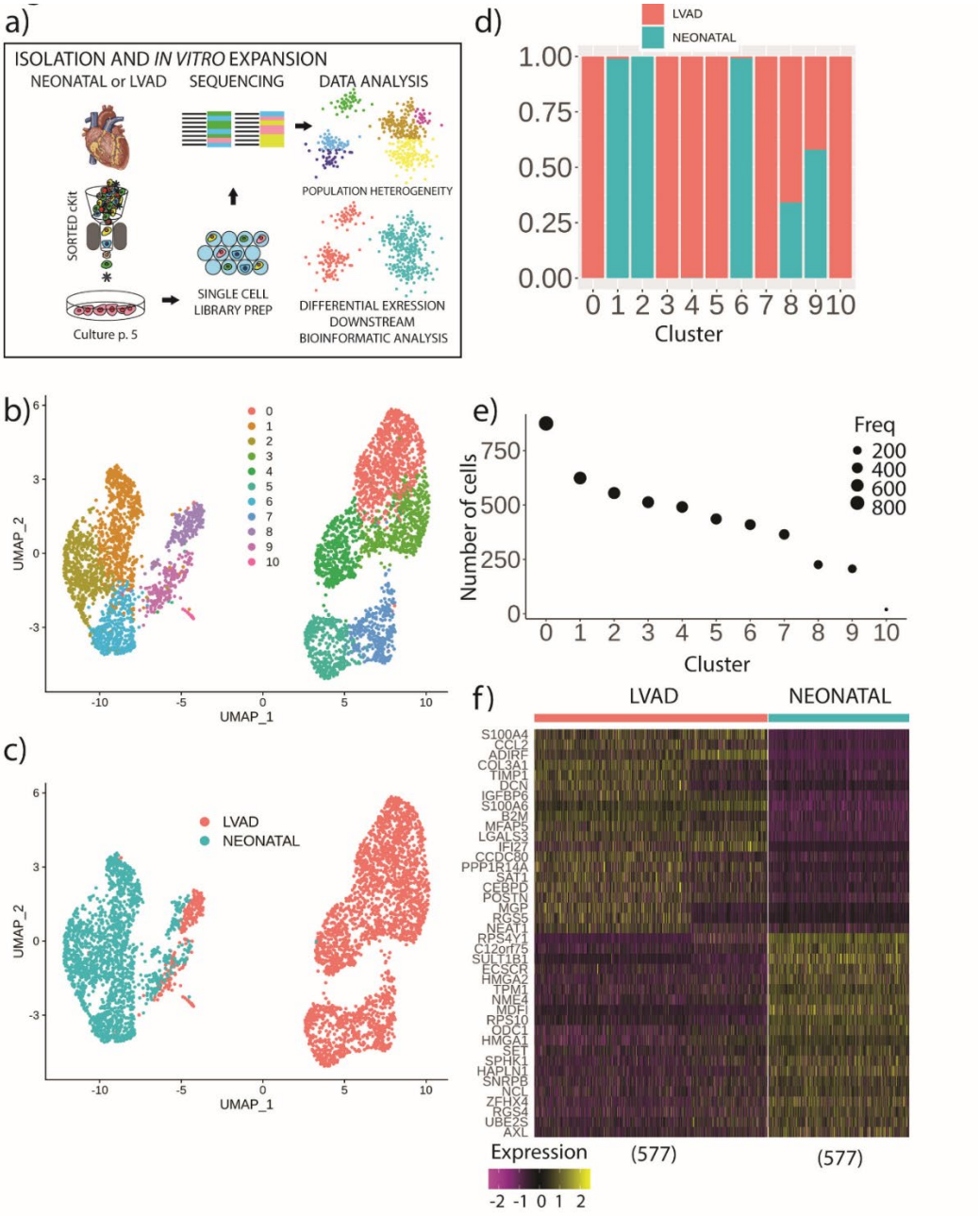

Figure 2.1 Connate transcriptional profiles retained in Neonatal and LVAD derived cells after in vitro expansion.

a) Schematic of experimental workflow of cCICs isolation and scRNASEQ from Neonatal and LVAD cardiac tissue. UMAP projection of cCICs color-coded according to b) unsupervised clustering of gene signatures and c) as derived from either Neonatal or LVAD cardiac tissue. d) Relative and absolute e) contributions of Neonatal or LVAD derived cCICs to each cluster as shown in UMAP (panel b). f) Heatmap representing the top 20 differential expressed genes from Neonatal and LVAD cCICs.

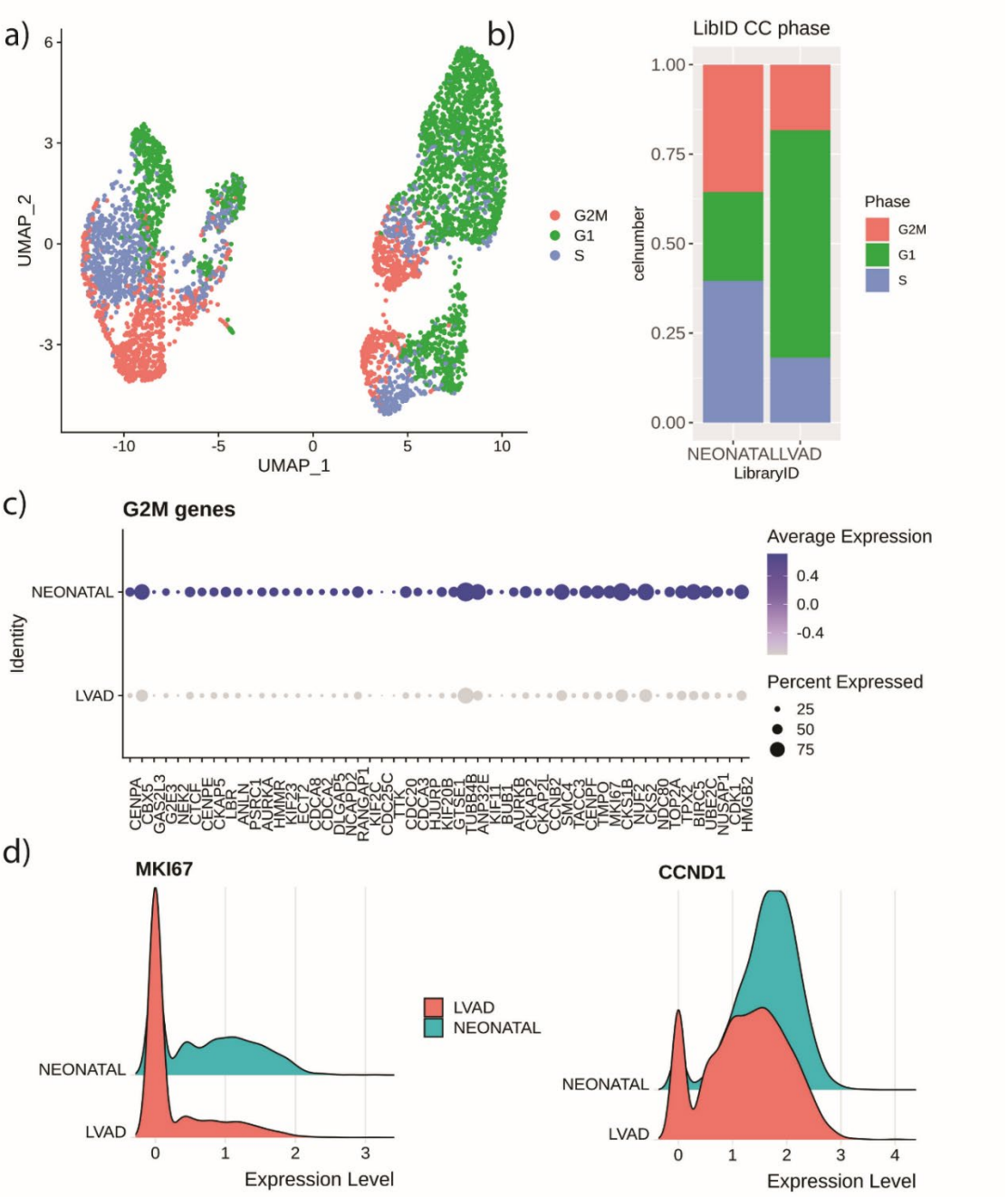

Figure 2.2 Cell cycle expression patterns heightened in neonatal derived cells.

a) UMAP projection of cells color-coded by transcriptional cell cycle score. b) Stacked bar graph representing ratio of cells in G2M, G1 and S stages according to cell cycle score. c) Dotplot representing expression of G2M-specific genes in both populations. Circle diameter represents the percentage of cells expressing a particular gene, while normalized average expression is represented by color intensity. d) Ridge plot representing MKI67 transcript expression and cell distribution on neonatal and LVAD populations.

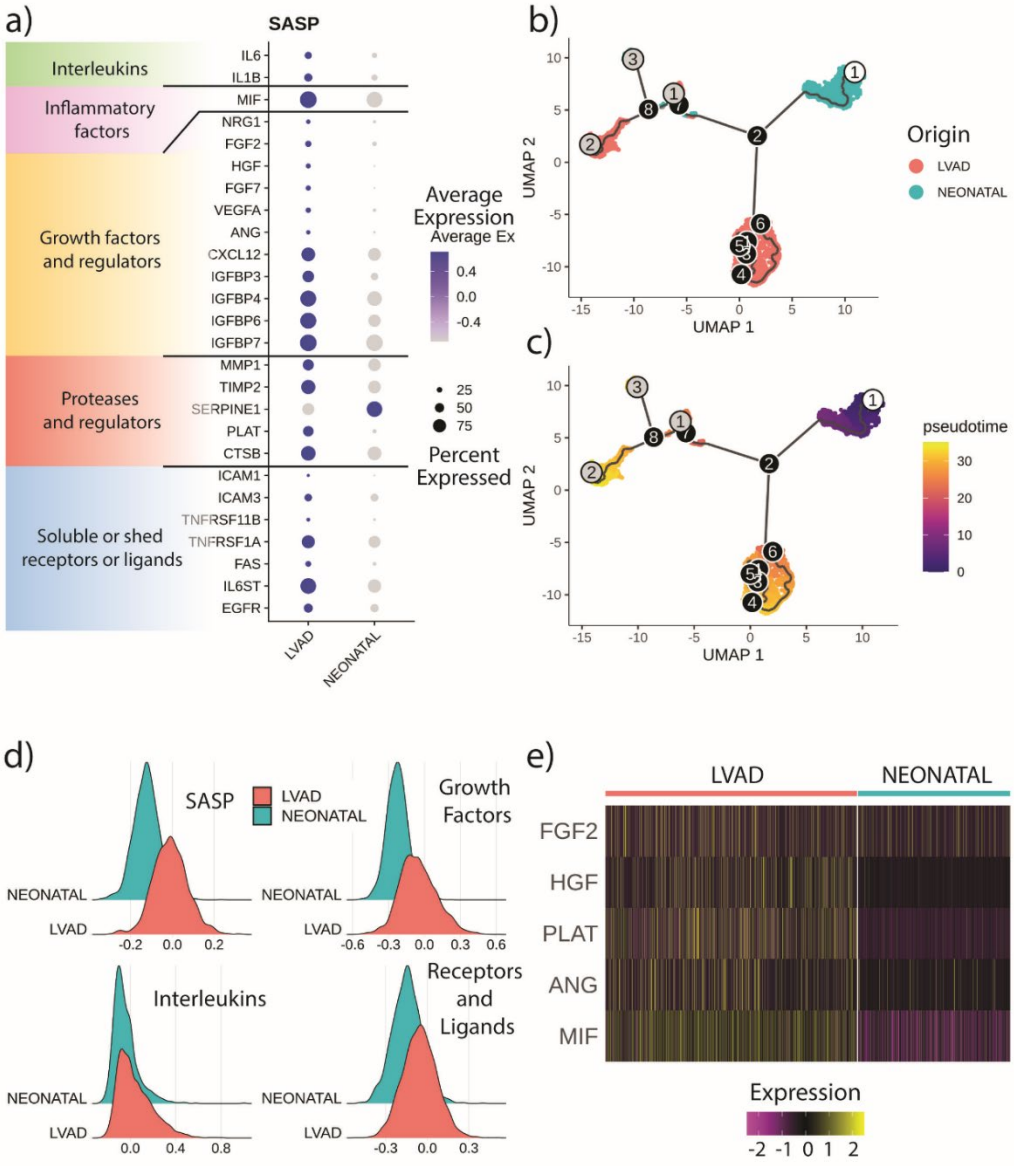

Figure 2.3 Senescent Associated Secretory Phenotype factors (SASPs) elevated in LVAD derived cells.

a) Dotplot representing expression of SASPs genes in both populations. Circle diameter represents the percentage of cells expressing a particular gene, while normalized average expression is represented by color intensity. Monocle generated UMAP projection of cCICs color-coded according to b) population of origin and c) calculated pseudotime analysis. Pseudotime transcriptional trajectory visualized by line across UMAP projection. Origin indicated by white number one circle. Nodes annotated in black circles and leaves numbered in gray. d) Ridge plots representing cell distribution on neonatal and LVAD populations and their respective calculated module scores for Senescent Associated Secretory Phenotype factors (SASPs), growth factors, interleukins and receptors and ligands. e) Heatmap representing single cell expression of paracrine and secreted factors from Neonatal and LVAD cCICs.

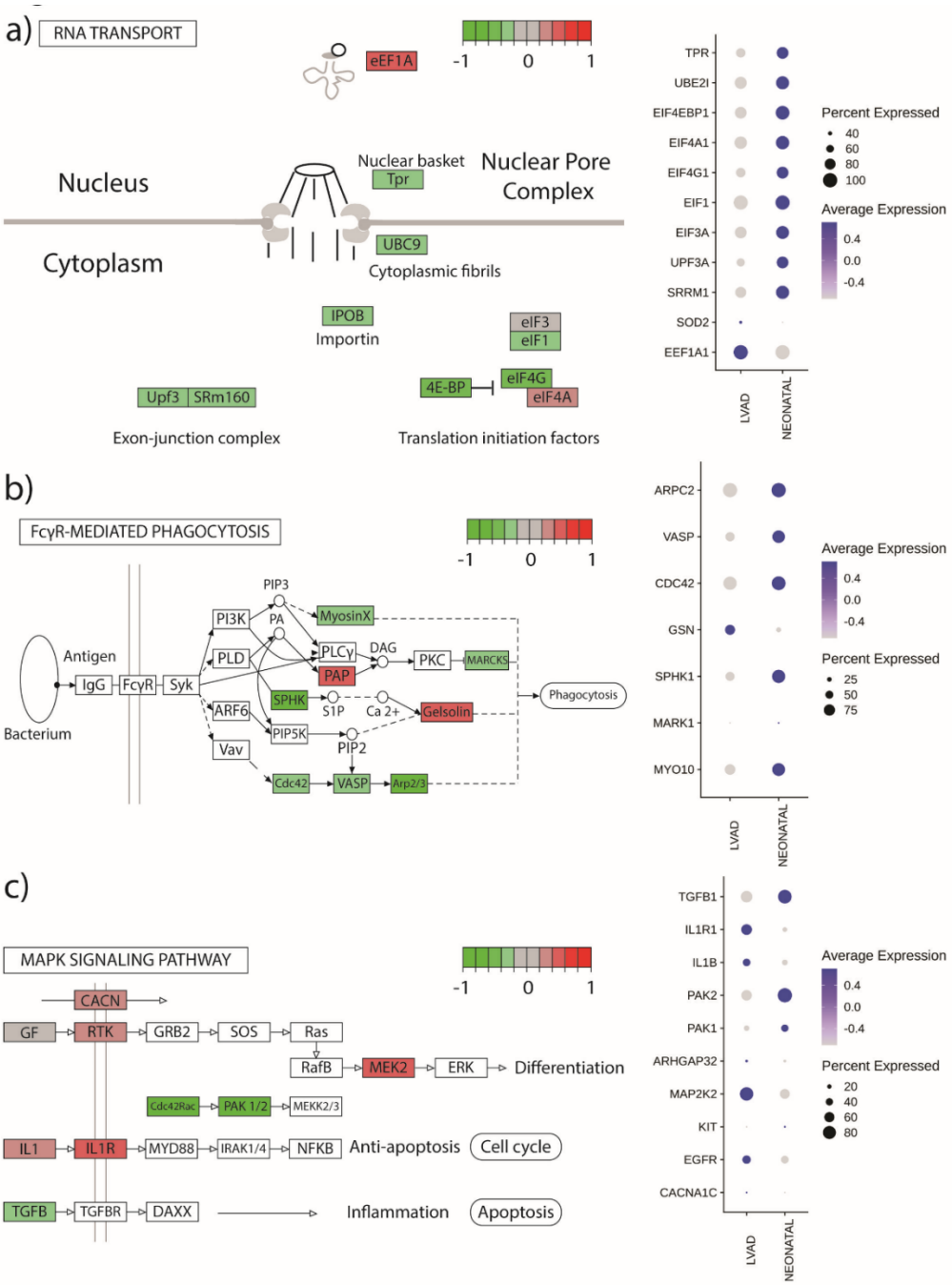

Figure 2.4 RNA transport pathway deregulated in LVAD derived cells.

Simplified KEGG pathway analysis derived from differential expression analysis and Dotplot representing expression of genes involved in a) RNA transport, b) FcγR-mediated phagocytosis and c) MAPK signaling pathways. Panels simplified from original analysis (SF 6-8). Genes in KEGG pathway analysis are color-coded in green when upregulated in Neonatal samples and red when upregulated in LVAD derived cells. In dotplot circle diameter represents the percentage of cells expressing a particular gene, while normalized average expression is represented by color intensity.

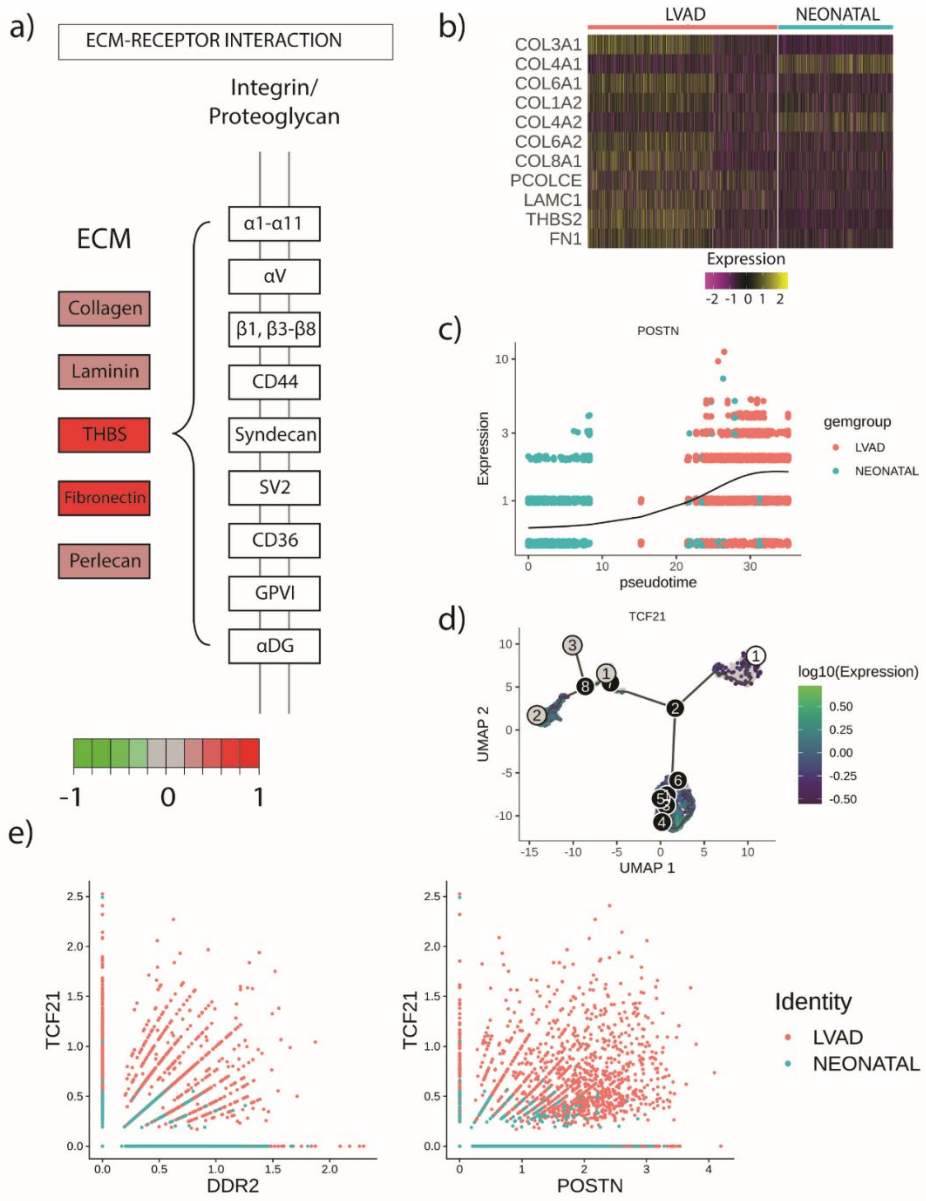

Figure 2.5 LVAD derived cells primed with a fibrotic transcriptional phenotype.

a) KEGG pathway analysis derived from differential expression analysis of genes involved in ECM-Receptor interaction pathway. Panels simplified from original analysis (SF 9). Genes in KEGG pathway analysis are color-coded in green when upregulated in Neonatal samples and red when upregulated in LVAD derived cells. b) Heatmap representing single cell expression of extracellular matrix factors in Neonatal and LVAD cCICs. c) Scatter plot representing expression of POSTN plotted against calculated pseudotime. Pseudotime transcriptional increased visualized by line across scatter plot. d) Monocle generated UMAP projection of cCICs color-coded according to TCF21 expression. Pseudotime transcriptional trajectory visualized by line across UMAP projection. Origin indicated by white number one circle. Nodes annotated in black circles and leaves numbered in gray. e) Scatter plot visualizing co-expression of fibroblast markers DDR2 vs TCF21 (left) and POSTN vs TCF21 (right).

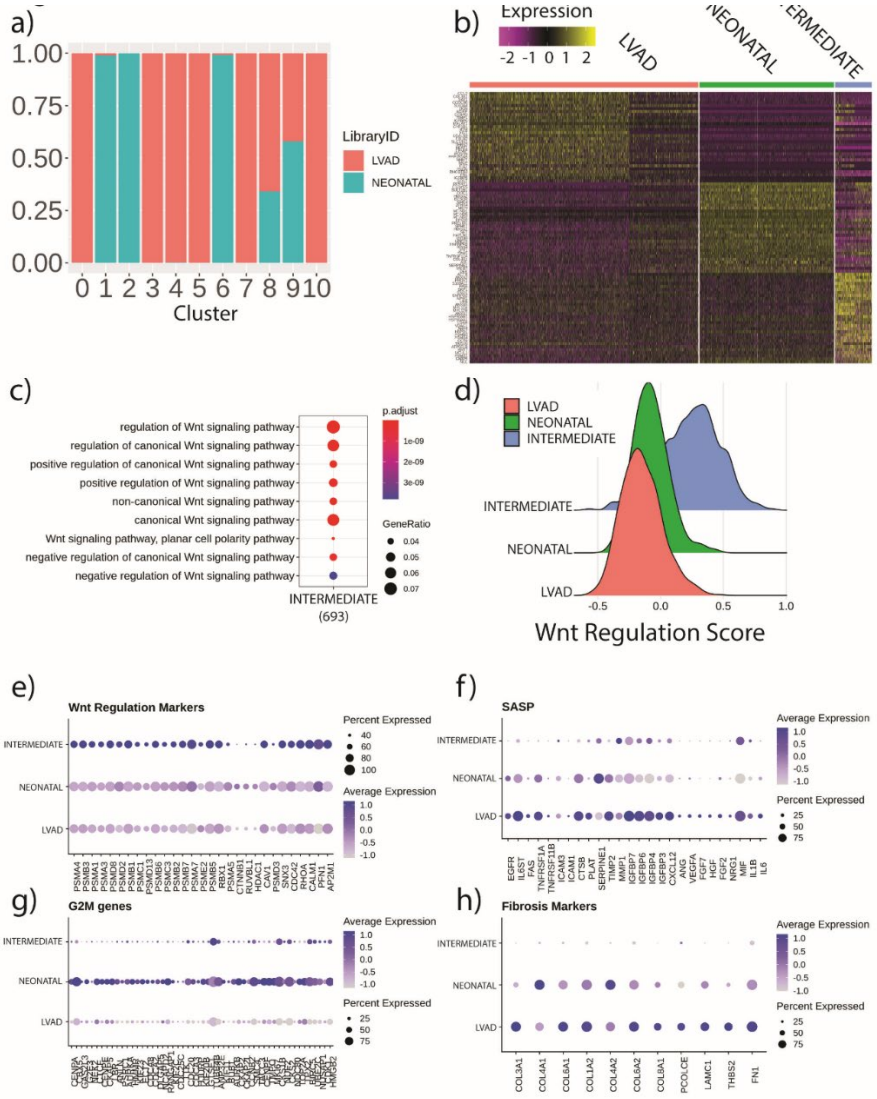

Figure 2.6 Neonatal and LVAD overlapping cells overexpress Wnt signaling regulators and sustain a hybrid phenotype.

a) Relative contributions of Neonatal or LVAD derived cCICs to each unsupervised cluster as shown in UMAP (Fig 1b). b) Heatmap representing the top 30 differential expressed genes from exclusively Neonatal and LVAD cCICs and Intermediate cells. c) Wnt regulation GO terms results from Gene Ontology analysis annotated by Biological Process. Circle diameter represents the gene ratio from the 693 DEGs being expressed in the Intermediate cells, while significance level is color-coded according to heatmap scale. d) Ridge plots representing cell distribution on neonatal and LVAD populations and their respective calculated module scores for Wnt Regulation. Dotplot representing expression of e) Wnt Regulation markers, f) SASPs, g) G2M-specific genes and h) fibrosis markers in both unique and overlapping populations. Circle diameter represents the percentage of cells expressing a particular gene, while normalized average expression is represented by color intensity.

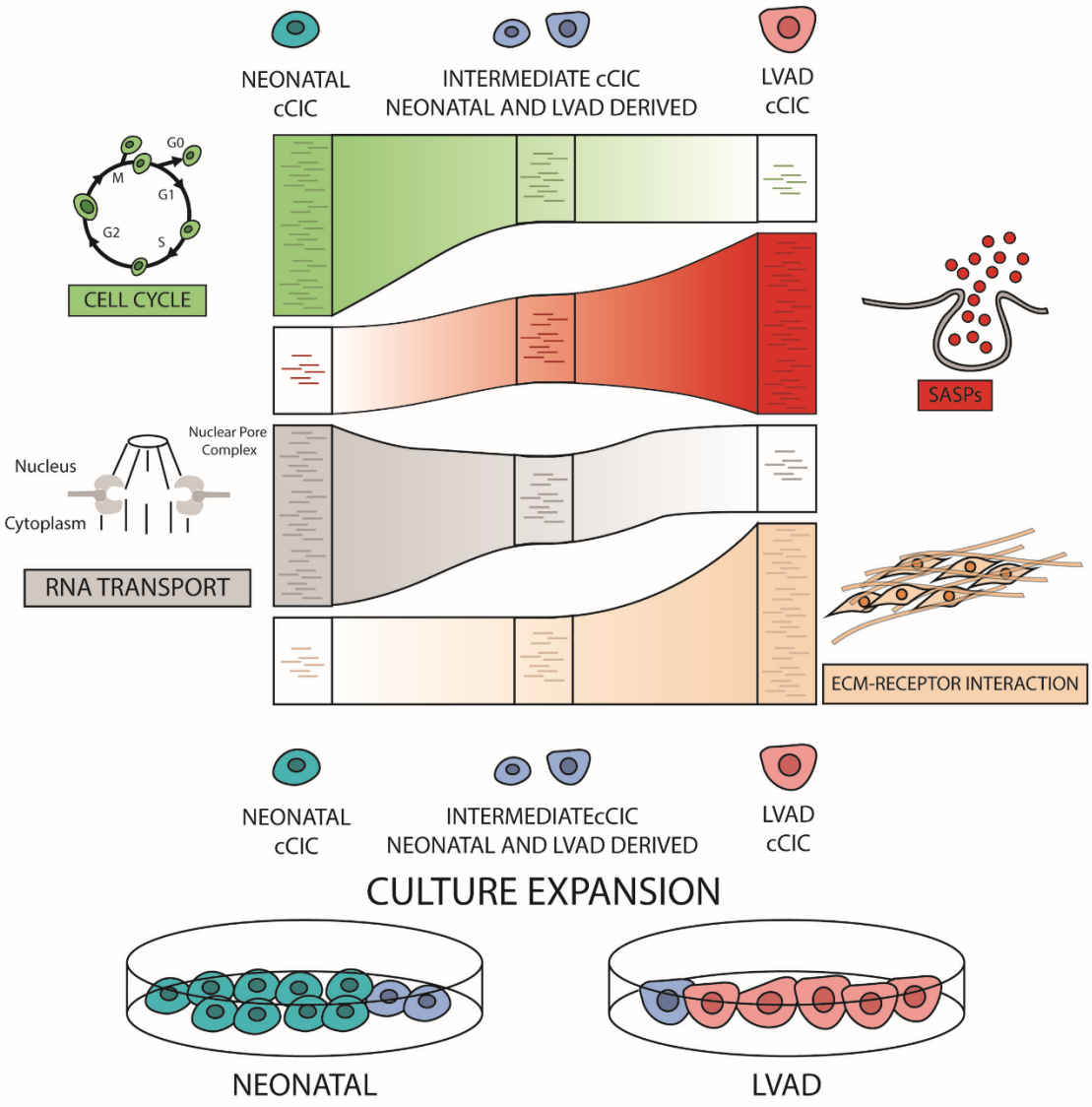

Figure 2.7 Transcriptional features of biological age are maintained following culture adaptation of cCICs.

Schematic of in vitro expanded cCICs displaying transcriptional phenotype retained by Neonatal and LVAD derived cells.

CHAPTER 3
Cardiovascular consequences of vaping

3.1 Abstract

Purpose of review: Vaping activity continues to increase worldwide. Promoted as a "healthier" alternative to traditional smoking, emerging evidence indicates "healthier" should not be confused with "harmless". Direct inhalation exposure of the respiratory tract in experimental research demonstrates pulmonary consequences of vaping. However, cardiovascular consequences of vaping are poorly characterized and are a priority area of research to reveal vaping-induced pathogenesis.

Recent findings: Alterations in cardiovascular homeostasis, inflammation, and molecular changes following vaping exposure demonstrate vaping-related health concerns.

Summary: This review summarizes cardiovascular consequences of vaping from cumulative research findings. Strategic application of emerging technologies to understand the impact of vaping upon the cardiovascular system will be essential for defining the true risks of vaping-associated injury.

Keywords: 3-5 Vaping, electronic cigarettes (E-cig), cardiopulmonary, vascular, cardiovascular disease, research.

3.2 Introduction

Vaping continues to gain popularity over the last decade across a diverse spectrum of users. In 2018 an estimated 14.9% of U.S. adults over 18 years old reported use of electronic cigarettes (E-cig)[94]. Use among youth has also increased with 19.6% of U.S. high-school students and 4.7% middle school students using E-cigs as of 2020[95]. Ill-conceived distribution of so called "Dank Vapes" contributed substantially to hospitalizations with 2,807 patients suffering from E-cig or vaping product use-associated lung injury (EVALI) in the U.S. as of February of 2020[96,97]. Clinical trials report acute impact of E-cig and nicotine use on cardiac physiology[98–100]* with pathological and economic costs derived from long-term exposure still being delineated[101,102]. Documented smoke-related cardiovascular disease (CVD)[103] and the associated financial burden on healthcare[104,105] foreshadows the future of vaping-associated CVD. Information on the intersection between vaping and cardiovascular health and homeostasis is still in early stages with a clear need for additional research to define susceptibility of cardiac structure and function to vaping.

Systemic biological consequences of vaping are too broad to consider in a short overview of the field. Therefore, this review focuses upon cardiovascular health and vaping with an emphasis upon recent trends and future directions. For detailed information on vaping-related impact on lung, vasculature, and other biological aspects, there are excellent recent reviews covering these subjects in depth[106–109]. Topics addressed here on the consequences of vaping include: 1) cardiovascular health, function, remodeling and homeostasis, 2) cardiac cell and molecular biology, 3) impact from localized and systemic immune responses, and 4) consideration of emerging technologies and experimental approaches. Evaluation of current research is necessary for planning approaches that will ultimately mitigate morbidity and mortality consequential to vaping.

3.3 Impact on Cardiac Structure and Function

Adverse effects of vaping have been observed in lungs with growing evidence indicating involvement of the heart and pulmonary circulation as well as deleterious impact upon function[110]*. Vaping can lead to acute respiratory distress syndrome (ARDS) in severe cases which is characterized by pulmonary hypertension and remodeling of the blood vessels of the lung[109,111,112](Fig. 3.1). Increased vascular resistance drives right ventricular dysfunction, exacerbating cardiopulmonary damage. Acute cardiomyopathic events are rare and often reversible[113*], however subsequent development of heart failure has also been documented[114]. Potential preventive and therapeutic approaches require insight derived from integrative examination of subject/vaping interactions, which includes chemical makeup and toxicity of vaping liquids, responses in subject's comorbidities and impact on cardiac tissue and cellulome.

Nicotine, propylene glycol/vegetable glycerin (PG/VG), other E-cig components and their byproducts are detrimental to cardiovascular health[115]. Nicotine is a highly addictive sympathoexcitatory drug, increasing heart rate and blood pressure and causing vasospasm during acute administration. Increased sympathetic stimulation can increase risk of arrhythmias and ischemia[116]. Numerous confounding effects, such as sensitization and desensitization responses, individual differences, and unclear dose-response ratios complicate simple interpretation of nicotine effects upon the cardiovascular system[117]. A murine model of high level nicotine exposure results in both systemic and pulmonary hypertension and subsequent right ventricle remodeling[118]. Systemic hypertension was present only during the first three weeks of exposure until development of nicotine-tolerance. However, at 8 weeks right ventricular systolic pressure was increased accompanied by increased right ventricular internal diameter, wall thickness, and MAPKs activation indicative of remodeling. Inhaled nicotine led to right ventricular remodeling mediated

by Angiotensin II type 1 receptor by acting upon the renin-angiotensin system [119*]. Administration of nicotine to young rats induced ROS production, promoting cardiomyocyte death by interfering with mitophagy and the intrinsic apoptotic pathway[120]. E-cig aerosol promotes alterations in a similar manner to tobacco smoke by promoting myocardial oxidative stress and inflammation leading to fibrosis[121]. As with tobacco cigarettes, recent studies found an association between E-cig use and self-reported hypertension in the population [122]and measured systemic hypertension in animal models [123]*, mainly driven by nicotine's effect on vasoconstriction and elevation of systemic vascular resistance. Combustible cigarettes cause a greater increase in sympathetic stimulation compared to E-cigs[116]. Labeling inaccuracies and elevated nicotine concentrations pose novel risks not inherent to combustible cigarettes [124]. Moreover, it is still not known if subsequent increases in adrenaline level have clinically relevant cardiovascular effects among vapers.

Although non-nicotine components and byproducts are more abundant in combustible cigarettes compared to electronic cigarettes, the presence and variety of these components in vape aerosol together with systemic and cardiovascular impact should not be underestimated. Flavoring additives to vaping juice are of particular interest, such as electrophysiological effects of toxic aldehydes such as vanillin and cinnamaldehyde [125]*. Flavoring aldehydes increased sympathetic stimulation compared to fruit-flavored e-vapor. Additionally, oxidizing compounds, metals, volatile organic compounds, carbonyls, and other components in E-cig vapor are dangerous for the circulatory system [126]. Further experimental and clinical assessment is needed to determine the impact of heterogeneous byproducts present in vape aerosol.

Vaping is particularly problematic in patients with underlying health conditions due to increased susceptibility to damage from acute and chronic insults. Administration of nicotine to

rats increased myocardial infarct size [127]. A high-fat diet and E-cig smoke with nicotine exposure decreased left ventricular contractility with increased apoptosis and structural alteration of the heart in mice[128]*. Thus, pre-existing conditions and comorbidities are likely to contribute significantly to vaping-induced CVD.

3.4 Vaping consequences on the vascular endothelium

Cardiac endothelium plays a significant role in the control of vascular relaxation/contraction. The established relationship between smoking-mediated endothelial dysfunction and cardiovascular disease[129,130] supports the importance of understanding vaping exposure upon endothelial health. A randomized controlled trial showed reduction in endothelial dysfunction on individuals switching from tobacco cigarettes to vaping, independently of nicotine content of the latter[131]. Impaired flow-mediated dilation (FMD), a metric for endothelial dysfunction and a predictor of cardiovascular risk, was reported in acute smokers but not E-cig vapers[132]. In contrast, tobacco cigarettes and JUUL E-cig decreased FMD at comparable levels[133]. Blood biomarkers of inflammation were increased and FMD decreased after a single episode of E-cig inhalation in otherwise healthy adults[134]. These superficially irreconcilable results could be explained due to the diversity of exposure protocols, *in vivo* models, variation in voltage settings, and E-cig brands in each study.

In addition to dysfunction, vascular oxidative stress[135,136], decreased of vascular endothelial growth factor (VEGF) expression, and a reduction of the density of capillaries have been reported[137]. There is significantly increased carotid plaque burden that young adult smokers and vapers exhibit compared to matched nonsmokers[138]*. Increased atherosclerotic lesions, burden and risk mediated by TLR9 pathway in response to vaping exposure was demonstrated in a mouse

model[139]*. Increased circulating endothelial progenitor cells, increased acute microvascular endothelial dysfunction, and arterial stiffness are additional factors altered in E-cig studies[140,141]. Evidence for long-term effects of vaping upon the circulatory system is lacking, but available data suggest E-cigs shouldn't be marketed as "safe" alternatives to cigarettes. However, vaping could mitigate smoking endothelial dysfunction in the short-term when employed as a smoking cessation strategy. However, E-cigs are not innocuous and further research is required to clarify discrepancies in the field and evaluate health and safety consequences of long-term vaping exposure.

3.5 Cellular and Molecular Response to E-Cigarettes in the Cardiovascular System

Mitigating strategies and therapeutic approaches require identification of pathways driving cardiac pathology as well as insight regarding molecular responses to E-cig. Molecular processes such as inflammation and reactive oxygen species (ROS) contribute significantly to CVD and vaping pathologies. Disruption in the balance of pro- and antioxidant systems in vasculature is associated with arrhythmias and myocardial remodeling due to pathogenic hypertrophy and apoptotic signaling[142]. E-cig exposure increases ROS in cardiomyocytes and aortic tissue vas detected by dihydroethidium (DHE) fluorescence[123,135,143]. Increased ROS coincided with decreased endothelial nitric oxide synthase (eNOS) following 3 days of exposure in mice, suggesting that decreased antioxidant nitric oxide is involved in the increase in oxidative stress[135]. The oxidative stress phenotype was alleviated by knocking out the ROS-producing enzyme NADPH Oxidase Subunit 2 (NOX2), confirming that oxidative stress is NOX2 dependent[135]. It is unclear the extent to which ROS accumulation observed in animal E-cig exposure studies translates to chronic users.

The cellular response to E-cig exposure is vital to understand mechanisms of pathogenesis. RNA-sequencing data of iPSC-derived cardiomyocytes exposed to E-cig extract for 2 days *in vitro* altered gene expression signatures for proliferation and apoptosis[143]. Notably, natriuretic peptide B (NPPB) upregulation was observed alongside downregulated myosin light chain kinase (MYLK) and troponin I3 (TNNI3). Proper levels of these proteins are essential for healthy heart function and appropriate stress responses. Increased apoptotic nuclei and increased cleaved-caspase 3 protein levels were reported in a high-fat diet/E-cig exposure study [128]. Increased apoptosis appears related to dysregulation of the AMPK pathway, since apoptosis regulator AMP-activated protein kinase (AMPK) was decreased in E-cig exposed mice with no expression of its downstream target Acetyl-CoA carboxylase (ACC)[128]. Cellular and molecular responses to vaping implicate increased oxidative stress and apoptosis, but data correlating these risk factors with reported pathology is still lacking. Further characterization of the signaling pathways and mechanism for vaping-induced molecular stress and damage such as vascular dysfunction, inflammation, remodeling, and impaired function are required to inform the public of the risks associated with E-cig use and will be essential for development of therapeutic interventions.

3.6 Innate and Adaptive Immune Response to E-Cigarettes

The innate and adaptive immune response to E-cig exposure has been predominantly examined in the pulmonary system and to a lesser extent in the cardiovascular system[144–149]. Sustained inflammation caused by typical recurring vape exposure could lead to downstream toxicity from oxidative stress and exert compounding effects to increase risk for cardiovascular disease. Additionally, immune response to vaping could exacerbate risk for CVD such as atherosclerosis and coronary artery disease. Environmental stressors such as E-cig vapor promote

macrophage transition into foam cells which build up in arteries as atherosclerotic plaques[150]. E-cig exposure for 16 weeks in ApoE−/− mice led to development of atherosclerotic plaques with increased levels of Mac2+ macrophages compared to controls[139]. Inhibition of TLR9 ameliorated the phenotype suggesting that TLR9 is mediating the atherosclerotic response. Additionally, macrophage marker CD68 was found to have increased protein levels in the aorta of mice following acute E-cig exposure[135]. Human studies have reported conclusions consistent with animal studies reporting increased levels of lymphocytes, monocytes, and neutrophils in the blood of E-cig users compared to non-users[151]*.

Increased levels of inflammatory cytokine IL-6 in blood has been reported in both human and mouse models of E-cig exposure following a wide range of exposure time lengths[135,139,152,153]*. Other cytokines including ICAM-1, MCSF, MCP-1, and IL-8 increase following acute exposure times in humans but it is unclear whether this is a transient response to initial E-cig exposure or if the inflammatory response is sustained long enough to be associated with pathogenesis[152,153]. Analysis of immune cell populations and signaling in animal studies on a timescale analogous to decades in humans can serve as approximations of future risk for E-cig users. The current SARS-CoV-2 (COVID19) pandemic[154,155]* drew attention regarding concerns related to immune system response following infection when combined with E-cig exposure. Alterations of immunocompetency pursuant to vaping are likely to have as yet poorly understood consequences for cardiopulmonary protection and homeostasis.

3.7 Emerging technologies and experimental approaches

Emerging consequences of vaping on cardiovascular homeostasis will require real-time solutions, creative experimental approaches, and innovative therapeutic approaches. Fortunately, state-of-the-art and high throughput technologies continue to be developed with some already

deployed to elucidate the impact of vaping. Single-cell and nuclei RNA sequencing (sc/snRNA-Seq) has proven to be a valuable tool to characterize the lung changes in response to senescence[156], fibrosis[157] and smoking[158]. Exploration of the cardiac transcriptome has yielded a remarkable framework to study the biological diversity, interplay, and plasticity of identified cardiac cell subpopulations. Single-cell transcriptional analysis has revealed the phenotypical diversity and intercommunication within the murine cardiac cellulome at the baseline[17] and under chronic cardiac fibrosis[85]*. Cardiac topology and chamber-specific transcriptional signatures of the human heart have been contextualized with genes implicated in cardiomyopathies using snRNA-Seq[57]. Dynamic interactions and insight on immune changes following acute injury in mouse models via myocardial infarction[84,159] or ischemia reperfusion[160]* have been derived from using scRNA-Seq platforms. Vaping effects on cardiac development can be cross-referenced to published datasets of temporal and chamber-specific benchmarks of cardiac development [6,161]. Framework to assess changes on *in vitro* phenotypes and protocols of culture expanded cardiac cell will be critical to evaluate the influence of vaping[18,162]. Organism-wide transcription cell atlas like the Tabula Muris project[28] and the Mouse Cell Atlas[163,164] can be used as baselines for comparison of cardiac and systemic changes derived from vaping exposure. New technologies and approaches in transcriptional analysis are currently underway to determine the impact of vaping upon cardiovascular biology. Paradigm development will benefit from high-throughput technologies targeting the proteome and secretome including mass spectrometry and mass cytometry[165], together with epigenomic platforms, and spatial approaches recently adopted to address standing biological questions of intercellular heterogeneity and communication.

3.8 Future considerations

Vaping popularity and activity continue to evolve with diverse, complex, and dynamic societal pressures advancing E-cig adoption and product development. Cardiopulmonary effects and documentation of pathogenesis continues to benefit from research studies tackling the complex and diverse array of possible exposure regimens (Fig. 3.2, Table 3.1). Acute consequences of vaping exposure include changes in pulmonary hypertension, cardiac remodeling, function, arterial pressure and stiffness, and cell and molecular changes (Fig 3.1 & 3.2, Table 3.1). Long-term cardiovascular effects of recreational vaping will eventually be revealed in decades ahead, as popularization of the vaping lifestyle is a relatively recent phenomenon, in the near term, implications of acute and chronic vaping for cardiopulmonary health will be revealed through carefully executed studies that reveal vaping impact.

Datasets[166], research observations, and experimental strategies for assessing vaping pathogenesis can be rooted in the approaches and concepts derived from the decades-long pursuit of biological studies on traditional cigarette smoking. Experimental animal models of chronic exposure with vaping protocols relevant and comparable to human recreational vaping will be crucial to evaluate long-term progression of cardiovascular health. Experimental approaches should consider cardiac cellular composition, heterogeneity, and topology, together with constraints inherent in handling and preservation of mammalian cardiopulmonary tissues.

3.9 Conclusion

In conclusion, there is a profound need for thoughtful and translationally relevant research to address cardiovascular consequences of vaping. New devices, vape juice mixtures and trends continue to be introduced, increasing variation among previous as well as ongoing studies. A

composite strategy incorporating robust longitudinal assessments to investigate vaping-induced pathogenesis will need to account for variability of available products and experimental designs. Clinical evaluations of right ventricular systolic and diastolic function have been centered on ARDS patients[167,168]. However, signs of right ventricular dysfunction such as chest discomfort and breathlessness manifest only after left ventricular function is compromised, ultimately complicating early assessment of pulmonary involvement[169]. Right ventricular remodeling observed in a mouse vaping model[170]* implicates cardiopulmonary consequences that can contribute to not only cardiac remodeling but also increased risk for secondary debilitating conditions. Current studies suggest a correlation between vaping and atherosclerosis, but additional experimental and clinical data is needed to define causality. Another area worthy of attention is the study of cell and molecular processes potentially affected by vaping, such as mitochondrial metabolism and energetics, stress response and genotoxicity.

Collectively, these considerations emphasize the need for promotion and expansion of vaping research. Associations between harm perception and desire to quit vaping have been established[171], which can be further reinforced by the scientific community contribution of elucidating mechanisms of vaping-induced pathology. Establishing a mechanistic basis of vaping-induced pathogenesis is critical for development of preventative and therapeutic interventional strategies. Efforts to curb the pathologic consequences of vaping are likely to involve multiple and potentially distinct approaches for young versus aged users. Fundamental research at tissue, cellular, molecular, and physiologic levels needs to keep pace with vaping industry initiatives and campaigns. Only through investment and expansion of research efforts on vaping will society be able to implement interventions designed to mitigate progression of injury and prevent irreversible damage, thereby fostering repair and recovery.

3.10 Key points

- Adverse effects of vaping have been observed with growing evidence indicating impact in cardiac structure as well as deleterious impact upon function.
- Current research suggest E-cigs are not innocuous for cardiac endothelium, localized immune cell populations and overall cardiovascular homeostasis.
- Further research is required to clarify discrepancies in the field and evaluate health and safety consequences of long-term vaping exposure.

3.11 Acknowledgements

This work was supported by NIH grants R01HL135661-02. Chapter 3, with slight modifications, is a reprint of the material as it will appear in Current Opinion in Cardiology, 2022. Cardiovascular consequences of vaping. Oscar Echeagaray, Clarissa Savko, Andrea Gallo, and Mark Sussman. The dissertation author was the primary author and investigator on this manuscript.

3.12 Figures

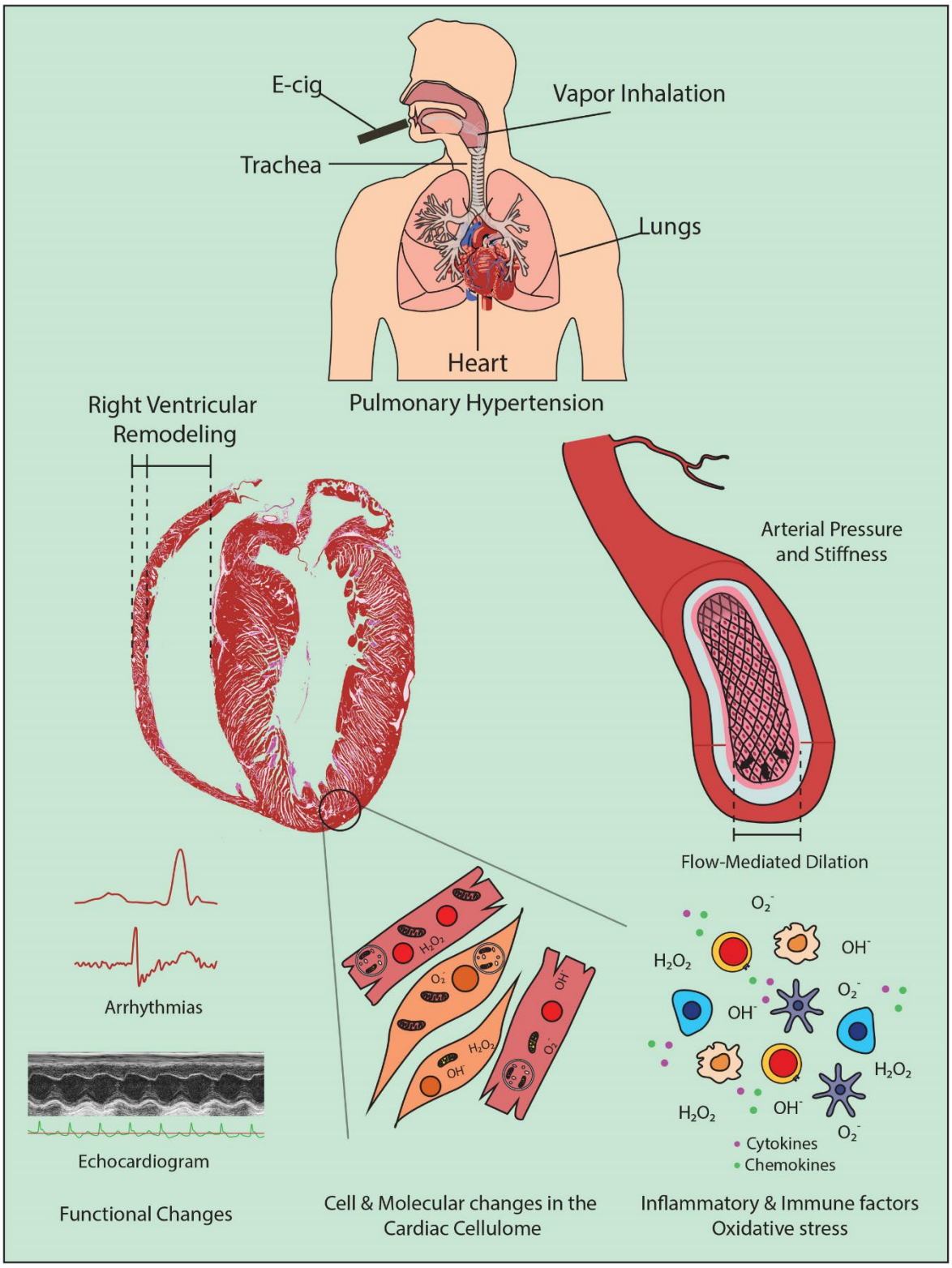

Figure 3.1 Summary of reported cardiovascular consequences of vaping.

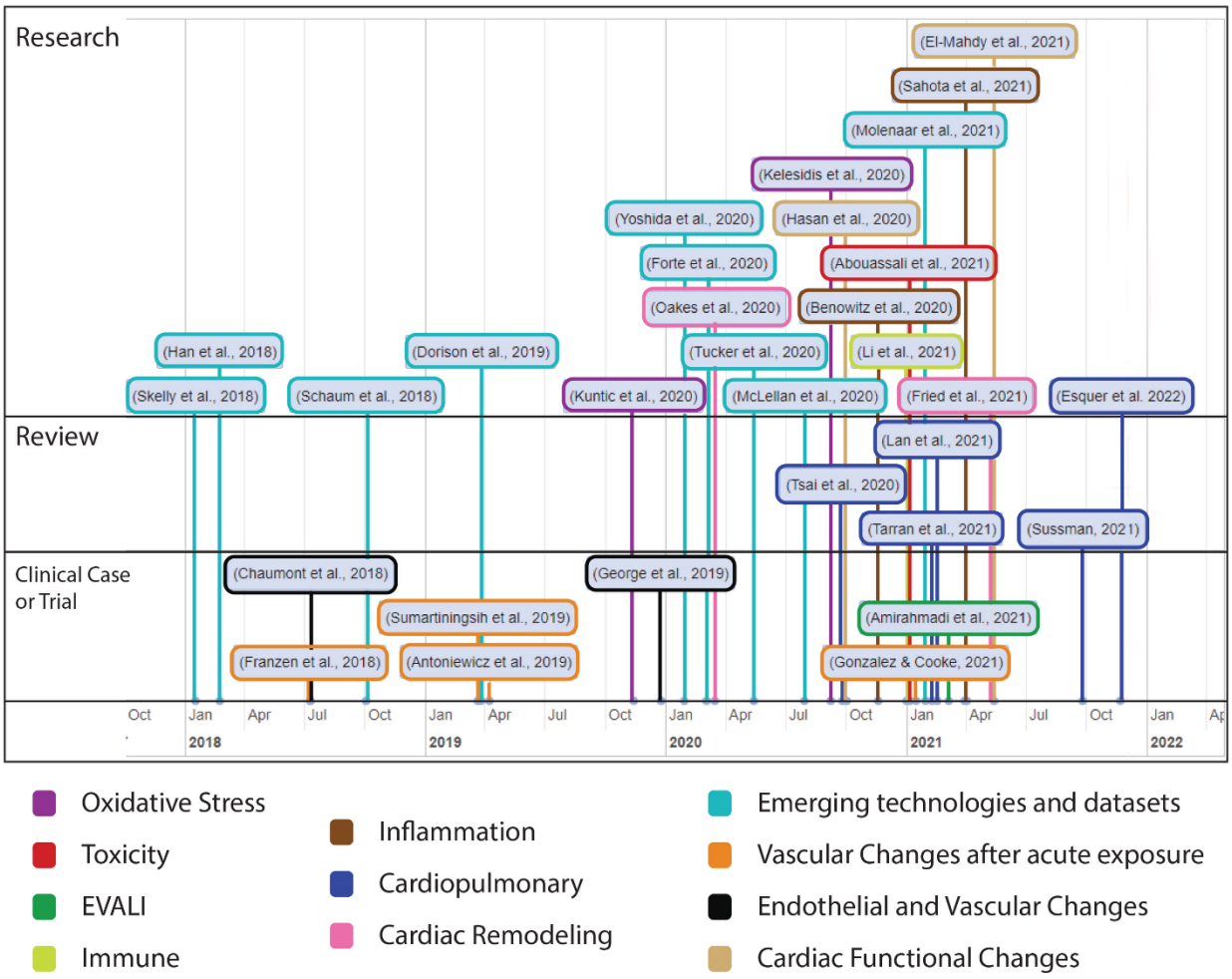

Figure 3.2 Cardiovascular consequences of vaping research timeline

Table 3.1. Selected papers of interest on cardiovascular consequences of Vaping.

Authors	Reference	Article type	Title	Keywords
(Esquer et al. 2022)	[170]	Research	Fundamentals of vaping-associated pulmonary injury leading to severe respiratory distress.	Cardiopulmonary, Cardiac Remodeling and Functional Changes
(Li et al. 2021)	[139]	Research	Electronic Cigarettes Induce Mitochondrial DNA Damage and Trigger TLR9 (Toll-Like Receptor 9)-Mediated Atherosclerosis.	Immune
(Benowitz et al. 2020)	[152]	Research	Twenty-Four-Hour Cardiovascular Effects of Electronic Cigarettes Compared With Cigarette Smoking in Dual Users.	Inflammation
(Kelesidis et al. 2020)	[151]	Research	Elevated Cellular Oxidative Stress in Circulating Immune Cells in Otherwise Healthy Young People Who Use Electronic Cigarettes in a Cross-Sectional Single-Center Study: Implications for Future Cardiovascular Risk.	Oxidative Stress, Inflammation
(Fried et al. 2021)	[119]	Research	Angiotensin II type 1 receptor mediates pulmonary hypertension and right ventricular remodeling induced by inhaled nicotine.	Cardiac Remodeling
(El-Mahdy et al. 2021)	[123]	Research	Long-term electronic cigarette exposure induces cardiovascular dysfunction similar to tobacco cigarettes: role of nicotine and exposure duration.	Cardiac Functional Changes
(Raymond et al. 2018)	(31)	Research	The nicotine content of a sample of E-cigarette liquid manufactured in the United States.	Nicotine content of e-liquid samples
(Hasan et al. 2020)	[128]	Research	Electronic cigarettes cause alteration in cardiac structure and function in diet-induced obese mice.	Cardiac Functional Changes
(Amirahmadi et al. 2021)	[113]	Clinical case or Trial	Electric cigarette-related lung injury and cardiovascular insult.	EVALI
(Sahota et al. 2021)	[138]	Research	Atherosclerosis inflammation and burden in young adult smokers and vapers measured by PET/MR.	Inflammation
(Abouassali et al. 2021)	[125]	Research	In vitro and in vivo cardiac toxicity of flavored electronic nicotine delivery systems.	Toxicity
(Lan et al. 2021)	[155]	Review	Right Ventricular Damage in COVID-19: Association Between Myocardial Injury and COVID-19.	Cardiopulmonary
(Tsai et al. 2020)	[110]	Review	Effects of e-cigarettes and vaping devices on cardiac and pulmonary physiology.	Cardiopulmonary
(Gonzalez & Cooke, 2021)	[99]	Clinical case or Trial	Acute effects of electronic cigarettes on arterial pressure and peripheral sympathetic activity in young nonsmokers.	Vascular Changes after acute exposure
(McLellan et al. 2020)	[85]	Research	High-Resolution Transcriptomic Profiling of the Heart During Chronic Stress Reveals Cellular Drivers of Cardiac Fibrosis and Hypertrophy.	Emerging technologies and datasets
(Molenaar et al. 2021)	[160]	Research	Single-cell transcriptomics following ischemic injury identifies a role for B2M in cardiac repair.	Emerging technologies and datasets

CHAPTER 4
Fundamentals of vaping-associated pulmonary injury leading to severe respiratory distress

4.1 Abstract

Vaping of flavored liquids has been touted as safe alternative to traditional cigarette smoking with decreased health risks. The popularity of vaping has dramatically increased over the last decade, particularly among teenagers who incorporate vaping into their daily life as a social activity. Despite widespread and increasing adoption of vaping among young adults, there is little information on long-term consequences of vaping and potential health risks. This study demonstrates vaping-induced pulmonary injury using commercial JUUL pens with flavored vape juice using an inhalation exposure murine model. Profound pathological changes to upper airway, lung tissue architecture, and cellular structure are evident within 9 week of exposure. Marked histologic changes include increased parenchyma tissue density, cellular infiltrates proximal to airway passages, alveolar rarefaction, increased collagen deposition, and bronchial thickening with elastin fiber disruption. Transcriptional reprogramming includes significant changes to gene families coding for xenobiotic response, glycerolipid metabolic processes, and oxidative stress. Cardiac systemic output is moderately but significantly impaired with pulmonary side ventricular chamber enlargement. This vaping-induced pulmonary injury model demonstrates mechanistic underpinnings of vaping-related pathologic injury.

4.2 Introduction

Relative merit of vaping for "harm reduction" intervention that transitions smokers away from combustible cigarettes remains under attack because of widespread adoption of vaping as a social activity and lifestyle choice by "never smokers," particularly adolescents [172–174]. The electronic vaping-associated lung injury (EVALI) outbreak of 2019 serves as a sobering demonstration of potential dangers resulting from uninformed experimentation with vape juice composition [175–177]. In comparison, commercially sold vape juices and prefilled disposable devices

typically do not provoke acute lung injury and respiratory distress as pointed out by vaping advocacy groups [178–180]. However, vaping-associated pulmonary injury (VAPI) in a minority of users is a well-documented and growing concern in the clinical setting with multiple independent reports of severe respiratory illness including acute respiratory distress syndrome including potential pulmonary circulation impairment [107,114,181–186]. Life-threatening consequences of VAPI emphasized by high profile media coverage over the last couple of years have raised public awareness of danger linked to vaping [187–190] with increased calls for regulatory oversight and expanded research [191,192]. Fundamental unresolved issues using commercial vaping products from reputable sources include (1) how do individual specific biological factors influence susceptibility to VAPI; (2) what is the underlying pathogenesis of VAPI leading to respiratory distress; and (3) how does progression of VAPI precipitate pulmonary circuit failure? Immediacy of the problem in society, recency of modern electronic vaping, and the rapid evolution of vaping technology necessitate development of an innovative platform to study biological processes of VAPI.

Studies of VAPI often target specific biological processes to assess consequences for phenotypic or functional impact in cells, tissues, or animals. Assessment of vape fluid exposure in vitro is typically focused upon a particular cell type such as epithelial or vascular cells [141,146,193–195]. Alternatively, in vitro studies of mixed cell cultures offer insight into disruption of structural interactions in “organoid” settings [196]. Primary culture of explanted tissue is another option for assessing consequences of vape juice exposure [197,198]. Observation of in vitro system is advantageous for several reasons including simplifying, focusing, and increasing throughput with targeted analyses of select cell or tissue types, but extrapolating findings to the in vivo setting remain problematic without corresponding animal studies. Experimentation conducted using animal models shows varying outcomes after vape juice exposure ranging from negligible to

substantial [123,193,199,200]. Inconsistent findings are undoubtedly due, at least in part, to variability in exposure protocols. Relatively few studies provide compelling rationales for experimental design or acknowledge inherent limitations of their approach [201]. Critics of vaping research leverage issues of experimental interpretation and variation to challenge relevance of findings, leading to pitched debate between pro-versus anti-vaping advocacy groups [202,203]. Establishing reasonable approximations of human vaping behavior as well as clinical manifestations of VAPI is essential and desperately needed to advance research and promote consensus among all stakeholders.

Quintessential combined features of VAPI are most appropriately recapitulated in a mammalian inhalation exposure model. Capturing the numerous variables of human vaping activity such as (but not limited to) frequency of use, vaping inhalation topography, device type, and vape juice formulation create a daunting challenge for implementing a "typical" exposure protocol. Nevertheless, topography and demographics of vaping have been studied [204–207], whereas user preferences for devices and juices are a moving target subject to social and marketing influences [208]. Presently, JUUL remains the most popular e-cigarette device with 51.6% of the reusable market share in April 2021 and 49.7% of the entire e-cigarette market [209–211]. Vape juice preferences trend toward fruit flavors, often with the addition of menthol to provide a cooling sensation [212,213]. Considerations such as these should be collectively incorporated into experimental design if the intent is to target human behaviors and choices.

Rapid evolution of the vaping industry coupled with unpredictable trending preferences of end users can have devastating consequences such as the EVALI outbreak, which was quickly correlated to ill-conceived modifications in "Dank Vape" juices [214,215]. However, severe respiratory distress syndromes linked to VAPI are increasingly seen in the clinical setting involving vapers using commercially sourced devices and vape fluid [114,216–220]. Evolution and onset

of VAPI in otherwise healthy individuals remains poorly understood, especially on cellular and molecular levels. Thus, the emerging clinical syndrome of VAPI forms the basis of this report wherein an experimental model of inhalation exposure was developed and characterized. Findings presented here document, to our knowledge, the first VAPI inhalation exposure model instigated using popular products sourced entirely from retail markets revealing novel biological responses and pathogenic processes.

4.3 Results

4.3.1 Structural and morphometric alterations to lung parenchyma and airways following vape exposure

Tissue samples harvested following Week 9 of exposure comprised the excised respiratory tree consisting of trachea with lungs, with hearts concurrently processed as detailed in the Materials and Methods section. Termination of the study at Week 9 time point was chosen based upon longitudinal histologic observation of lung tissue exhibiting progressive pathological features of VAPI. Longitudinal time course histological assessments were performed on a small cohort of subjects beginning at Week 5 at 1-wk intervals for a small cohort (Data not shown). Overt behavioral or physiological stress was not evident from daily routine monitoring of mouse subjects throughout the Week 9 time course. Lung sections were prepared in the coronal plane and visualized for basic structure by H&E stain (Fig 4.1). Normal non-vaped lung tissue shows typical features of larger bronchi proximal to primary branch points becoming smaller toward peripheral regions, scattered vasculature of various sizes, and parenchyma with uniformly distributed alveolar areas (Fig 4.1, A1). In comparison, vaped lung shows increased staining intensity proximal to bronchi in central regions and remodeling of lung parenchyma (Fig 4.1, A2), suggesting pathological changes in bronchiolar and vascular structure. Closer visualization of bronchioles from vaped lung sections reveals wall thickening, deterioration of smooth muscle organization,

and increases in cellular infiltrates (Fig 4.1B). Large accumulations of cellular infiltrate are particularly prominent near vasculature as clusters of numerous cells concentrate around injured vessels (Fig 4.1C). Widespread alveolar rarefaction in vaped lung tissue is present with significant losses in peripheral regions as revealed by alveolar space quantitation (Fig 4.1D). Adverse remodeling of thickened bronchiole walls was also significant (Fig 4.1E). Collectively, these findings demonstrate multiple pathological abnormalities consistent with VAPI and reveal the extent and nature of damage caused by inhalation exposure in the lungs.

4.3.2 Pathologic disruption of structural organization in airway and lung tissue of vaped mice

Pursuant to findings using H&E (Fig 4.1), additional histological stains were used to further understanding of lung tissue composition. Coronal lung sections from both non-vaped and vaped mice were stained with either Pentachrome or Trichrome dye mixtures to reveal distribution of elastin fibers or collagen, respectively (Fig 4.2). Normal non-vaped lung shows densely packed elastin fibers surrounding the periphery of airway passages originating in the central bronchi and continuing into the distal airspaces. In contrast, structural organization alteration of elastin fibers in the vaped lung is evident by loss of alignment, density, and orientation relative to the airway (Fig 4.2, top row). Damage to lung architecture is prevalent in vaped tissue sections with increased collagen deposition associated with bronchial airways, vessels, and alveolar spaces compared to the non-vaped control sample (Fig 4.2, bottom row). Estimation of collagen deposition indicates a 45.69% (1.5-fold) increase in the vaped lung compared to the non-vaped group (non-vaped covered 3.46% of area; vaped covered 5.04% of area) by methyl blue stain quantitation on images. These results provide further evidence of VAPI pathology and structural abnormalities induced by inhalation exposure of vape aerosol.

4.3.3 Mucin accumulation in bronchial airways of vaped mice

Presence of mucopolysaccharides and glycoproteins in lung tissue sections was observed using periodic acid–Schiff (PAS) stain with detection visualized as a deep red Fuchsia color. PAS labeling intensity is increased in the lung tissue of vaped mice compared with non-vaped samples (Fig 4.3A). PAS stain was notably present in the epithelial lining of airway tracts in numerous large secretory vesicles. This initial finding was further confirmed by immunolabeling for mucin 5AC (Muc5AC), a major constituent glycoprotein of secretory mucus produced by goblet cells that protects airways from foreign pathogens [221,222]. Muc5AC immunolabeling is increased in bronchiolar goblet cells in the airway of vaped mice compared with non-vaped samples (Fig 4.3B). Cell membranes are visualized with immunolabeling for Epithelial-cadherin (ECAD), a cell adhesion molecule [223]. Muc5AC immunolabeling shows distribution along the apical surface of epithelial lining as expected for a secretory protein. Elevation of mucin protein expression was confirmed by immunoblot analysis of protein homogenates prepared from the right lung lobe using antibodies to Muc5AC and Muc1 (Fig 4.3C). Protein levels for Muc5AC and Muc1 were significantly increased by 3.5 ± 0.36 and 2.3 ± 0.19-fold, respectively, as determined by quantitative analysis ($P < 0.001$). Taken together, these findings demonstrate increases in PAS stain and mucin accumulation in vaped lung samples consistent with expectations for VAPI and airway epithelial tract response to expunge xenobiotic agents.

4.3.4 Pseudostratified columnar epithelium disruption in trachea of vaped mice

Upper airway epithelial lining play a critical role in the respiratory defense response to xenobiotic agents by trapping and clearing foreign pathogens [223,224]. Within the epithelial lining, ECAD serve an indispensable role in regulation of cell–cell adhesion as well as regulation of innate

immunity [225]. Thus, upper airway structure was evaluated with emphasis upon ECAD localization and protein expression level. Trachea sections from upper airway were also immunohistochemically labeled for the water-specific channel Aquaporin 5 (Aq5) [226], basal cells expressing cytokeratin 5 (Krt5), ciliated cells expressing α-tubulin, and the cytoskeletal signaling molecule tetraspanin [227–229]. Deterioration of upper airway pseudostratified epithelial organization is evident in samples from vaped mice versus non-vaped controls (Fig 4.4A and B). Normal columnar structure remodels into a multilayered cellular sheet with dysmorphic features varying from collapsed (Fig 4.4A) to hyperplastic (Fig 4.4B). Basal cell localization along the basement membrane shows irregularities and Aq5 immunoreactivity is diminished in sections from vaped mice relative to non-vaped controls. Notably, ECAD immunoreactivity is enhanced in vaped sections versus non-vaped controls (Fig 4.4A and B) prompting further evaluation by immunoblot analysis of the right lung lobe that demonstrates a significant 30% elevation of ECAD protein in the vaped lung ($P < 0.01$; Fig 4.4C). In summary, these results reveal multiple alterations of proteins involved in structural and functional properties of the lung airway and concomitant loss of pseudostratified cellular architecture in trachea epithelium.

4.3.5 Inflammatory activity increased in vaped mice

Presence of cellular infiltrates observed by H&E (Fig 4.1C) suggests the presence of an inflammatory response in the lung of vaped mice. Immunophenotyping was performed using antibody to CD11b (also known as Mac-1), an integrin primarily expressed on monocytes, macrophages, neutrophils, DCs, NK cells, and a subset of B and T cells [230,231] as well as CD11c, a marker of DCs. CD11b and CD11c immunoreactivity is increased in tissue sections from lung parenchyma of vaped mice compared to non-vaped controls (Fig 4.5A and B). Comparison of cellular density for CD11b and CD11c was determined by counting of cells in sections from two

non-vaped and four vaped mouse samples. Four images were taken per sample, each with an area of 1.32 mm2 totaling 5.27 mm2 imaged per sample. Cell count for CD11b was significantly increased by fourfold (8.875 ± 1.62 for no vape versus 35.69 ± 4.66 vape; P = 0.001. Cell count for CD11c was significantly increased by 2.3-fold (23.25 ± 7.2 no vape versus 53.19 ± 5.257 vape; P = 0.003). Additional evidence supporting enhanced inflammatory activity in vaped lung samples was provide by immunoblot analysis of lung parenchyma homogenates for immune cell markers. Expression of CD11b increased 2.5 ± 0.33-fold in vaped compared with non-vaped control samples, along with similar elevations of CD45 (2.0 ± 0.12-fold), CD206 (1.4 ± 0.07-fold), and CD11c (1.9 ± 0.16-fold) (Fig 4.5C and D). Inflammatory cytokine expression was also elevated in vaped versus non-vaped lung tissue homogenates including IL-6 (2.1 ± 0.14-fold), IL-1 (1.9 ± 0.07-fold), and high mobility group box protein-1 (HMGB-1; 1.4 ± 0.04-fold). Last, elevation of the extracellular matrix protein fibronectin (2.5 ± 0.20-fold) is indicative of inflammation and possibly tissue repair after bronchopulmonary injury [232,233]. Overall, these results indicate potentiation of inflammation consistent with VAPI in the lungs of vaped mice.

4.3.6 Transcriptome profiling of alterations induced by vape inhalation exposure

Spatial transcriptional analysis demonstrates biological effects consistent with observations from microscopy and immunoblot analyses (Figs 4.1–4.5). Transcriptional data were obtained from cryosections of upper pulmonary branches from non-vaped (NV) and vaped (V) mice (two males and two females) using the Visium platform (10× Genomics) and aligned to the murine transcriptome (Fig 4.6A). All samples displayed comparable unique molecular identifier (UMI) and detected gene expression per spot with a slight differential between lung parenchyma and upper airway tissue (Data not shown). Unsupervised clustering revealed 14 clusters throughout

all samples (Clusters 0–13), facilitating tracing of treatment-associated features within the pulmonary architecture (Fig 4.6B–D).

Spot distribution normalized to input revealed some clusters distributed in both NV and V samples (clusters 0, 3, 5, and 12; Fig 4.1E). Spots from clusters 2, 4, 8, and 10 were predominant in the NV group, whereas spots from clusters 1, 6, 7, 9, 11, and 13 were mostly present in V samples (Fig 4.6E). An expected factor driving transcriptional clustering was lung architecture as captured in the tissue section and number of transcriptionally similar spots (Fig 4.6F). Therefore, accurate interpretation of data spots required subset of lung parenchyma and upper airway for downstream analysis (parenchyma: clusters 0, 1, 2, 3, 5, 6, 7, 10, and 12; upper airway: clusters 4, 8, 9, 11, and 13; Figs 4.6D). Spot mapping identified cell types in each cluster by score, with some spots mapping to multiple cell types (Table 4.1).

Multiple cells from each lung section were captured on each spot (50 μm in diameter) of the gene expression slide, conferring the spots with hybrid transcriptome for spatial analysis. Cell type identification of hybrid gene expression spots was done by cross-referencing spatial transcriptome to the Mouse Cell Atlas (MCA) single-cell annotated database (1) (Fig 4.6A). Spot mapping identified cell types in each cluster by score, with some spots mapping to multiple cell types (Data not shown). Spot mapping mostly aligned to transcriptome annotated in the murine lung, but in some instances displaying transcriptional similarities to cell types from other tissues or developmental stages (Data not shown). Spot ratios per cluster were contextualized with the number of spot per cluster (Fig 4.6F and G). Endothelial and stromal cells were present throughout all clusters and lung regions, with some spots matching cell type subclassifications characterized by expression of particular markers (Figs 4.6G). Lung parenchyma broadly displayed transcripts distribution of annotated adipocytes, AT1, AT2, B cells, club cells, DCs, and macrophages,

whereas spots in the upper airway show higher transcript for ciliated and muscle cells (Data not shown). Clusters 0, 3, 5, and 12 predominant in parenchyma in both NV and V samples captured endothelial, stromal, ciliated cells, club cells, muscle, lower proportion adipocyte, erythroblasts, and macrophages. However, clusters overall vaped samples showed higher spatial distribution of spots mapping to MCA annotated AT1, AT2, ciliated cells, and club cells (Data not shown), suggesting a shift on these populations in response to vaping treatment. Together, these findings define transcriptional changes on the lung architecture in cell type detection and spatial distribution in response to chronic vaping exposure.

4.3.7 Transcriptional response to xenobiotic stimulus, endothelial apoptosis, and lipid catabolism in lung parenchyma

Transcriptional differences across treatments on the parenchyma tissue were revealed by differential expression analysis, with 364 differentially expressed genes (DEGs) identified on NV spots and 51 DEGs on V parenchyma tissue (Fig 4.7A). DEGs derived from differential expression analysis were used as input for gene ontology (GO) analysis. GO term analysis by biological processes revealed an enrichment of various ontologies associated with metabolic processes and cellular apoptosis in the V samples (Fig 4.7B). Gene targets belonging to GO term (GO: 0071466), cellular response to xenobiotic stimulus, showed consistently increased expression in V samples (Cyp2a5, Gsto1, Cyp2f2, Fmo2, Gsta3, and Cyp2b10; Fig 7D). Parenchyma of V samples showed higher spot number expressing Gsto1 and Cyp2f2 with increase distributions throughout the tissue (Fig 4.7C and D). Transcripts for processes of xenobiotic response and endothelial apoptosis were significantly increased in vaped compared to non-vaped samples (Fig 4.7E). Cidea, Acadvl, Hsd11b1, and Acer2 targets belong to the lipid catabolic process GO term (GO: 0016042) were up-regulated in the parenchyma of V samples. Consistent with exposure of vape fluid, Cidea, a

gene associated to lipolysis, was overexpressed in vaped samples (Fig 4.7F). Additional GO terms with up-regulated targets upon vaping exposure included: drug catabolic process (GO: 0042737; Chil3, Cyp4b1, Hbb-bt, and Prdx6), glycerolipid metabolic process (GO: 0046486; Gpd1, Thrsp, Agpat2, and Apoc1), and hydrogen peroxide metabolic process (GO: 0042743; Cyp1a1, Hbb-bt, and Prdx6) (Data not shown). Collectively, these results demonstrate parenchyma exhibit transcriptional changes associated activating processes of endothelial apoptosis and lipid catabolism in respond to vaping xenobiotic stimulus.

4.3.8 Upper airway up-regulates transcriptome markers representing mitochondrial alterations during apoptosis and response to oxidative stress after vaping exposure

Differential expression analysis of the upper airway revealed 96 DEGs in the NV group and substantial up-regulation in the V group accounting for 1,385 DEGs (Fig 4.8A). GO analysis demonstrated enrichment of muscle contraction targets and processes in the NV group, with more metabolic GO terms in the vaped samples (Data not shown). Examination of biological processes revealed an enrichment of various ontologies associated with cellular stress on the vaped samples (Fig 4.8B). Biological significance of each GO term was assessed by comparing the gene count per GO term in addition to the gene ratio, verifying the DEG enrichment on the NV group (Fig 4.8C). Expression patterns of genes associated to the response to oxidative stress GO term (GO: 0006979) were consistently upregulated in the upper airway of vaped samples (Fig 4.3D). GO terms associated to mitochondrial homeostasis, membrane organization, fusion, and fission and gene expression were pronouncedly higher in gene ratio and gene count per GO term in the V samples (Fig 4.8E and F). Consistent with the GO analysis, average expression of targets belonging to the apoptotic mitochondrial changes were higher in the upper airway of vaped samples (Fig 4.8G). Similar to results observed in the lung parenchyma, gene ratios and counts of GO terms

associated to lipid metabolism were up in the V group, with up-regulated expression of genes in GO term (GO: 0016042) (Data not shown). Cross-referencing the DEGs from NV and V groups revealed an intersect of 80 DEGs characteristic of NV samples regardless of spatial distribution and 36 DEGs up-regulated in the V group (Data not shown). Together, these results demonstrate up-regulation of lipid catabolism and activation of apoptotic mitochondrial alterations and response to oxidative stress are the main transcriptional responses in the upper airway after vaping exposure.

4.3.9 Pulmonary dysfunction and right ventricular remodeling in vaped mice

VAPI as evidenced by multiple independent criteria and analyses (Figs 4.1–4.8) demonstrates severe damage to lung tissue. The clinical syndrome of severe VAPI has been associated with cardiac dysfunction [186,216,234] prompting assessment of myocardial structure and function in vaped mice after the 9-wk termination point of exposure. Short axis echocardiography was performed on all mice before euthanasia (Fig 4.9A) and multiple parameters of cardiac structure and function were calculated. Significant worsening ($P < 0.001$) of ejection fraction (EF; 62.41 ± 1.71 versus 74.91 ± 4.35), fractional shortening (FS; 32.67 ± 1.44 versus 42.45 ± 3.02), left ventricular interior diameter at systole (LVIDs; 2.129 ± 0.15 versus 1.794 ± 0.2), and left ventricular volume at systole (LV Vol S; 15.14 ± 2.25 versus 9.764 ± 3.67) was evident comparing hearts from vaped mice to non-vaped controls, respectively (Fig 4.9B–E). Interestingly, these same four indices of EF, FS, LVIDs, and LV Vol S also exhibit a lesser but significant gender difference ($P < 0.05$) subjects with consistently worse values for hearts of male versus female vaped mice (Fig 4.9B–E). All remaining calculated parameters of cardiac structure and function from echocardiographic measurements consisting of left ventricular mass, left ventricular volume at diastole, left ventricular interior diameter at diastole, intraventricular septum at diastole,

intraventricular septum at systole, left ventricular posterior wall at diastole, and left ventricular posterior wall at systole were not significantly different (Table 4.2). Pulmonary circuit failure associated with VAPI cannot be readily assessed by echocardiography in mice, so coronal sections of hearts were evaluated to determine right ventricular structural abnormalities. Right ventricular chamber enlargement and wall thinning is consistently evident in hearts of vaped mice compared to non-vaped controls (Fig 4.9F and G). Furthermore, histologic quantitation of cardiomyocyte cross-sectional length reveals significant elongation of cells in the right ventricular wall of vaped mice compared with non-vaped controls ($P < 0.001$ to 0.05; Fig 4.9H and Table 4.3). Pathological damage associated with right ventricular remodeling is also observed with increased collagen deposition at perivascular regions near the atrioventricular junction in hearts of vaped mice compared with non-vaped controls (Fig 4.9I and J). This preponderance of evidence indicating cardiac structural and functional deterioration pursuant to vaping is consistent with expectations of pulmonary failure in severe VAPI [186,216,234].

4.4 Discussion

VAPI presents several novel and unprecedented challenges for researchers, clinicians, and society including (1) the diverse array of device delivery systems for vape aerosols including "do-it-yourself" modifications, (2) an incalculable number of formulations for vape juices also including "do-it-yourself" recipes, (3) variability in vaping profiles and topography among users, (4) inability to readily obtain target tissue samples and track pathogenic changes in vapers, (5) inherent biological differences between users including (but not limited to) age, gender, health status, and genetic composition, (6) limitations of experimental modeling systems to recapitulate biological conditions of human vaping, (7) rapidly evolving vape industry products, (8) ephemeral

trends of the vape community, (9) inability to forecast long term effects of vaping due to lack of historical data (recency of development and utilization), and (10) balancing arguments of "harm reduction" for smokers versus creating a new generation of "never smoker" vapers. Assessing biological consequences of vaping in the human setting predominantly revolves around individuals experiencing symptoms of respiratory illness and relies upon non-invasive evaluation for diagnosis. Studying vaping pathogenesis requires understanding of alterations of both tissue structure/function as well as cellular/molecular biology that is not realistically possible in human subjects. As an alternative, rationally designed inhalation exposure models to provide biological insights are desperately needed. Paramount among the many questions to be addressed are: (1) what constituents of vape aerosol present substantial hazards for triggering pathological processes, and (2) what are predisposing factors for severe VAPI manifestation in some individuals? Identifying characteristics of "at risk" users will be critical to avoid potentially life changing pulmonary damage, and biological assessments using patient samples could offer diagnostic value for clinically relevant injury status evaluation. Whereas most vapers do not experience overt symptoms of VAPI, let alone exhibit pulmonary failure, a small subset of users succumb to this type of injury [181–186,234,235]. Such severe VAPI cases arise in users of commercially available vaping products, unlike the EVALI epidemic in 2019 traced back to black market "Dank Vapes" associated with ill-conceived mixing of Vitamin E acetate and THC into vape juice [214,215](48, 49). EVALI syndrome often presented as acute respiratory distress syndrome with fulminant inflammation in the respiratory tract [175–177]. In comparison, pathological processes culminating in severe VAPI are more obscure and slow to develop, in some cases occurring over months of frequent unrelenting vaping activity [181–186,234,235]. Thus, rather than model lung injury using xenobiotic agents that induce rapid and overwhelming inflammatory activity within hours such as

bleomycin or meconium [236,237], the conceptual framework for this study was to use widely available retail vaping technology and product combined with an extended exposure protocol consistent with topography of a high intensity vaper likely to develop VAPI leading to hospitalization.

Pathological outcomes of vaping vary dramatically in humans as well as laboratory models, but occurrence of severe VAPI in the clinical setting is a serious and growing concern in society [181–186,234,235]. The VAPI model developed in this report provides an experimental platform for this understudied syndrome, exhibiting a collective set of distinguishing characteristics without precedent in the literature. Foremost, phenotypic manifestations are reminiscent of clinical case reports of individuals hospitalized for severe VAPI including tissue damage, inflammatory responses, and cardiopulmonary failure. Importantly, pathogenesis was mediated by peach flavored vape juice with menthol cooling agent popularly used in the community delivered by the ubiquitous JUUL vape pen. Inhalation exposure of popular vape products using established vaping devices remains the best approximation of human activity to study biological effects upon the cardiopulmonary system. Vaping topography implemented in this report was deliberately designed based upon publications documenting human behavior and quantitative inhalation measurements (Fig 4.11; [205–207]). Puff frequency, duration, and flow rate were all set at values consistent with typified heavy vaping consumption for human subjects to the extent that our approach using an exposure chamber system can deliver similar parameters. Vaping topography is a critical factor in experimental design and varies widely between individual reports, often without detailed explanations for chosen parameters [201]. Justification and/or standardization of vaping topography remains an important unresolved issue in most vaping-related research studies. Judicious implementation of puff topography for inhalation exposure using real-world products common in

the vaping community produced a preclinical VAPI model over a 9-wk time course with clear evidence of pathological damage. Development of this inhalation exposure model enabled profiling of vaping biological effects on an unprecedented level using a combination of microscopic, biochemical, and molecular analyses offering fundamental insights into pathological responses in the cardiopulmonary system.

Pathological alterations consistent with VAPI in our murine model include multiple abnormalities in the respiratory tract. Widespread remodeling is evident from the upper airway passages to distal alveolar spaces deep within the lung parenchyma. Alveolar rarefaction, particularly evident in peripheral regions of the lung, is significant as demonstrated by mean linear intercept analysis (Fig 4.1). Deterioration of alveolar integrity is a hallmark of multiple respiratory distress syndromes including VAPI [238]. Despite substantial loss of alveolar integrity the mice in this study did not exhibit overt symptoms of respiratory distress throughout the time course of inhalation exposure and there was no occurrence of adverse events. Additional physiological analyses of respiratory functional parameters such as plethysmography and blood oxygenation level (pO2) could reveal subclinical manifestations in mice not apparent from behavioral observation. Thickening of bronchiolar passages together with localized accumulation of cellular infiltrate are histologic findings consistent with chronic irritation (Fig 4.1). Degeneration of airway structural integrity including features of epithelial dysmorphia as well as disruption of extracellular matrix were readily observed in histological evaluation (Fig 4.2). Elastin disorganization and increased collagen deposition presumably decrease airway compliance as has been described in other respiratory injury syndromes [239,240]. Elevation of mucin production and secretion represents a defensive mechanism within airways to facilitate clearance of inhaled foreign agents [221,222] and is clearly a feature of our VAPI model (Fig 4.3). Vape juice exposure provokes various biological

responses including increased secretory activity [222], but relative roles of the VG/PG vehicle versus minor component additives of flavorings and menthol cooling agents remains obscure and continues to be a focus of ongoing investigation [146,149,193,213,241]. Induction of inflammation and elevation of cytokine production (Fig 4.5) is commonly present in lung injury [144,146,242,243], but cellular infiltrates in our VAPI model are present in focal areas rather than uniformly distributed throughout tissues, most prominently proximal to airways or vessels indicative of remodeling. Chronic irritation serves as an inciting stimulus for oncogenic transformation [244,245], and indeed sporadic histologic signs of early stage tumorigenesis were rare events but present in our VAPI model (data not shown). Among lung epithelial proteins, ECAD plays particularly important roles in maintenance of cellular junctional integrity and has been linked to immunomodulatory activity [225]. Thus, the profound ECAD up-regulation in our VAPI model (Fig 4.4) may be multipurpose and it is tempting to speculate that ongoing suppression of airway inflammation may be involved. The potential relationship between VAPI, chronic airway inflammation, immunomodulation by ECAD, and oncogenic risk is an intriguing possibility to be explored in future studies.

Transcriptomic profiling is a powerful tool for identifying cellular reprogramming consequential to environmental stress. Transcriptional profiling of vape fluid exposure has primarily involved cell culture models examining acute changes after short-term exposure protocols [246–250]. Such studies have implicated vape juice for induction of genes associated with inflammation, metabolic/ biosynthetic processes, extracellular membrane, apoptosis, lipid metabolism, and hypoxia. None of these studies evaluated an inhalation exposure model of VAPI, which presents challenges for transcriptome profiling. Respiratory tract cellular composition is profoundly distinct in the upper airway compared with lung parenchyma, so spatial transcriptomics was used to facilitate regional identification of profiles. Predominant effects at the transcriptional

level in lung parenchyma include processes associated with endothelial apoptosis and lipid catabolism in respond to the xenobiotic stress of vape fluid exposure. In comparison, transcriptomic changes in the upper airway involve up-regulation of lipid catabolism and activation of apoptotic mitochondrial alterations and response to oxidative stress in the vaped samples relative to non-vaped controls. Select DEGs identified in bioinformatic analyses of particular interest include Gsto1 and Cyp2f2 because of their roles in inflammation [251], club cell differentiation, lung epithelial regeneration [252], and metabolism and toxicity of xenobiotic compounds [253]. Rgcc, Ager, and Angptl4 were among the up-regulated DEGs within the endothelial cell apoptotic process GO term (GO: 0072577). Ager, the gene encoding for RAGE is a key marker in pathophysiology of chronic obstructive pulmonary disease associated with cigarette smoking [254–256] (Fig 4.7E). These few examples demonstrate the diverse transcriptional effects characteristic of VAPI in our murine model. Broad roles of gene families mediating responses to xenobiotic agents, reactive oxygen species, lipid metabolism, and apoptotic signaling identified in this report provide a roadmap for future characterization in human VAPI samples. The differential expression analysis strategy of Model-based Analysis of Single-cell Transcriptomics (MAST) test [257] did not yield DEGs in our analysis. However, applicability of the MAST test to spatial transcriptomic data relative to the features and assumptions used for single cell data are unclear and possibly inappropriate. We suspect the multimodality and sparsity of spatial transcriptomic data from highly admixed tissues as the lung, which holds the transcriptome of numerous mixed cells within a 50-μm spot does not compare to single-cell transcriptome derived from a microfluidics approach. Nevertheless, DEG results are valid based upon expression levels per spot and spots count of targets of interest that were robust and consistent with Wilcoxon test results (Fig 4.7D, 4.8D and G). Candidate genes could be valuable for screening patient

samples to serve as diagnostics for assessment of VAPI severity in clinical setting, perhaps in subclinical evaluation of patient risk for VAPI. The extraordinary sensitivity and wealth of information derived from spatial transcriptomics allowed for an unprecedented view of cellular reprogramming in response to vape fluid inhalation exposure with the resulting datasets and their bioinformatic analyses forming the roadmap for future investigation.

Severe VAPI involves pulmonary failure including cardiac structural remodeling and functional decline [186,216,234]. Echocardiographic assessment provided initial indications of myocardial involvement in VAPI based upon significant decreases in EF and FS as well as increases in LVIDs and LV Vol S (Fig 4.9). Left ventricular functional and structural alterations are consistent with modest systemic hemodynamic decline rather than heart failure, as would be expected for VAPI with primary impact upon pulmonary circulation. Because assessment of right ventricular structure is not feasible by echocardiography in mice, evaluations were performed by histological analyses of coronal sections as well as measurement of cardiomyocyte length. Pathologic alterations of right ventricular structure include chamber enlargement and wall thinning as well as increased perivascular collagen deposition (Fig 4.9J), all indicative of increased hemodynamic stress in the pulmonary circuit. Increased collagen deposition surrounding the vessel above the right ventricle (Fig 4.9J) is consistent with increased perivascular collagen in lung sections (Fig 4.2). Right side failure is likely due to persistent pulmonary hypertension, but measurement of murine right ventricular hemodynamics is not practicable. Implications of pulmonary failure including impaired pO2 as well as compromised exercise capacity resulting from VAPI are the subject of ongoing studies. Increased cardiomyocyte length in the right ventricular free wall of mice suffering from VAPI compared with non-vaped controls is consistent with chamber dilation and wall thinning [258,259]. Collectively, cardiac remodeling is consistent with

expectations for severe VAPI-pathogenesis with one unanticipated distinction: the consistent gender-associated difference in severity. Female cardioprotection from pathological challenge is mediated by estrogenic activity involving AKT/Pim-1 axis downstream signaling [260–263]. Ramifications of gender-based differences in cardioprotection in relation to risk of pulmonary involvement will be an interesting biological phenomenon to correlate with clinical observations as VAPI hospitalizations accrue in the future.

No model can completely capture the complexities of human vaping exposure, but our murine model of inhalation exposure using popular vaping products and puff protocols based upon studies of human experience brings a new platform that can be modified as desired for rational experimental design (Fig 4.10A–D). Moreover, findings in this report provide broad-based yet integrated depiction of VAPI at the tissue, cellular, and molecular level serving as a reference point for future research. There is a desperate need for rigorous, unbiased, and independent research studies assessing biological responses to vape aerosol with inhalation exposure experimental models. Society is perched on the precipice of a new era for ENDS devices and vaporizers. Big Tobacco companies continue to find innovative ways to market tobacco related devices and products. Explosive growth of vaping over the past decade demonstrates consumer willingness to adopt new technologies for inhalation exposure in the absence of rigorous scientific research on potential health risks. Heated Tobacco Products represent the next generation of devices from Big Tobacco companies being touted for “harm reduction” compared to combustible cigarette smoking. Identical arguments of decreased health risks continue to be made for ENDS devices, and yet the evidence of pathological processes consequential to vaping is accumulating from past and ongoing research as well as clinical findings. Admittedly, there will always be a spectrum of VAPI from subclinical to mild to severe. However, no one can predict prevalence or clinical

presentation of VAPI in the years ahead with increasing years of exposure and advancing age of the user population. Only the passage of time will provide the information needed to assess the long term consequences of VAPI and recovery potential for human vapers, but these are certainly areas worthy of further investigation [109]. Findings in this report are deliberately intended to reflect severe VAPI that represents a minority of vaping-associated respiratory illness. Modeling severe VAPI consistent with clinical reports [181–186,234,235] provides insight regarding risk factors, biological responses, and cardiopulmonary susceptibility in a dynamic marketplace attracting a diverse user base that will continue to expand for the foreseeable future. Whether vaping technology or avant-garde heated tobacco products represent a lower risk for cardiopulmonary complications, respiratory illness, and cardiovascular diseases remains to be seen.

4.5 Materials and Methods

4.5.1 Mouse vaping inhalation protocol

4-wk-old male and female C57BL/6J mice were purchased from (Cat. no. 00064; Jackson Laboratory) and housed four mice per static cage. Ambient temperature was 70–72°F, on a 12-h light–dark cycle with automatic light control. Mice were supplied with Rodent Maintenance Diet (Teklad Global 14% Protein) and water ad libitum. During the adult phase of mouse life, 2.6 d are approximately equivalent to one human year. Vaping of mice started at ~8 wk (56 d) in a time course of 8–9 wk (age at conclusion equals 112–119 d). This represents the equivalent of human vaping from 16 to 37.5–40.2 yr of age according to Dutta and Sengupta [264] or the equivalent of 18–25 yr of age according to Flurkey [265]. 6-to 8-wk-old mice were exposed to Peach Ice 70VG/30PG (ORGNX) flavored vape juice delivered as e-vapor from JUUL pens in whole body exposure chambers (inExpose; SCIREQ). Vaping chamber setup is represented schematically in Fig 4.11. Mice were exposed to 3 s puffs every 20 s at 1.8 liters/minute, intake rate. Exhaust pumps

for fresh air flow rate was 2.5 and 1.5 liters/minute for the 4-h duration of the vaping profile (Fig 4.11) based upon human vaping topography recommended by Farsalinos et al. concluding "4-s puffs with 20–30 s interpuff interval should be used when assessing electronic cigarette effects in laboratory experiments, provided that the equipment used does not get overheated." [207] In addition, puff duration parameters and frequency are within the reported range of human vaping topography from real time characterization of electronic cigarette use in the 1 Million Puffs Study [206]. Animals were exposed for 4 h/day, 5 d/week for 9 wk (Fig 4.11).

4.5.2 Histological staining

Lungs of e-cigarette-exposed and control mice were harvested by inflation with formalin. Right lung lobes were sutured off at the right primary bronchus and frozen back in liquid nitrogen immediately after dissection, whereas the left lobe was manually inflated over the course of 15 min with ~1.5 ml of formalin until visual confirmation of sufficient inflation. The left lobe was then dissected and submerged in formalin for 24 h followed by tissue processing, paraffin embedding, and sectioning. The lungs were compressed to attain the primary bronchial tree in the same plane of view as parenchyma. Sections were stained with Harris Hematoxylin and Eosin-Phloxine (H&E) in addition to Movat's Pentachrome reagents to visualize morphometric and structural changes. Lung sections were stained after the modified Russell-Movat pentachrome stain protocol to visualize changes in collagen, elastic fibers, and mucin deposition. Pentachrome staining is interpreted as elastic fibers (black to blue/black), nuclei (blue/black), collagen (yellow to red), reticular fibers (yellow), mucin (bright blue), fibrin (bright red), and muscle (red). Trichrome Stain (Masson) Kit (Cat. no. HT15; Sigma-Aldrich) was used to visualize collagen

deposition in hearts and lungs according to the manufacturer's protocol. Images were acquired using a Leica DMIL6000 microscope running XY stage tile scanning and subsequently stitched using ImageJ software. PAS stain: Slides were deparaffinized and rehydrated after generic procedures. PAS stain was performed following the kit protocol specifications (1.01646.0001; Sigma-Aldrich). Hematoxylin solution modified according to Gill III was substituted, as recommended by the protocol, for hematoxylin solution modified according to Gill II (GHS216; Sigma-Aldrich). Finally, slides were mounted with toluene solution (Lot#103929; Thermo Fisher Scientific). Images were acquired using a Leica DMIL6000 microscope. All images were taken in the upper airway as close as possible to the branch point of the primary and secondary bronchi.

4.5.3 Quantitative analysis of lung morphometry by mean linear intercept and bronchial wall thickness

4.5.3.1 Mean linear intercept quantitation

H&E–stained sections of e-cigarette exposed and control mice were analyzed for changes to the mean free distance between gas exchange surfaces, denoted as mean linear intercept (Lm; N = 10 for each group). 10 randomly selected regions of lung parenchyma without bronchioles or vessels from each mouse were imaged and analyzed using the semi-automated method developed by Crowley et al [266]. 10 test lines were superimposed over the images and chords between alveolar walls were measured. An average of 2,000 chords per mouse were obtained. Lm was calculated by multiplying the lengths of the chords by the number of chords and dividing the product by the sum of all the intercepts.

4.5.3.2 Bronchial wall thickness

Lung sections of e-cigarette exposed and control mice stained with H&E were analyzed for changes to the thickness of the bronchial walls. Images of the bronchioles in a cross-sectional plane of view were taken from each mouse and measured using ImageJ software. An average of six independent measurements per mouse were taken. The total area of the bronchial was measured

by tracing the outside of the basement layer of the epithelium and the area of the lumen was measured by tracing the inner border of the epithelium. Wall area percentage was calculated by dividing the difference of the total area and the lumen area by the total area.

4.5.4 Immunohistochemistry and confocal microscopy

Tissue samples were formalin fixed and paraffin embedded as previously described (see "Histological staining") [267]. Paraffin sections (5 μm) were deparaffinized, subjected to antigen retrieval in 10 mM citrate, pH 6.0, and quenched for endogenous autofluorescent activity in 3% sodium borohydride (452882-250; Sigma-Aldrich) in TN buffer (150 mM NaCl and 100 mM Tris, pH 7.6) for 30 min. Blocking was performed for 30 min at room temperature with 10% Horse Serum in 1xTN. Tissues were immunolabeled with primary antibodies as listed in Table 4.1 overnight at 4°C. Fluorescently conjugated secondary antibodies were diluted 1:200 (Donkey antigoat 488 Cat. no. A11055; Life Tech, Donkey anti-rabbit 555 Cat. no. A32794; Invitrogen, Donkey anti-rat 555 Cat. no. 712-166-153; Jackson Labs, Donkey anti-chicken 555 Cat. no. 703-165-155; Jackson Labs, Donkey anti-rabbit 647 Cat. no. A31573; Invitrogen, Donkey antichicken 647 Cat. no. 703-505-155; Jackson Labs). DAPI (Cat. no. 62248; Thermo Fisher Scientific) was applied in the final wash step at 0.1 μg/ml to label nuclei. Images were acquired using a Leica SP8 confocal microscope and processed with Leica and Photoshop software. Stains were performed on at least three different samples per exposure group, and one technical replicate. Tissue was imaged from trachea, conducting airways, and lung parenchyma.

4.5.5 Muc5ac immunostain

Frozen sections prepared identical to those used for spatial transcriptomics (see below) were used to visualize Muc5ac. Slides stored at −80°C were warmed to room temperature and washed twice in PBS (0.37 M NaCl, 27 mM KCl, 100 mM Na2HPO4, and 18 mM KH2PO4), then

fixed in −20°C methanol for 30 min. Two more washes in PBS were performed, and then the tissue was blocked using 10% Horse Serum for 30 min. Next, two washes in PBS were followed by immunolabeling with Muc5ac (Cat. no. 1364248; U.S. Biotech) and ECAD (Cat. no. AF748; R&D Systems) overnight at 4°C. Two more washes in PBS were performed the following day, and fluorescently conjugated secondary antibodies were used to detect primary antibodies (Donkey anti-Rabbit 555 703-165-155; Jackson Labs, Donkey anti-Goat A11055; Life Tech) for 1 h and 30 min at room temperature. After two washes in PBS, DAPI (Cat. no. 62248; Thermo Fisher Scientific) was applied in the final wash step at 0.1 μg/ml to label nuclei for 15 min in PBS, and slides were coverslipped and mounted in Vectashield (Cat. no. H-1000; Vector Labs). Images were acquired using Leica SP8 confocal microscope and images were processed with Leica software. Tissue was imaged in most distal airways where mucin secretion is uncommon.

4.5.6 Immunoblotting

Lungs from vaped animals and air-exposed controls were collected and stored at −80°C for future analysis. Frozen lung tissues were homogenized in lysis buffer containing protease and phosphatase inhibitor cocktails (P8340, P5726, and P2850; Sigma-Aldrich). Bradford assay was performed to analyze and normalize protein concentrations and lysates were prepared by addition of NuPAGE LDS Sample Buffer (NP0007; Thermo Fisher Scientific) and 100 μM dithiothreitol (161-0611; Bio-Rad). Samples were sonicated and boiled for 5 min at 95°C and stored at −80°C. Proteins were separated on a 4–12% NuPAGE Bis-Tris gel (NP0321BOX; Thermo Fisher Scientific) and transferred onto a polyvinylidene fluoride membrane. Nonspecific binding sites were blocked using Odyssey blocking buffer (927-60001; LICOR) and proteins were labeled with primary antibodies in 0.2% Tween in Odyssey blocking buffer overnight. After multiple washes, blots were incubated with secondary antibodies in 0.2% Tween 20 in Odyssey blocking buffer for

1 h 30 mins at room temperature and scanned using the LICOR Odyssey CLx scanner. Quantification was performed using ImageJ software. Antibodies and their dilutions are listed in Table 4.4.

4.5.7 Spatial transcriptomic analyses

4.5.7.1 Sample preparation

Lungs were inflated through the trachea with a 1:1 PBS/OCT mix (1× PBS, Cat. no. 21-040-CV; Corning; TissueTek O.C.T. Compound, Cat. no. 25608-930; VWR) with RNAse inhibitor at 0.2 U/µl (Cat. no. 3335399001; Millipore Sigma). Tissues were embedded in OCT and flash frozen using an isopentane and liquid nitrogen bath. Tissue sections of 10 µm were obtained on a CryoStar NX70 (Thermo Fisher Scientific) and processed immediately for spatial transcriptional analysis or stored for histological stains. Blocks and sections were maintained at −80°C for long-term storage.

4.5.7.2 Image collection and spatial transcriptomic library preparation

Freshly obtained cryosections were placed in Visium gene expression slides (Cat. no. 2000233; 10X Genomics) for processing. Tissue staining with hematoxylin and eosin and image collections were performed as recommended by the Visium protocol. Images were collected on a Leica DMI6000 B on a 5× objective at a 1.16 µm/pixel capture resolution (Data not shown). Spatial transcriptomic libraries were prepared using Visium Spatial Gene Expression Slide & Reagent Kit following the manufacturer's protocol (PN-1000184; 10X Genomics). Lung permeabilization time was optimized Visium Spatial Tissue Optimization Slide & Reagent Kit (PN-1000193; 10X Genomics). Samples were processed together to avoid introduction of technical batch effects. Library concentration and fragment size distribution of each library were tested with Bioanalyzer

(Agilent High Sensitivity DNA Kit, Cat. no. 5067-4626; average library size: 500–610 bp). The sequencing libraries were quantified by quantitative PCR (KAPA Biosystems Library Quantification Kit for Illumina platforms P/N KK4824) and Qubit 3.0 with dsDNA HS Assay Kit (Thermo Fisher Scientific). Sequencing libraries were submitted to the UCSD IGM Genomics Core for sequencing (NovaSeq 6000), aiming for >50K reads per spot.

4.5.7.3 Spot processing and quality control

Raw data were processed on the SpaceRanger pipeline (10X Genomics; version 1.2.2, Data not shown). Sequencing reads were aligned to the 10x mouse genome mm10-2020-A. Spots maintained comparable UMI and gene count detection throughout the tissue section (Data not shown). Counts per spot were normalized to account for variance within tissue anatomy, and transformed using Seurat R Package (v4.0.3) to account for technical artifacts and preserve biological variance [48,268]. Preparations derived from slide preparation yielded 4933 barcoded spots for analysis, from which 1,315 corresponded to Control (842 male, 473 female), and 3,618 corresponded to 0% vape group (1,565 male, 2,053 female). Final removal of unwanted sources of variation and batch effect corrections was performed using Seurat R Package (v4.0.3).

4.5.8 Bioinformatics

4.5.8.1 Dimensionality reduction and unsupervised clustering

The first 30 principal components (PCs) were used to perform dimensionality reduction. Approximately 1,000 spatially variable genes were selected based on their expression and dispersion using the “markvariogram” method [269]. PC analysis was performed on the scaled data as a dimensionality reduction approach. The first 30 PCs were selected for unsupervised clustering and nonlinear dimensional reduction (UMAP; Data not shown). PC selection was based using an heuristic approach ranking the percentage of the variance explained by each PC[270]. Clusters were

classified using the clustifyr package [271] using the Tabula muris data as reference set for classification [28] (data not shown), and spots mapped to the MCA database using scMCA package [272].

4.5.8.2 GO analysis

GO enrichment analysis for DEGs lists derived from parenchyma and upper airway spots was performed using the enrichGO and compareCluster functions of clusterProfiler (3.16.1) R package [51]. Bonferroni correction was use as a multiple hypothesis test method to control the number of false positives [273].

4.5.9 Echocardiography

Transthoracic echocardiography was performed on lightly anesthetized mice under isoflurane (1.0–2.0%; Abbot Laboratories) using a Vevo 2100 (VisualSonics). Hearts were imaged in the 2D parasternal short-axis (SAX) view, and M-mode echocardiography of the mid-ventricle was recorded at the level of papillary muscles to calculate FS. From the recorded M-mode images, the following parameters were measured: EF, left ventricular (LV), anterior wall thickness (AWT), LV posterior wall thickness (PWT), LV internal diameter (LVID), and LV volume in diastole (index: d) and systole (index: s).

4.5.10 Cardiac histology

After anesthetization of the mice by ketamine, hearts were arrested in diastole and perfused with formalin for 15 min at 80–100 mm Hg via retrograde cannulation of abdominal aorta. Retroperfused hearts were removed from the thoracic cavity and fixed overnight in formalin at room temperature. The hearts were processed for paraffin embedding and sectioned in the sagittal

orientation at 5 μmthickness at room temperature. The heart sections were stained with Harris hematoxylin and eosin Phloxine to visualize morphometric and structural changes. Images were obtained by a Leica DMIL6000 microscope using XY stage tile scan and manually stitched using ImageJ software.

4.5.11 Cardiomyocyte cross sectional area quantitation

Heart sections of all treatment groups were acquired and stained as previously described with the exception that heart samples were not treated with sodium borohydride. 24 images of each right ventricle were taken using a Leica SP8 confocal microscope at a 400× magnification. Quantification of the cross sectional area of right ventricularmyocytes was done in ImageJ software using a pixel/umratio of 3.5 for all images analyzed. Myocytes that contained two clear intercalated discs at each end with an associated nucleus were measured by drawing a line from one intercalated disc to the other, then measuring the length of the line. All measurements taken from each experimental group are listed in the table below. Data points were input into Prism5 software to compose a graph and run a one way ANOVA test using Kruskal–Wallis metrics, $P < 0.01$. Male Vape (n = 4, 133 measurements, SD: ±12.9 μm). Female Vape (n = 4, 116 measurements, SD: ±14.13). Male No Vape (n = 3, 83 measurements, SD: ±14.97). Female No Vape (n = 3, 72 measurements, SD: ±9.935).

4.5.12 Statistics

For mean linear intercept and bronchiole wall area percentage, unpaired t tests were performed between the vape and no vape groups with a 95% confidence interval and a two-tailed P-value of 0.0167 for 1D and 0.0098 for 1E I using GraphPad Prism Version 5.02. For echocardiography, 5–7mice per group ANOVA with Kruskal–Wallis significant differences test

with $P < 0.05$(*), $P < 0.01$(**), $P < 0.001$(***). For differential expression analysis, Wilcoxon rank sum test was performed with selection for a threshold of 0.05 for an adjusted P-value and a log (FC) > 0.25 was used to define statistically significant and DEGs.G0 term analysis was performed with P-value cutoff of 0.05 using Benjamini–Hochberg Procedure. For immunoblot analysis, two-tailed unpaired t test was used to compare two groups of vape and non-vape samples. Statistical analysis was performed using GraphPad Prism. A P-value of < 0.05 was considered statistically significant. For cardiomyocyte cross-sectional length, right ventricularmyocyteswere analyzed inmale and female, vaped and nonvaped samples. A one-way ANOVA using Kruskal–Wallis t test metrics was performed on the total number of measurements per group ($P < 0.01$). Male Vape (n = 4, 133 measurements, SD: ±12.9 μm). Female Vape (n = 4, 116 measurements, SD: ±14.13). Male No Vape (n = 3, 83 measurements, SD: ±14.97). Female No Vape (n = 3, 72measurements, SD: ±9.935).

4.5.13 Study approval

Animal protocols and experimental procedures were approved by the Institutional Animal Care and Use Committee at San Diego State University.

4.5.14 Data Availability

Spatial transcriptomic data generated in this study has been uploaded to the Gene Expression Omnibus database (GSE188805).

4.5.15 Supplementary Information

Supplementary Information is available at https://doi.org/10.26508/lsa.202101246.

4.6 Acknowledgements

This work was supported by NIH grants R01HL135661-02. Chapter 4, with slight modifications, is a reprint of the material as it appears in Life Science Alliance, Vol. 5, No. 2, 2021. Fundamentals of vaping-associated pulmonary injury leading to severe respiratory distress. Carolina Esquer, Oscar Echeagaray, Fareheh Firouzi, Clarissa Savko, Grant Shain, Pria Bose, Abigail Rieder, Sophie Rokaw, Andrea Witon-Paulo, Natalie Gude, Mark A Sussman. The dissertation author was the primary co-author and investigator on this manuscript.

The author extends his deepest appreciation to members of the Sussman Laboratory who provide invaluable assistance and expertise in developing vaping-related studies and information. This publication includes data generated at the UC San Diego IGM Genomics Center utilizing an Illumina NovaSeq 6000 that was purchased with funding from a National Institutes of Health SIG grant (#S10 OD026929).”

4.7 Figures

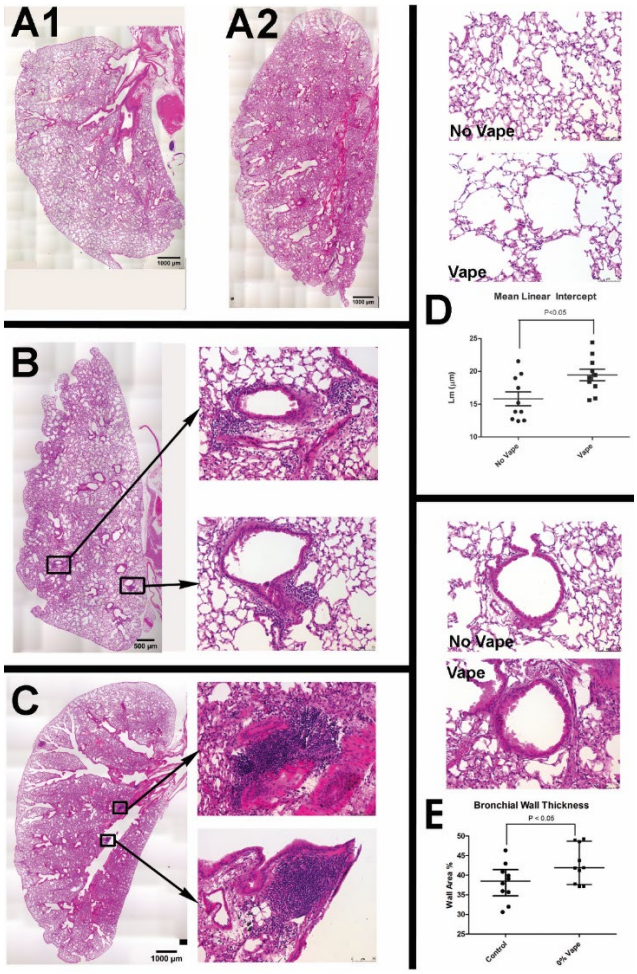

Figure 4.1 Structural and morphometric alterations to lung parenchyma and airways following vape exposure.

Representative H&E images of entire lung section demonstrating overview of changes following vape exposure in normal (**A1**) and vaped (**A2**) lung. Representative images of vape lungs showing cellular infiltrates proximal to airways (**B** and **C**). Overview of vape lung showing localization of cellular infiltrates surrounding bronchioles (**B**) with inset images at right showing boxed regions of cellular infiltrates surrounding bronchioles. Overview of vape lung showing localization of cellular infiltrates at branching of primary bronchiole (**C**) with inset images at right showing boxed regions of cellular infiltrates at branching of primary bronchiole. Lung parenchyma structure (**D**) in normal lung (No Vape) compared to vape lung shows alveolar rarefaction (Vape). Average free distance between alveolar walls measured by mean linear intercept (Lm) shows significantly increased open space in vaped relative to normal lung (**D, Mean Linear Intercept graph**; $p<0.05$). Each dot represents the average of all independent measurements from one mouse. The bars represent the median and interquartile range. Bronchiole airway cross-section comparison (**E**) between normal (No Vape) versus vaped (Vape) lung tissue in sections. Bronchiole wall thickness significantly increased in vape group (**E, Bronchiole Wall Thickness graph**; $p<0.01$) measured as percentage of the difference between total and lumen area over total area. Each dot represents the average of all independent measurements from one mouse. The bars represent the median and interquartile range. N=10 mice for each group.

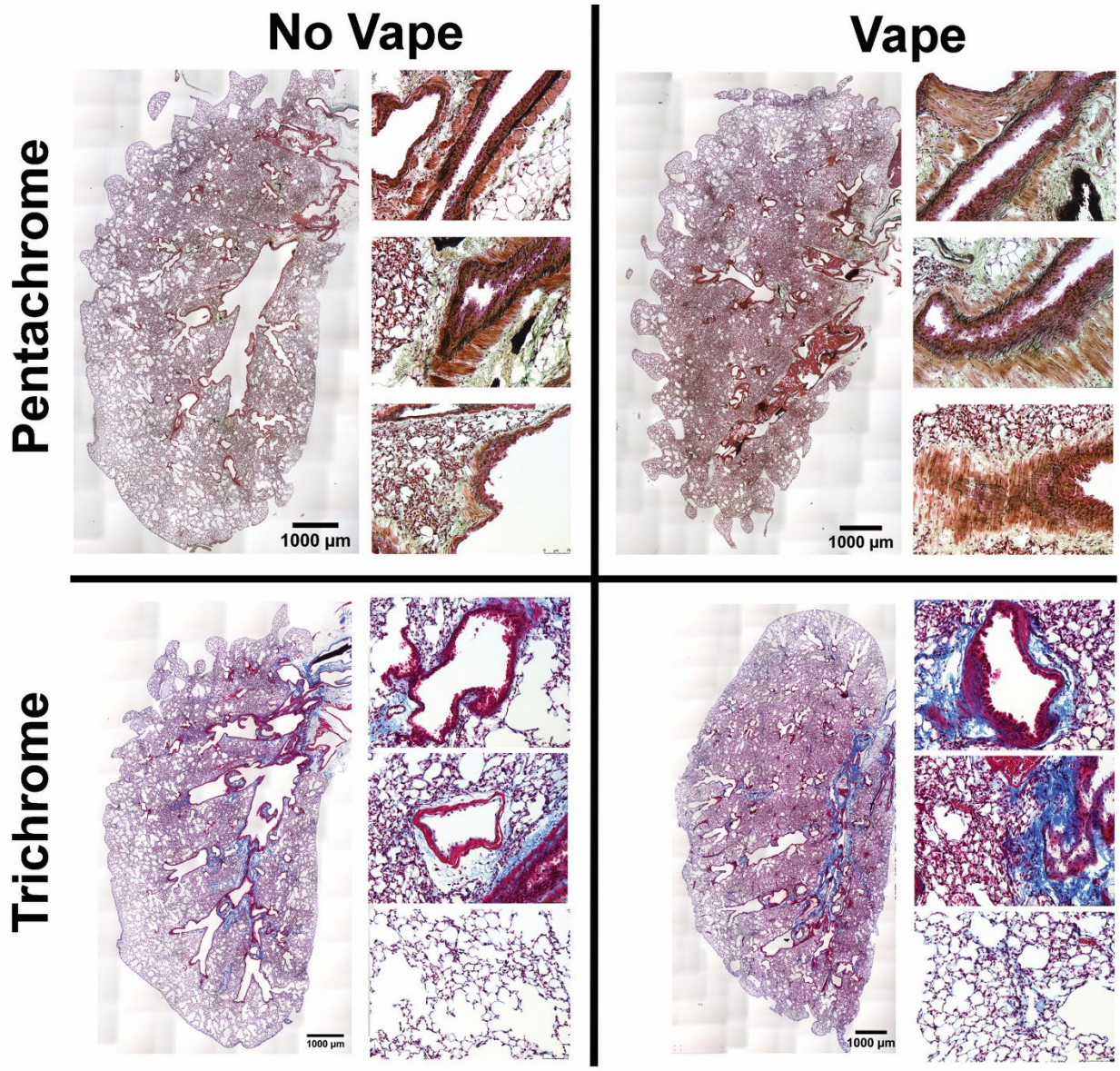

Figure 4.2 Pathologic disruption of structural organization in airway and lung tissue of vaped mice.

Overview of lung sections from No Vape (left) and Vape (right) stained with either Movat's Pentachrome (top row) or Masson's Trichrome (bottom row). Pentachrome stained magnified images at right of each overview show elastic fiber disorganization lining the airways in Vape samples (elastic fibers and nuclei (black); muscle (red); fibrin (bright red); collagen and reticular fibers (yellow); ground substance and mucin (blue). Trichrome stained magnified images at right of each overview show increased collagen deposition surrounding bronchioles (top), vasculature (middle), and parenchyma (bottom) in vape lungs (collagen (blue); muscle fibers (red); nuclei (black).

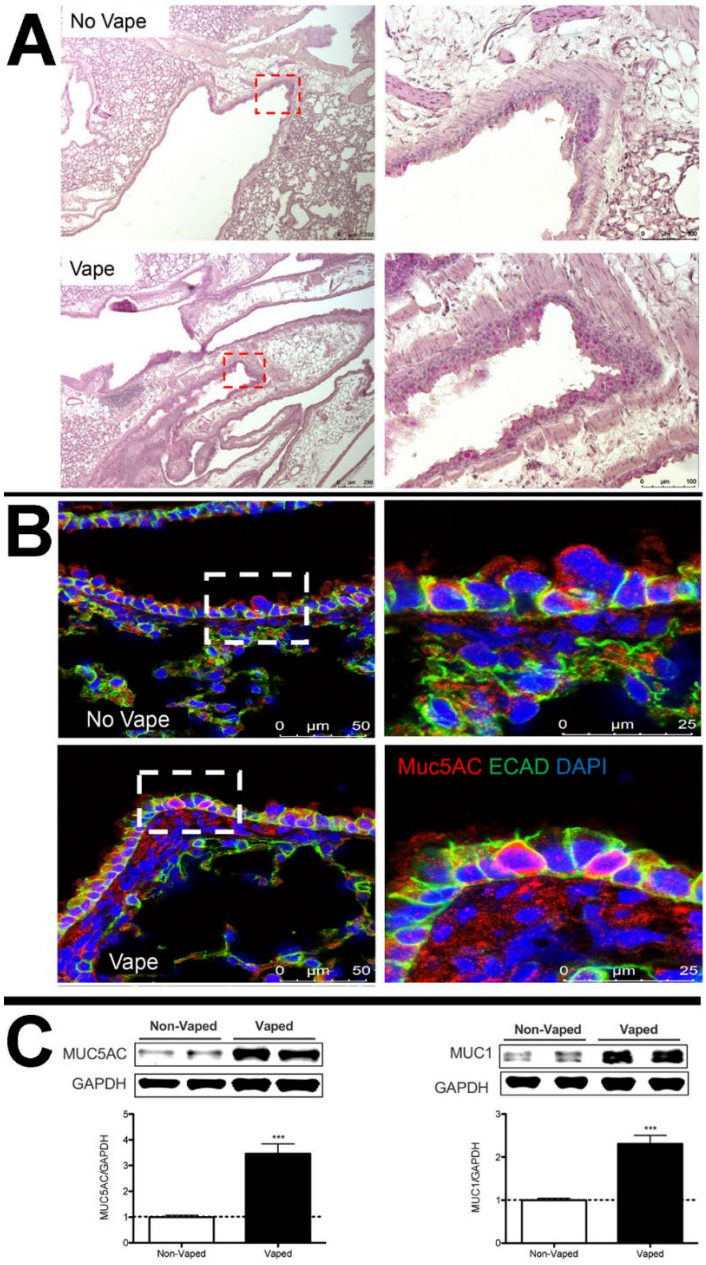

Figure 4.3 Mucin accumulation in bronchial airways of vaped mice.

(A) Periodic Acid Schiff (PAS) stain of representative No Vape or Vape lung tissue sections demonstrating increased mucopolysaccharides (deep red color) in vaped samples. Inset images boxed by red dotted lines are shown to the right of corresponding section. (B) Increased Mucin5AC in goblet cells of lower distal airway near the parenchyma by confocal immunomicroscopy. All images are representative of Mucin5AC (red), E-cadherin (cell adhesion molecule; green), and DAPI (nuclei; blue). (C) Mucin 5AC and Mucin 1 protein levels are significantly increased (***; $p<0.001$) in tissue samples prepared from lungs of vaped mice (Vaped) relative to normal lung samples (Non-Vaped). Corresponding quantitation of immunoblots is shown under each representative blot. GAPDH is used as loading control. Independent replicate blots of n=12 for MUC5AC and MUC1 using 4 non-vaped control mice and 17 vaped mice. Error bars represent SEM.

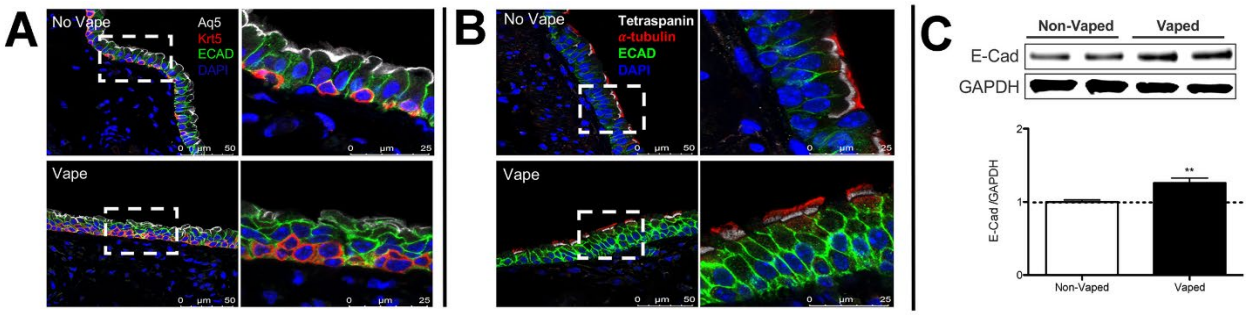

Figure 4.4 Pseudostratified columnar epithelium disruption in trachea of vaped mice.

Pseudostratified cell architecture in normal trachea epithelial layer (No Vape) is disorganized by vaping exposure (Vape). (**A**) Deterioration of Basal Cell (red; Krt5) distribution, diminished Aquaporin5 channel immunoreactivity (white; Aq5) in surface epithelium, and increased immunolabeling of E-Cadherin (green; E-Cad) in vaped sample relative to No Vape control. (**B**). Ciliated epithelium (red; α-tubulin) and cytoskeletal tetraspanin (white) marks apical epithelial boundary above disorganized cell layers in Vaped versus No Vape controls revealed by E-Cad (green) and nuclei (blue; DAPI). All images are representative and taken in superior trachea. (**C**) E-Cadherin (E-Cad) protein levels are significantly increased (**; $p<0.01$) in tissue samples prepared from lungs of vaped mice (Vaped) relative to normal lung samples (Non-Vaped). Corresponding quantitation of immunoblot is shown representative blot. GAPDH is used as loading control. Independent replicate blots of n=6 using 4 non-vaped control mice and 17 vaped mice. Error bars represent SEM.

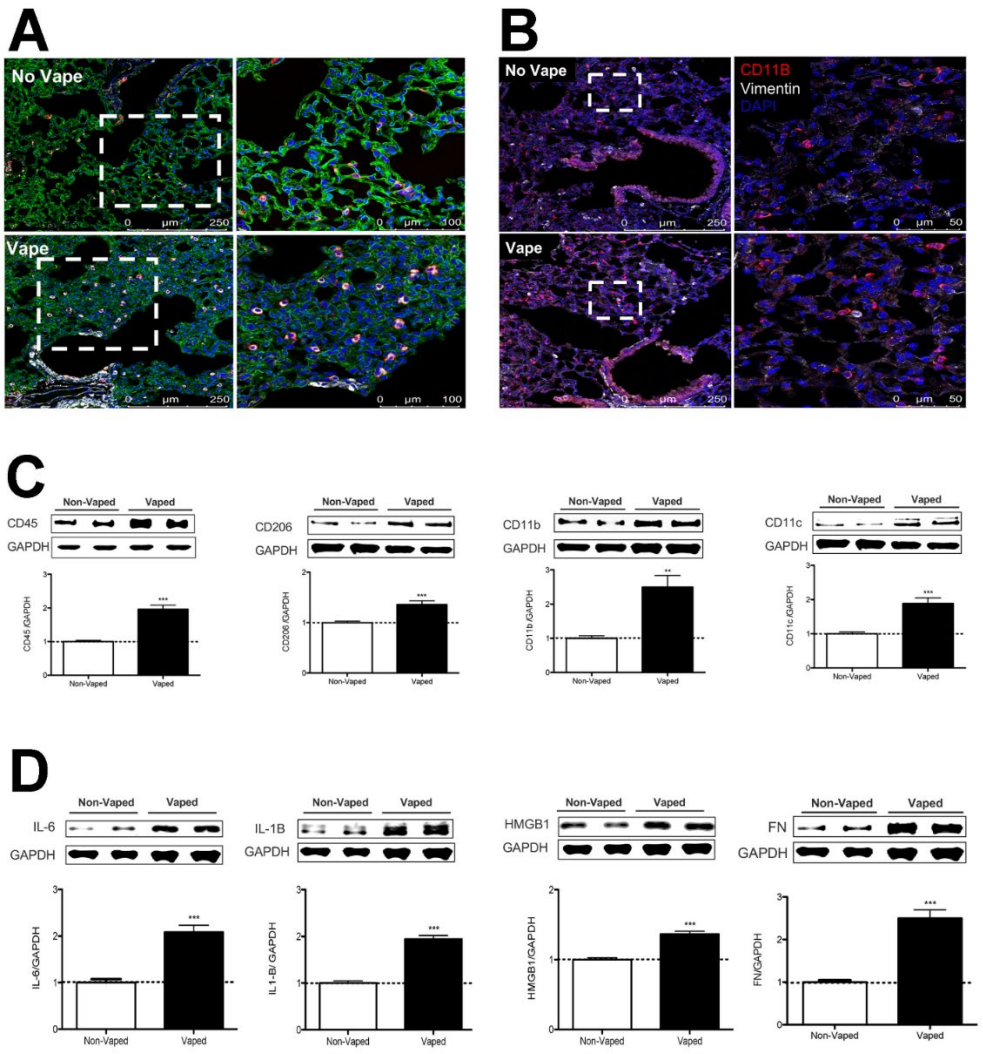

Figure 4.5 Inflammatory activity increased in vaped mice.

(**A**) Immune cellular infiltration increased in vaped (Vape) relative to normal (No Vape) lung tissue sections revealed by immunoreactivity for CD11c (innate immune cells; red), vimentin (intermediate filaments; white), and Receptor for Advanced Glycation End products (RAGE; alveolar type-1 cells; green) with nuclei label (blue; DAPI). (**B**) Comparable immunolabeled section to (A) without RAGE labeling with CD11b (red), vimentin (white), and DAPI for nuclei (blue). All images are taken in the distal alveolar region of the lung. Inset images boxed by white dotted lines are shown to the right of corresponding section. (**C**) Increased expression of immunophenotypic markers of cellular infiltrate in Vaped lung samples relative to Non-Vaped controls including CD45, CD206, CD11b, and CD11c. GAPDH is used as loading control. Corresponding quantitation of immunoblots is shown under each representative blot. n=8 independent immunoblots using n=4 non-vaped control mice and n=17 vaped mice. Error bars represent SEM. *** p< 0.001, ** p< 0.01. (**D**) Increased expression of immunomarkers of inflammation and matrix remodeling in Vaped lung samples relative to Non-Vaped controls including interleukin 6 (IL-6), interleukin 1B (IL-1B), high mobility group box protein 1 (HMGB1), and fibronectin (FN). GAPDH is used as loading control. Corresponding quantitation of immunoblots is shown under each representative blot. n=12 independent immunoblots using n=4 non-vaped control mice and n=17 vaped mice. Error bars represent SEM. *** p< 0.001.

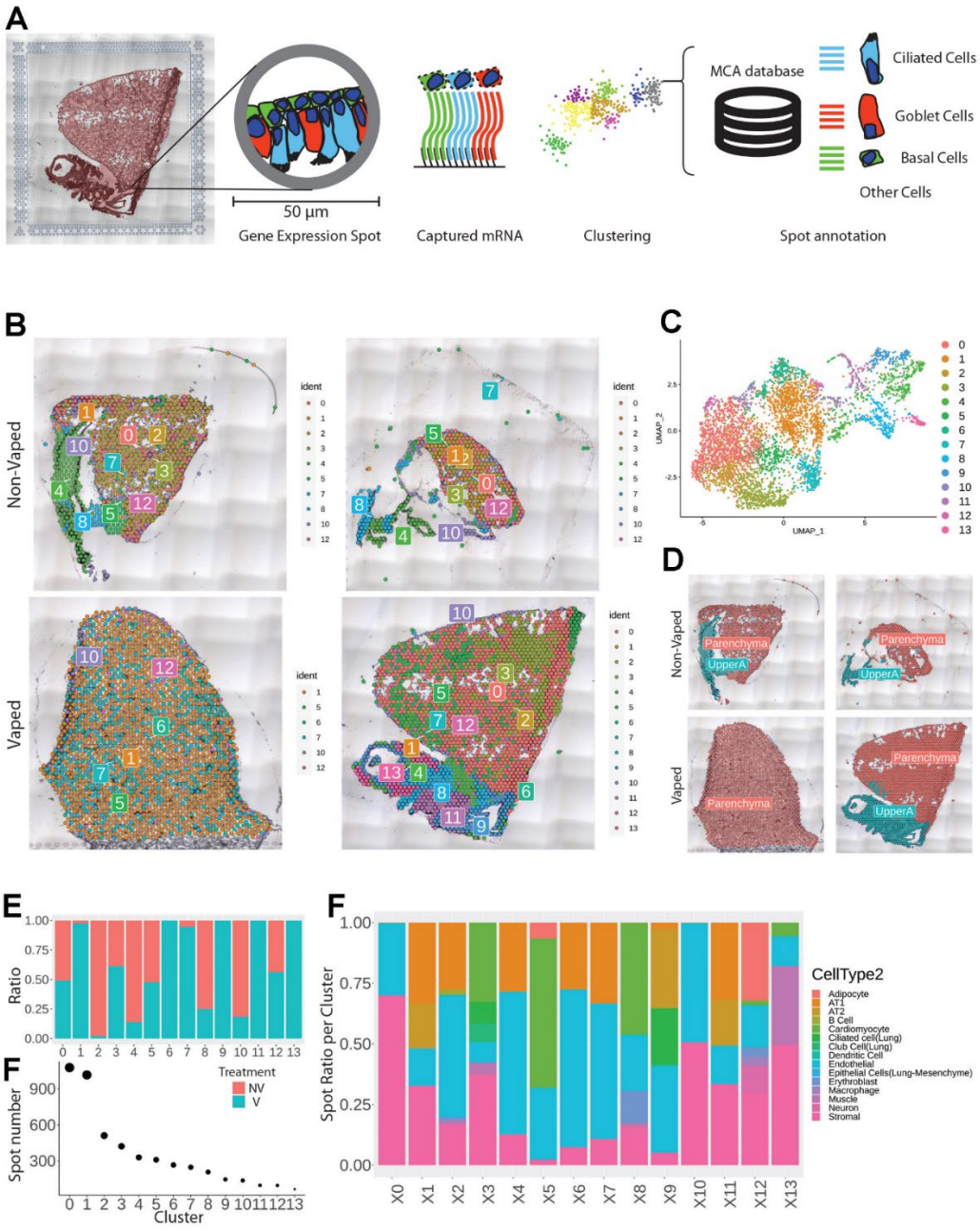

Figure 4.6 Vaping induces spatial transcriptional changes in pulmonary tissue.

(**A**) Schematic of experimental workflow representing capture of lung tissue within fiducial frame of gene expression slide, RNA library preparation and data analysis to spot annotation on the Mouse Cell Atlas (MCA) database. (**B**) Spatial representation of unsupervised clusters overlaid on Hematoxylin and Eosin (H&E) micrographs of Non-Vaped and Vaped samples. (**C**) UMAP projection color-coded according to unsupervised clustering of gene signatures. (**D**) Identification of parenchyma and upper airway clusters overlaid on H&E micrographs of Non-Vaped and Vaped samples. (**E**) Relative and absolute (**F**) spot contributions of Non-Vaped and Vaped derived samples to each cluster as shown in UMAP (Panel 6C and Supplemental Figure 2b). (**G**) Putative cell type contributions by cluster relative to MCA database (Condense plot).

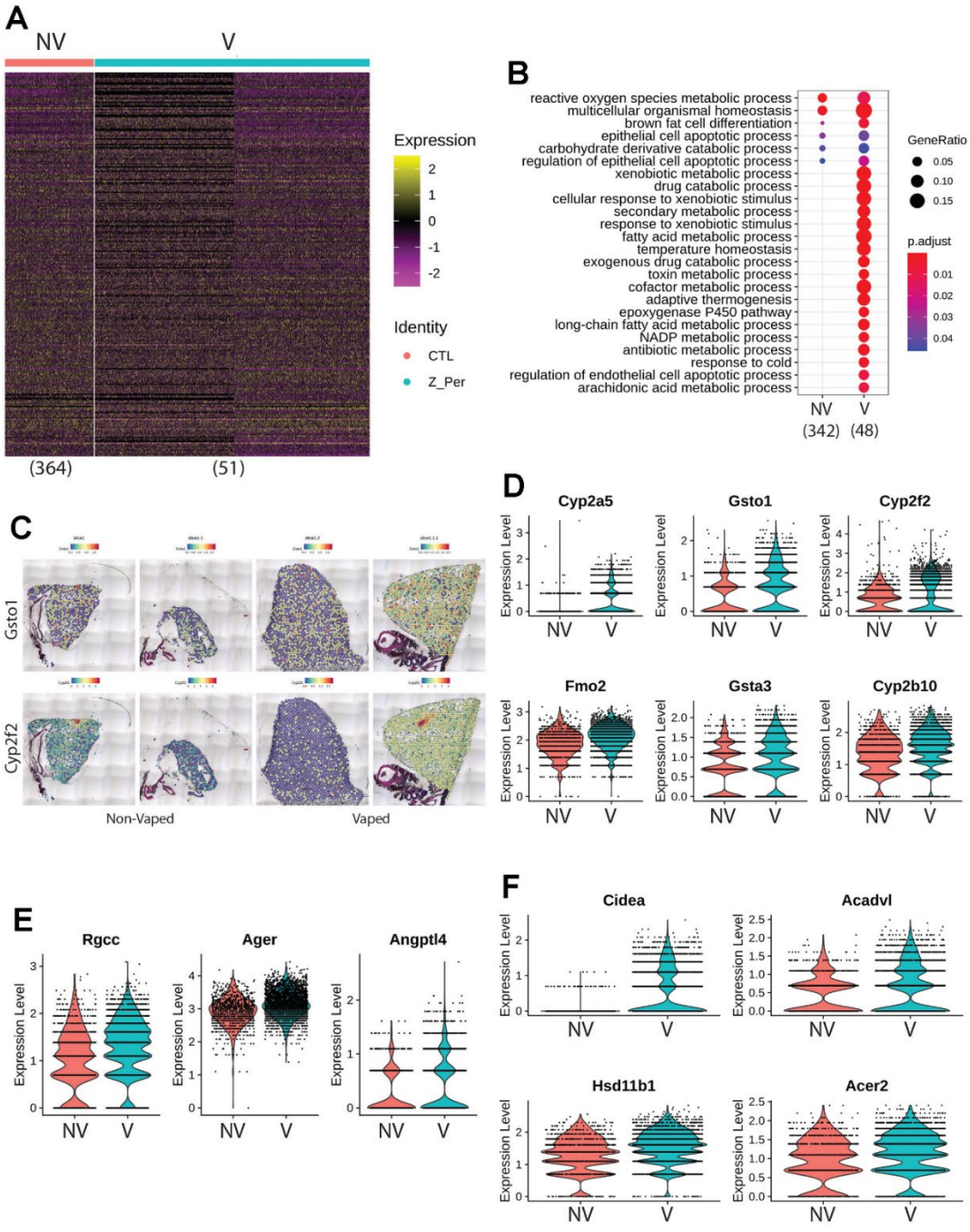

Figure 4.7 Chronic vaping prompts response to xenobiotic stimulus, endothelial apoptosis and lipid catabolism in lung parenchyma.

(**A**) Heatmap representing the differential expressed genes from Non-Vaped and Vaped samples in the parenchyma subset. (**B**) GO terms results from Gene Ontology analysis annotated by Biological Process. Circle diameter represents the gene ratio, while significance level is color-coded according to heatmap scale. (**C**) Spatial expression and distribution of Gsto1 and Cyp2f2 in Non-Vaped and Vaped samples. Violin plots indicating the single spot distribution and expression of gene targets of GO terms: (**D**) cellular response to xenobiotic stimulus, (**E**) endothelial cell apoptotic process and (**F**) lipid catabolic process.

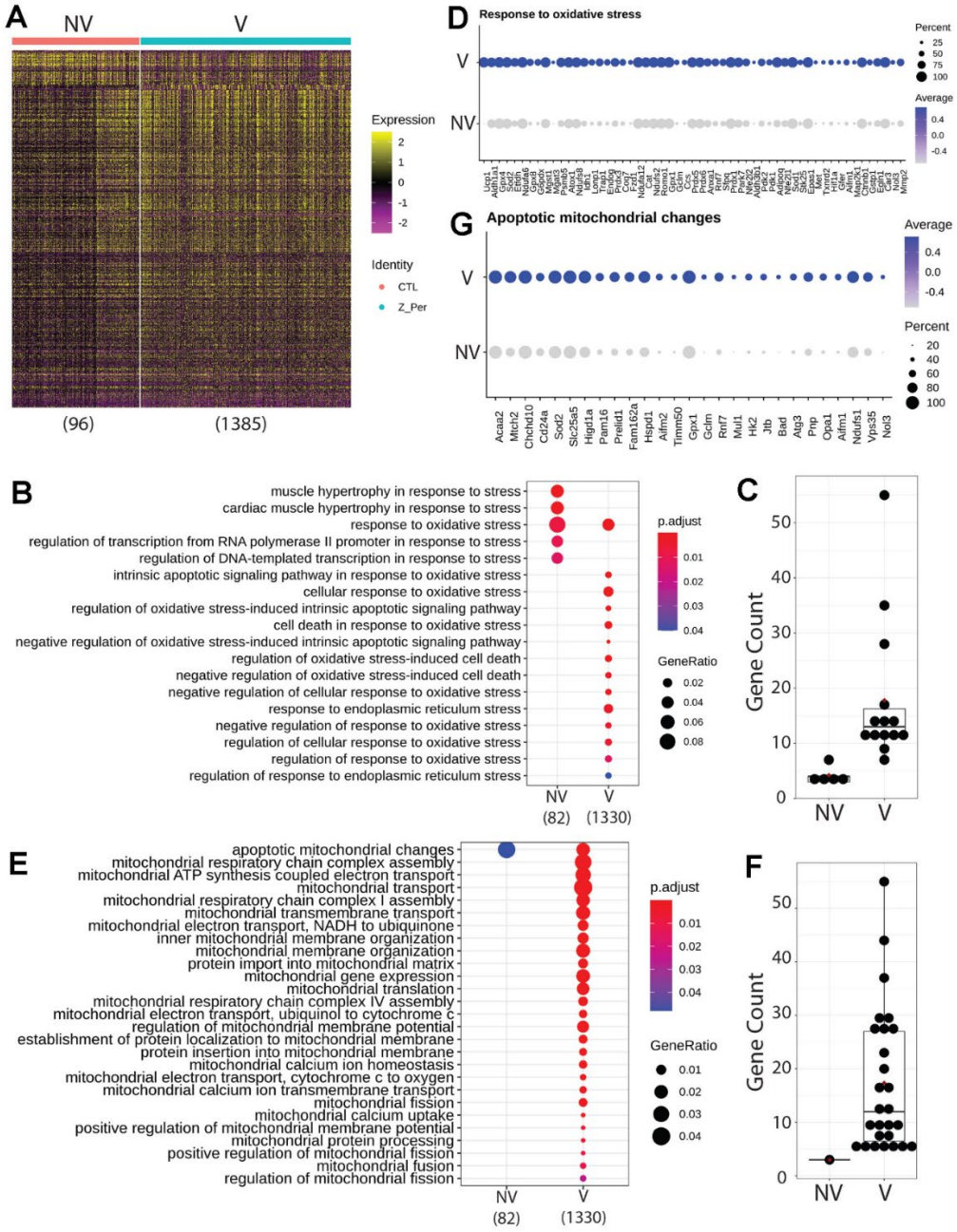

Figure 4.8 Upper airway upregulates targets linked to mitochondrial alterations during apoptosis and response to oxidative stress after vaping exposure.

(**A**) Heatmap representing the differential expressed genes from Non-Vaped and Vaped samples in the upper airway subset. GO terms results from Gene Ontology analysis annotated by Biological Process and grouped by (**B**) cellular stress and (**E**) mitochondrial ontologies on Non-Vaped and Vaped samples. Circle diameter represents the gene ratio, while significance level is color-coded according to heatmap scale. Gene counts per GO term grouped by (**C**) cellular stress and (**F**) mitochondrial ontologies on Non-Vaped and Vaped samples. Dotplot representing expression of marker of GO terms: (**D**) Response to oxidative stress and (**G**) Apoptotic mitochondrial changes. Circle diameter represents the percentage of spots expressing a particular gene, while normalized average expression is represented by color intensity.

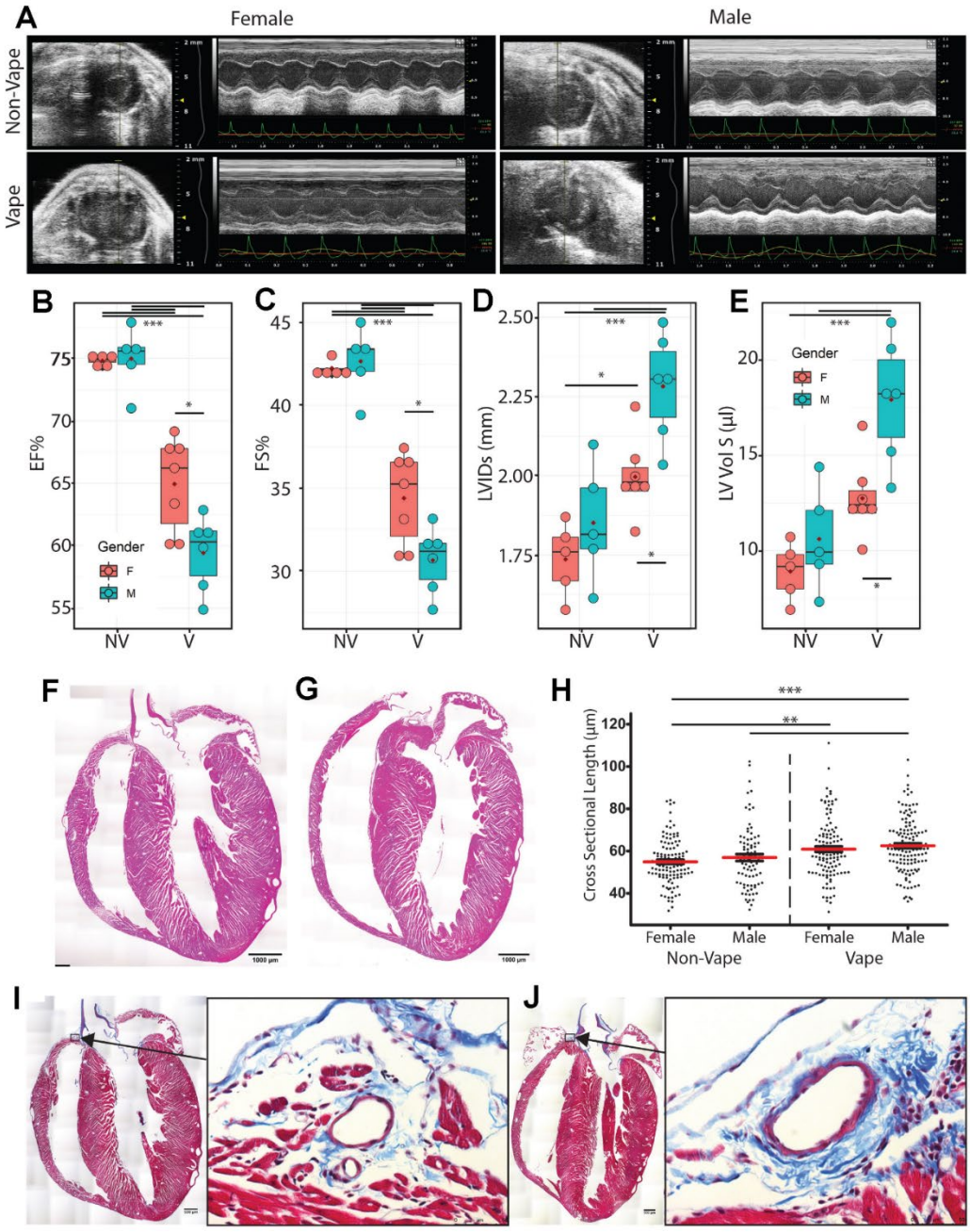

Figure 4.9 Pulmonary dysfunction and right ventricular remodeling in vaped mice.

(**A**) Representative 2D echocardiography images (M-mode) at study completion (week 9). Para-sternal short-axis view showing LV anterior wall and posterior wall movement. Echocardiogram data from non-vaped and vaped samples measuring (**B**) Ejection fraction, (**C**) Fractional shortening, (**D**) Left Ventricular Interior Diameter in systole and (**E**) Left Ventricular Volume in systole. Hematoxylin and Eosin (H&E) micrographs of (**F**) Non-Vaped and (**G**) Vaped hearts in coronal view. (**H**) Myocyte cross-sectional length in right ventricle. Masson's trichrome stain of (**I**) Non-Vaped and (**J**) Vaped samples hearts in sagittal view (Arrow: Collagen deposition. Arrowhead: cellular infiltrate). ANOVA with Kruskal-Wallis significant differences test. $p<0.05$(*), $p<0.01$(**), $p<0.001$(***).

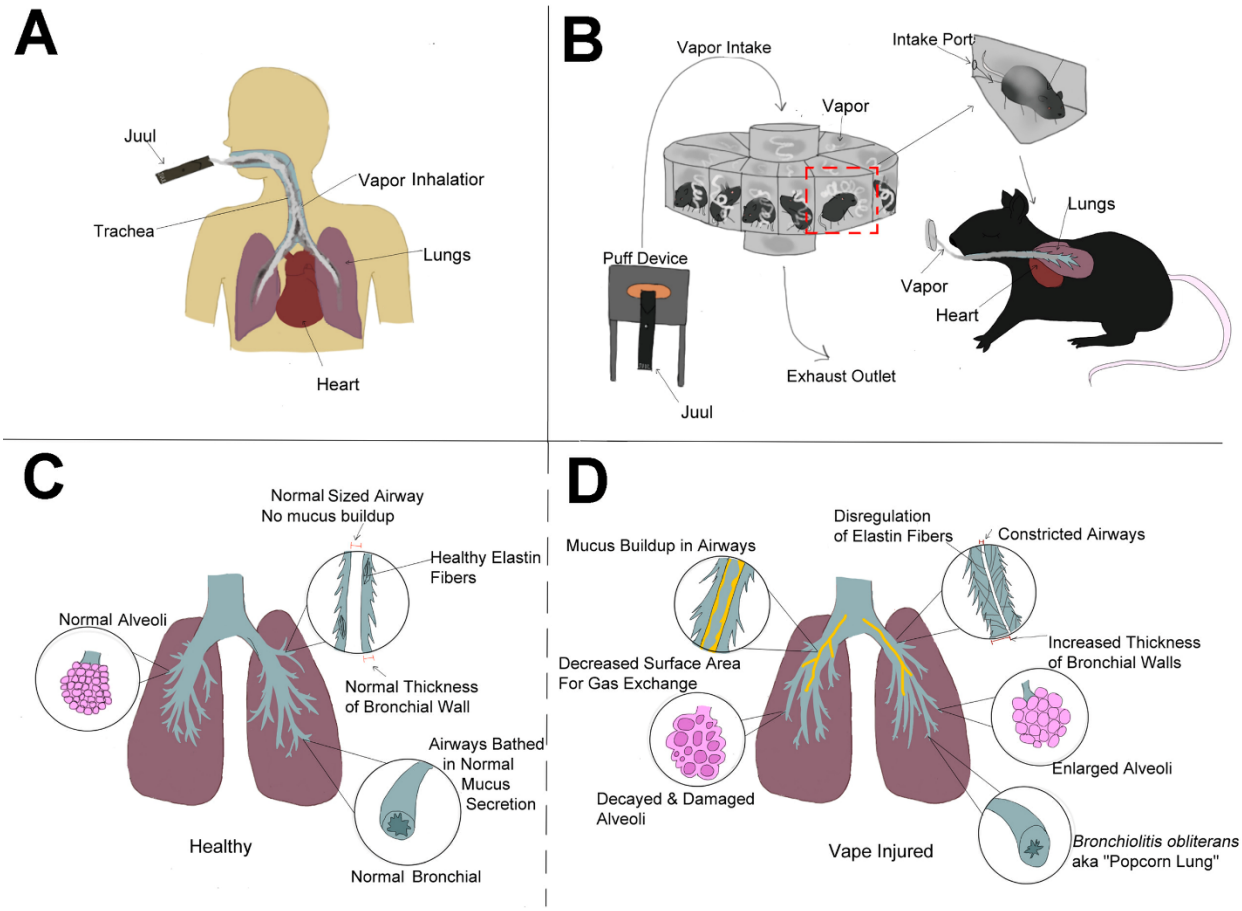

Figure 4.10 VAPI modeling and pathology.

Schematic representation comparative summary of inhalation exposure between humans (**A**) versus the InExpose murine model (**B**), and healthy lung biology (**C**) versus pathological changes observed in this study (**D**). Additional pathological changes in right ventricular structure leading to pulmonary failure were also observed, but are not represented in the diagram.

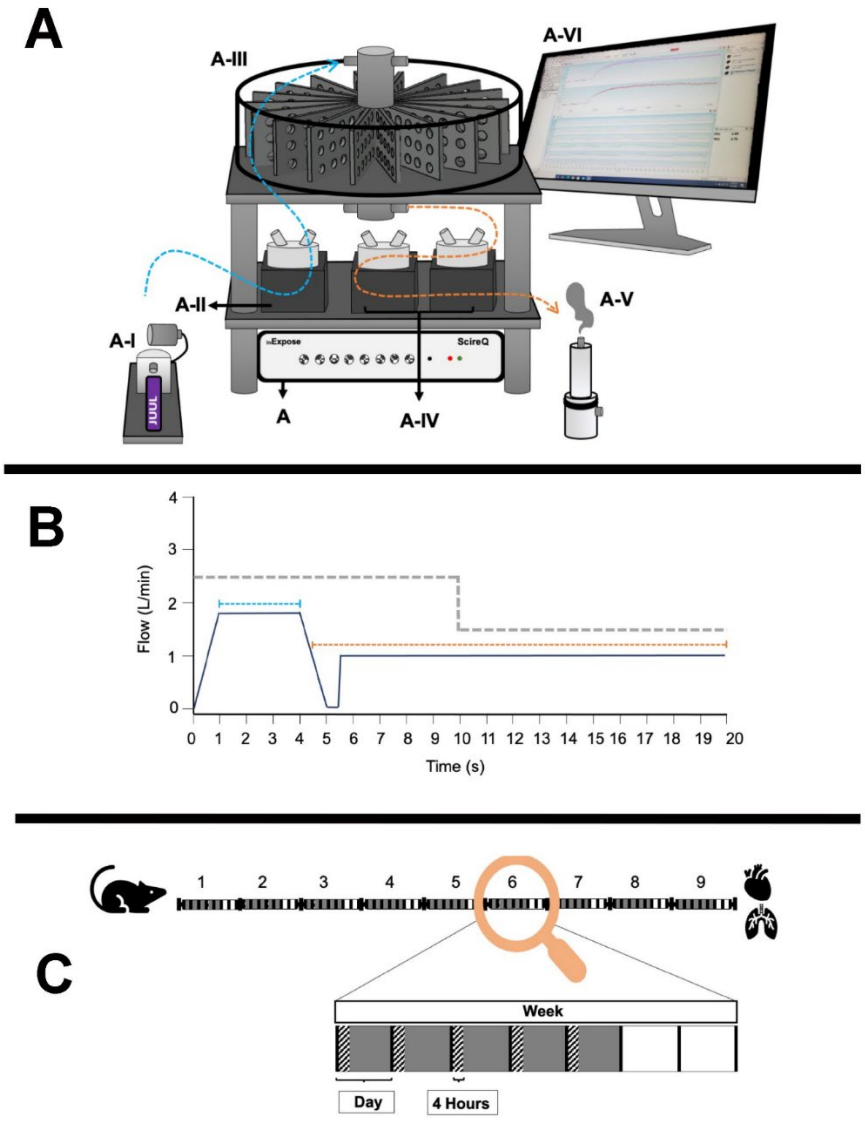

Figure 4.11 Vaping protocol details showing InExpose equipment, vaping topography profile, and time course of exposure schematic.

(A) InExpose base unit is software controlled to regulate exposure time and duration (A). ENDS device stroke controller ensures consistent e-vapor deposition (A-I). InExpose pump 1 generates e-vapor puffs (A-II; one pump per exposure chamber, only one pump shown). Whole body chamber houses up to 16 subjects for simultaneous exposure (A-III). InExpose exhaust pumps 2 and 3 (A-IV; one pump per exposure chamber). Buffer chamber pulls vapor from exposure chamber in order to circulate fresh air during inter-puff intervals (A-V). FlexiWare software controls the base unit to regulate vaping topography time and duration (A-VI). (B) Schematic of vaping topography. Mice in exposure chambers received e-vapor delivered in 3 s puffs (blue dashed line; 1.8 liters/min flow rate) in 20 s intervals (orange dashed line; 1 liter/min air flow rate). Exhaust pump flow rate alternated between puff and interval at rates of 2.5 liters/min and 1.5 liters/min, respectively (grey dashed line). (C) C57BL/6J mice were exposed to Organx Peach Ice flavored vape juice delivered as e-vapor from JUUL pens. Chamber habitation for 4 h per day, 5 d per week over a 9-wk time course. Vaping Days (grey boxes), Exposure time (hatched rectangles), and Rest Days (white boxes) are shown.

4.8 Tables

Table 4.1 Antibodies used for immunohistochemistry.

Marker	Species	Company	Catalog #	Dilution
ECAD	Goat	R&D Systems	AF748	1:100
Vimentin	Chicken	Invitrogen	PA1-10003	1:400
CD11C	Rabbit	Cell Signaling Tech	97585S	1:200
RAGE	Goat	R&D Systems	AF1145	1:100
KRT5	Chicken	Biolegend	905901	1:200
AQ5	Rabbit	Abcam	Ab78486	1:400
CD9	Rabbit	Abcam	Ab92726	1:100
Alpha Tubulin	Rat	Biorad	1703	1:400
Muc5ac	Rabbit	US Biotech	1364248	1:100
Desmin	Rabbit	Abcam	Ab15200	1:200

Table 4.2 Echocardiographic measurements shown by experimental group and gender. Values represent mean ± standard deviation.

	No Vape Female	No Vape Male	Vape Female	Vape Male
EF	74.82± 0.464655	74.99±2.531607	64.95±3.74678	59.43±2.98888
FS	42.24±0.476157	42.66±2.090859	34.4±2.743135	30.66±1.985322
LV_Mass	81.53±18.11191	89.68±13.87718	80.95±4.805302	88.3±11.93415
LV_Vold	35.42±6.053918	42.03±7.525448	36.39±4.106111	44.07±6.537644
LV_Vols	8.916±1.502419	10.612±2.718028	12.75±1.988373	17.92±3.238416
LVIDd	3.007±0.212416	3.225±0.239866	3.045±0.139681	3.291±0.207086
LVIDs	1.736±0.115514	1.852±0.185913	1.997±0.119995	2.283±0.167831
IVSd	0.9405±0.08526	0.957±0.042974	0.8723±0.048719	0.9123±0.022281
IVSs	1.355±0.098609	1.382±0.093474	1.3±0.060127	1.265±0.108597
LVPWd	0.75±0.171771	0.726±0.035867	0.8028±0.043058	0.718±0.111153
LVPWs	0.8085±0.184679	0.7938±0.072507	0.8578±0.063111	0.7594±0.064659

Table 4.3 Parameters for cardiomyocyte length measurements.

Male Vape		Female Vape		Male No Vape		Female No Vape	
Sample #	Measurements	Sample #	Measurements	Sample #	Measurements	Sample #	Measurements
21053	25	21075	23	21061	29	21071	24
21099	38	21077	28	21042	19	21041	20
21044	43	21043	34	21113	35	21059	28
21065	27	21089	31				
Total Measurements: 133		Total Measurements: 116		Total Measurements: 83		Total Measurements: 72	
Mean: 62.51		Mean: 60.93		Mean: 56.92		Mean: 53.76	
% Increase: 8.94		% Increase: 11.77					

Table 4.4 Antibodies used for immunoblotting.

Marker	Species	Company	Catalog #	Dilution
CD11b	Rabbit	Abcam	Ab133357	1:500
CD11c	Rabbit	Cell Signaling	97585s	1:500
CD206	Rabbit	Abcam	Ab64693	1:500
CD45	Goat	R&D	AF114	1:500
E-Cadherin	Rabbit	R&D	AF748	1:500
Fibronectin	Rabbit	Sigma	F3648	1:250
GAPDH	Goat	Sicgen	AB0067	1:3000
HMGB1	Rabbit	Abcam	Ab18256	1:250
IL1-β	Rabbit	Invitrogen	P420B	1:50
IL-6	Mouse	Sino Biological	10395-MM19	1:250
MUC1	Rabbit	Abcam	Ab109185	1:250
MUC5AC	Rabbit	My Biosource	MBS2028179	1:200

REFERENCES

1. Quaife-Ryan, G. A., Sim, C. B., Ziemann, M., Kaspi, A., Rafehi, H., Ramialison, M., El-Osta, A., Hudson, J. E. & Porrello, E. R. Multicellular Transcriptional Analysis of Mammalian Heart Regeneration. *Circulation* **136**, 1123–1139 (2017).

2. Yu, J., Seldin, M. M., Fu, K., Li, S., Lam, L., Wang, P. & S, C. E. Y. D. *Topological Arrangement of Cardiac Fibroblasts Regulates Cellular Plasticity*. (2018). doi:10.1161/CIRCRESAHA.118.312589.

3. Torán, J. L., López, J. A., Gomes-Alves, P., Aguilar, S., Torroja, C., Trevisan-Herraz, M., Moscoso, I., Sebastião, M. J., Serra, M., Brito, C., Cruz, F. M., Sepúlveda, J. C., Abad, J. L., Galán-Arriola, C., Ibanez, B., Martínez, F., Fernández, M. E., Fernández-Aviles, F., Palacios, I., R-Borlado, L., Vázquez, J., Alves, P. M. & Bernad, A. Definition of a cell surface signature for human cardiac progenitor cells after comprehensive comparative transcriptomic and proteomic characterization. *Sci. Rep.* **9**, 1–16 (2019).

4. Gomes-Alves, P., Serra, M., Brito, C., R.-Borlado, L., López, J. A., Vázquez, J., Carrondo, M. J. T., Bernad, A. & Alves, P. M. Exploring analytical proteomics platforms toward the definition of human cardiac stem cells receptome. *Proteomics* **15**, 1332–1337 (2015).

5. Furtado, M. B., Costa, M. W., Pranoto, E. A., Salimova, E., Pinto, A. R., Lam, N. T., Park, A., Snider, P., Chandran, A., Harvey, R. P., Boyd, R., Conway, S. J., Pearson, J., Kaye, D. M. & Rosenthal, N. A. Cardiogenic Genes Expressed in Cardiac Fibroblasts Contribute to Heart Development and RepairNovelty and Significance. *Circ. Res.* **114**, 1422–1434 (2014).

6. DeLaughter, D. M., Bick, A. G., Wakimoto, H., McKean, D., Gorham, J. M., Kathiriya, I. S., Hinson, J. T., Homsy, J., Gray, J., Pu, W., Bruneau, B. G., Seidman, J. G. & Seidman, C. E. Single-Cell Resolution of Temporal Gene Expression during Heart Development. *Dev. Cell* **39**, 480–490 (2016).

7. Freeman, B. T., Jung, J. P. & Ogle, B. M. Single-Cell RNA-Seq of Bone Marrow-Derived Mesenchymal Stem Cells Reveals Unique Profiles of Lineage Priming. *PLoS One* **10**, e0136199 (2015).

8. Freeman, B. T., Jung, J. P. & Ogle, B. M. Single-cell RNA-seq reveals activation of unique gene groups as a consequence of stem cell-parenchymal cell fusion. *Sci. Rep.* **6**, 23270 (2016).

9. Wang, Y. & Navin, N. E. Advances and applications of single-cell sequencing technologies. *Mol. Cell* **58**, 598–609 (2015).

10. Wilson, N. K., Kent, D. G., Buettner, F., Shehata, M., Macaulay, I. C., Calero-Nieto, F. J., Sánchez Castillo, M., Oedekoven, C. A., Diamanti, E., Schulte, R., Ponting, C. P., Voet, T., Caldas, C., Stingl, J., Green, A. R., Theis, F. J. & Göttgens, B. Combined Single-Cell

Functional and Gene Expression Analysis Resolves Heterogeneity within Stem Cell Populations. *Cell Stem Cell* **16**, 712–724 (2015).

11. Zheng, G. X. Y., Terry, J. M., Belgrader, P., Ryvkin, P., Bent, Z. W., Wilson, R., Ziraldo, S. B., Wheeler, T. D., McDermott, G. P., Zhu, J., Gregory, M. T., Shuga, J., Montesclaros, L., Underwood, J. G., Masquelier, D. A., Nishimura, S. Y., Schnall-Levin, M., Wyatt, P. W., Hindson, C. M., Bharadwaj, R., Wong, A., Ness, K. D., Beppu, L. W., Deeg, H. J., McFarland, C., Loeb, K. R., Valente, W. J., Ericson, N. G., Stevens, E. A., Radich, J. P., Mikkelsen, T. S., Hindson, B. J. & Bielas, J. H. Massively parallel digital transcriptional profiling of single cells. *Nat. Commun.* **8**, 14049 (2017).

12. Guerrero-Juarez, C. F., Dedhia, P. H., Jin, S., Ruiz-Vega, R., Ma, D., Liu, Y., Yamaga, K., Shestova, O., Gay, D. L., Yang, Z., Kessenbrock, K., Nie, Q., Pear, W. S., Cotsarelis, G. & Plikus, M. V. Single-cell analysis reveals fibroblast heterogeneity and myeloid-derived adipocyte progenitors in murine skin wounds. *Nat. Commun.* **10**, 1–17 (2019).

13. Alpern, D., Gardeux, V., Russeil, J., Mangeat, B., Meireles-Filho, A. C. A., Breysse, R., Hacker, D. & Deplancke, B. BRB-seq: ultra-affordable high-throughput transcriptomics enabled by bulk RNA barcoding and sequencing. *Genome Biol.* **20**, 71 (2019).

14. Winkels, H., Ehinger, E., Vassallo, M., Buscher, K., Dinh, H. Q., Kobiyama, K., Hamers, A. A. J., Cochain, C., Vafadarnejad, E., Saliba, A.-E., Zernecke, A., Pramod, A. B., Ghosh, A. K., Anto Michel, N., Hoppe, N., Hilgendorf, I., Zirlik, A., Hedrick, C. C., Ley, K. & Wolf, D. Atlas of the Immune Cell Repertoire in Mouse Atherosclerosis Defined by Single-Cell RNA-Sequencing and Mass Cytometry. *Circ. Res.* **122**, 1675–1688 (2018).

15. Swiech, L., Avraham-Davidi, I., Habib, N., Trombetta, J. J., Heidenreich, M., Zhang, F., Hession, C., Regev, A. & Li, Y. Div-Seq: Single-nucleus RNA-Seq reveals dynamics of rare adult newborn neurons. *Science (80-.).* **353**, 925–928 (2016).

16. Paik, D. T., Tian, L., Lee, J., Sayed, N., Chen, I. Y., Rhee, S., Rhee, J.-W., Kim, Y., Wirka, R. C., Buikema, J. W., Wu, S. M., Red-Horse, K., Quertermous, T. & Wu, J. C. Large-Scale Single-Cell RNA-Seq Reveals Molecular Signatures of Heterogeneous Populations of Human Induced Pluripotent Stem Cell-Derived Endothelial Cells. *Circ. Res.* **123**, 443–450 (2018).

17. Skelly, D. A., Squiers, G. T., McLellan, M. A., Bolisetty, M. T., Robson, P., Rosenthal, N. A. & Pinto, A. R. Single-Cell Transcriptional Profiling Reveals Cellular Diversity and Intercommunication in the Mouse Heart. *Cell Rep.* **22**, 600–610 (2018).

18. Kim, T., Echeagaray, O. H., Wang, B. J., Casillas, A., Broughton, K. M., Kim, B. H. & Sussman, M. A. In situ transcriptome characteristics are lost following culture adaptation of adult cardiac stem cells. *Sci. Rep.* **8**, 1–9 (2018).

19. Liu, Z., Wang, L., Welch, J. D., Ma, H., Zhou, Y., Vaseghi, H. R., Yu, S., Wall, J. B., Alimohamadi, S., Zheng, M., Yin, C., Shen, W., Prins, J. F., Liu, J. & Qian, L. Single-cell

transcriptomics reconstructs fate conversion from fibroblast to cardiomyocyte. *Nature* **551**, 100–104 (2017).

20. Li, G., Plonowska, K., Kuppusamy, R., Sturzu, A. & Wu, S. M. Identification of cardiovascular lineage descendants at single-cell resolution. *Development* **142**, 846–857 (2015).

21. Chen, Z., Zhu, W., Bender, I., Gong, W., Kwak, I.-Y., Yellamilli, A., Hodges, T. J., Nemoto, N., Zhang, J., Garry, D. J. & van Berlo, J. H. Pathologic Stimulus Determines Lineage Commitment of Cardiac C-kit $^{+}$ Cells. *Circulation* **136**, 2359–2372 (2017).

22. Kanisicak, O., Khalil, H., Ivey, M. J., Karch, J., Maliken, B. D., Correll, R. N., Brody, M. J., J. Lin, S.-C., Aronow, B. J., Tallquist, M. D. & Molkentin, J. D. Genetic lineage tracing defines myofibroblast origin and function in the injured heart. *Nat. Commun.* **7**, 12260 (2016).

23. See, K., Tan, W. L. W., Lim, E. H., Tiang, Z., Lee, L. T., Li, P. Y. Q., Luu, T. D. A., Ackers-Johnson, M. & Foo, R. S. Single cardiomyocyte nuclear transcriptomes reveal a lincRNA-regulated de-differentiation and cell cycle stress-response in vivo. *Nat. Commun.* **8**, 1–13 (2017).

24. Broughton, K. M., Khieu, T., Nguyen, N., Rosa, M., Mohsin, S., Quijada, P., Wang, B. J., Echeagaray, O. H., Kubli, D. A., Kim, T., Firouzi, F., Monsanto, M. M., Gude, N. A., Adamson, R. M., Dembitsky, W. P., Davis, M. E. & Sussman, M. A. Cardiac interstitial tetraploid cells can escape replicative senescence in rodents but not large mammals. *Commun. Biol.* **2**, 205 (2019).

25. Zeng, W., Jiang, S., Kong, X., El-Ali, N., Ball, A. R., Ma, C. I. H., Hashimoto, N., Yokomori, K. & Mortazavi, A. Single-nucleus RNA-seq of differentiating human myoblasts reveals the extent of fate heterogeneity. *Nucleic Acids Res.* **44**, 1–13 (2016).

26. Lacar, B., Linker, S. B., Jaeger, B. N., Krishnaswami, S., Barron, J., Kelder, M., Parylak, S., Paquola, A., Venepally, P., Novotny, M., O'Connor, C., Fitzpatrick, C., Erwin, J., Hsu, J. Y., Husband, D., McConnell, M. J., Lasken, R. & Gage, F. H. Nuclear RNA-seq of single neurons reveals molecular signatures of activation. *Nat. Commun.* **7**, (2016).

27. Guillaumet-Adkins, A., Rodríguez-Esteban, G., Mereu, E., Mendez-Lago, M., Jaitin, D. A., Villanueva, A., Vidal, A., Martinez-Marti, A., Felip, E., Vivancos, A., Keren-Shaul, H., Heath, S., Gut, M., Amit, I., Gut, I. & Heyn, H. Single-cell transcriptome conservation in cryopreserved cells and tissues. *Genome Biol.* **18**, 1–15 (2017).

28. Schaum, N., Karkanias, J., Neff, N. F., May, A. P., Quake, S. R., Wyss-Coray, T., Darmanis, S., Batson, J., Botvinnik, O., Chen, M. B., Chen, S., Green, F., Jones, R. C., Maynard, A., Penland, L., Pisco, A. O., Sit, R. V., Stanley, G. M., Webber, J. T., Zanini, F., Baghel, A. S., Bakerman, I., Bansal, I., Berdnik, D., Bilen, B., Brownfield, D., Cain, C., Chen, M. B., Chen, S., Cho, M., Cirolia, G., Conley, S. D., Darmanis, S., Demers, A., Demir, K., de Morree, A., Divita, T., du Bois, H., Dulgeroff, L. B. T., Ebadi, H., Espinoza, F. H., Fish,

M., Gan, Q., George, B. M., Gillich, A., Green, F., Genetiano, G., Gu, X., Gulati, G. S., Hang, Y., Hosseinzadeh, S., Huang, A., Iram, T., Isobe, T., Ives, F., Jones, R. C., Kao, K. S., Karnam, G., Kershner, A. M., Kiss, B. M., Kong, W., Kumar, M. E., Lam, J. Y., Lee, D. P., Lee, S. E., Li, G., Li, Q., Liu, L., Lo, A., Lu, W. J., Manjunath, A., May, A. P., May, K. L., May, O. L., Maynard, A., McKay, M., Metzger, R. J., Mignardi, M., Min, D., Nabhan, A. N., Neff, N. F., Ng, K. M., Noh, J., Patkar, R., Peng, W. C., Penland, L., Puccinelli, R., Rulifson, E. J., Schaum, N., Sikandar, S. S., Sinha, R., Sit, R. V., Szade, K., Tan, W., Tato, C., Tellez, K., Travaglini, K. J., Tropini, C., Waldburger, L., van Weele, L. J., Wosczyna, M. N., Xiang, J., Xue, S., Youngyunpipatkul, J., Zanini, F., Zardeneta, M. E., Zhang, F., Zhou, L., Bansal, I., Chen, S., Cho, M., Cirolia, G., Darmanis, S., Demers, A., Divita, T., Ebadi, H., Genetiano, G., Green, F., Hosseinzadeh, S., Ives, F., Lo, A., May, A. P., Maynard, A., McKay, M., Neff, N. F., Penland, L., Sit, R. V., Tan, W., Waldburger, L., Youngyunpipatkul, J., Batson, J., Botvinnik, O., Castro, P., Croote, D., Darmanis, S., DeRisi, J. L., Karkanias, J., Pisco, A. O., Stanley, G. M., Webber, J. T., Zanini, F., Baghel, A. S., Bakerman, I., Batson, J., Bilen, B., Botvinnik, O., Brownfield, D., Chen, M. B., Darmanis, S., Demir, K., de Morree, A., Ebadi, H., Espinoza, F. H., Fish, M., Gan, Q., George, B. M., Gillich, A., Gu, X., Gulati, G. S., Hang, Y., Huang, A., Iram, T., Isobe, T., Karnam, G., Kershner, A. M., Kiss, B. M., Kong, W., Kuo, C. S., Lam, J. Y., Lehallier, B., Li, G., Li, Q., Liu, L., Lu, W. J., Min, D., Nabhan, A. N., Ng, K. M., Nguyen, P. K., Patkar, R., Peng, W. C., Penland, L., Rulifson, E. J., Schaum, N., Sikandar, S. S., Sinha, R., Szade, K., Tan, S. Y., Tellez, K., Travaglini, K. J., Tropini, C., van Weele, L. J., Wang, B. M., Wosczyna, M. N., Xiang, J., Yousef, H., Zhou, L., Batson, J., Botvinnik, O., Chen, S., Darmanis, S., Green, F., May, A. P., Maynard, A., Pisco, A. O., Quake, S. R., Schaum, N., Stanley, G. M., Webber, J. T., Wyss-Coray, T., Zanini, F., Beachy, P. A., Chan, C. K. F., de Morree, A., George, B. M., Gulati, G. S., Hang, Y., Huang, K. C., Iram, T., Isobe, T., Kershner, A. M., Kiss, B. M., Kong, W., Li, G., Li, Q., Liu, L., Lu, W. J., Nabhan, A. N., Ng, K. M., Nguyen, P. K., Peng, W. C., Rulifson, E. J., Schaum, N., Sikandar, S. S., Sinha, R., Szade, K., Travaglini, K. J., Tropini, C., Wang, B. M., Weinberg, K., Wosczyna, M. N., Wu, S. M., Yousef, H., Barres, B. A., Beachy, P. A., Chan, C. K. F., Clarke, M. F., Darmanis, S., Huang, K. C., Karkanias, J., Kim, S. K., Krasnow, M. A., Kumar, M. E., Kuo, C. S., May, A. P., Metzger, R. J., Neff, N. F., Nusse, R., Nguyen, P. K., Rando, T. A., Sonnenburg, J., Wang, B. M., Weinberg, K., Weissman, I. L., Wu, S. M., Quake, S. R. & Wyss-Coray, T. Single-cell transcriptomics of 20 mouse organs creates a Tabula Muris. *Nature* **562**, 367–372 (2018).

29. Rodriques, S. G., Stickels, R. R., Goeva, A., Martin, C. A., Murray, E., Vanderburg, C. R., Welch, J., Chen, L. M., Chen, F. & Macosko, E. Z. Slide-seq: A scalable technology for measuring genome-wide expression at high spatial resolution. *Science (80-.).* **363**, 1463–1467 (2019).

30. Becht, E., McInnes, L., Healy, J., Dutertre, C. A., Kwok, I. W. H., Ng, L. G., Ginhoux, F. & Newell, E. W. Dimensionality reduction for visualizing single-cell data using UMAP. *Nat. Biotechnol.* **37**, 38–47 (2019).

31. Rostom, R., Svensson, V., Teichmann, S. A. & Kar, G. Computational approaches for interpreting scRNA-seq data. *FEBS Lett.* **591**, 2213–2225 (2017).

32. Leigh, N. D., Dunlap, G. S., Johnson, K., Mariano, R., Oshiro, R., Wong, A. Y., Bryant, D. M., Miller, B. M., Ratner, A., Chen, A., Ye, W. W., Haas, B. J. & Whited, J. L. Transcriptomic landscape of the blastema niche in regenerating adult axolotl limbs at single-cell resolution. *Nat. Commun.* **9**, (2018).

33. Sahraeian, S. M. E., Mohiyuddin, M., Sebra, R., Tilgner, H., Afshar, P. T., Au, K. F., Bani Asadi, N., Gerstein, M. B., Wong, W. H., Snyder, M. P., Schadt, E. & Lam, H. Y. K. Gaining comprehensive biological insight into the transcriptome by performing a broad-spectrum RNA-seq analysis. *Nat. Commun.* **8**, 1–14 (2017).

34. Halpern, K. B., Shenhav, R., Matcovitch-Natan, O., Tóth, B., Lemze, D., Golan, M., Massasa, E. E., Baydatch, S., Landen, S., Moor, A. E., Brandis, A., Giladi, A., Stokar-Avihail, A., David, E., Amit, I. & Itzkovitz, S. Single-cell spatial reconstruction reveals global division of labour in the mammalian liver. *Nature* **542**, 1–5 (2017).

35. Echeagaray, O. & Sussman, M. A. Transcribing the heart: faithfully interpreting cardiac transcriptional insights. *Regen. Med.* (2019) doi:10.2217/rme-2019-0063.

36. Januszyk, M., Rennert, R., Sorkin, M., Maan, Z., Wong, L., Whittam, A., Whitmore, A., Duscher, D. & Gurtner, G. Evaluating the Effect of Cell Culture on Gene Expression in Primary Tissue Samples Using Microfluidic-Based Single Cell Transcriptional Analysis. *Microarrays* **4**, 540–550 (2015).

37. Tekin, H., Simmons, S., Cummings, B., Gao, L., Adiconis, X., Hession, C. C., Ghoshal, A., Dionne, D., Choudhury, S. R., Yesilyurt, V., Sanjana, N. E., Shi, X., Lu, C., Heidenreich, M., Pan, J. Q., Levin, J. Z. & Zhang, F. Effects of 3D culturing conditions on the transcriptomic profile of stem-cell-derived neurons. *Nat. Biomed. Eng.* **2**, 540–554 (2018).

38. Kim, T., Echeagaray, O. H., Wang, B. J., Casillas, A., Broughton, K. M., Kim, B. & Sussman, M. A. In situ transcriptome characteristics are lost following culture adaptation of adult cardiac stem cells. *Sci. Rep.* 1–9 (2018) doi:10.1038/s41598-018-30551-1.

39. Mohsin, S., Khan, M., Nguyen, J., Alkatib, M., Siddiqi, S., Hariharan, N., Wallach, K., Monsanto, M., Gude, N., Dembitsky, W. & Sussman, M. A. Rejuvenation of human cardiac progenitor cells with pim-1 kinase. *Circ. Res.* **113**, 1169–1179 (2013).

40. Zhu, K., Wu, Q., Ni, C., Zhang, P., Zhong, Z., Wu, Y., Wang, Y., Xu, Y., Kong, M., Cheng, H., Tao, Z., Yang, Q., Liang, H., Jiang, Y., Li, Q., Zhao, J., Huang, J., Zhang, F., Chen, Q., Li, Y., Chen, J., Zhu, W., Yu, H., Zhang, J., Yang, H. T., Hu, X. & Wang, J. Lack of Remuscularization Following Transplantation of Human Embryonic Stem Cell-Derived Cardiovascular Progenitor Cells in Infarcted Nonhuman Primates. *Circ. Res.* **122**, 958–969 (2018).

41. Higuchi, A., Ku, N. J., Tseng, Y. C., Pan, C. H., Li, H. F., Kumar, S. S., Ling, Q. D., Chang, Y., Alarfaj, A. A., Munusamy, M. A., Benelli, G. & Murugan, K. Stem cell therapies for myocardial infarction in clinical trials: Bioengineering and biomaterial aspects. *Laboratory*

Investigation vol. 97 1167–1179 (2017).

42. Sanganalmath, S. K. & Bolli, R. Cell therapy for heart failure: A comprehensive overview of experimental and clinical studies, current challenges, and future directions. *Circ. Res.* **113**, 810–834 (2013).

43. Messina, E., De Angelis, L., Frati, G., Morrone, S., Chimenti, S., Fiordaliso, F., Salio, M., Battaglia, M., Latronico, M. V. G., Coletta, M., Vivarelli, E., Frati, L., Cossu, G. & Giacomello, A. Isolation and expansion of adult cardiac stem cells from human and murine heart. *Circ. Res.* **95**, 911–921 (2004).

44. Eschenhagen, T., Bolli, R., Braun, T., Field, L. J., Fleischmann, B. K., Frisén, J., Giacca, M., Hare, J. M., Houser, S., Lee, R. T., Marbán, E., Martin, J. F., Molkentin, J. D., Murry, C. E., Riley, P. R., Ruiz-Lozano, P., Sadek, H. A., Sussman, M. A. & Hill, J. A. Cardiomyocyte Regeneration. *Circulation* **136**, 680–686 (2017).

45. Van Der Sanden, B., Dhobb, M., Berger, F. & Wion, D. Optimizing stem cell culture. *J. Cell. Biochem.* **111**, 801–807 (2010).

46. Monsanto, M. M., White, K. S., Kim, T., Wang, B. J., Fisher, K., Ilves, K., Khalafalla, F. G., Casillas, A., Broughton, K., Mohsin, S., Dembitsky, W. P. & Sussman, M. A. Concurrent Isolation of 3 Distinct Cardiac Stem Cell Populations From a Single Human Heart BiopsyNovelty and Significance. *Circ. Res.* **121**, 113–124 (2017).

47. M, K., S, M., D, A., S, S., J, N., K, W., P, Q., M, M., N, G., R, A., DG, T., WJ, K. & MA, S. β-Adrenergic regulation of cardiac progenitor cell death versus survival and proliferation. *Circ. Res.* **112**, 476–486 (2013).

48. Macosko, E. Z., Basu, A., Satija, R., Nemesh, J., Shekhar, K., Goldman, M., Tirosh, I., Bialas, A. R., Kamitaki, N., Martersteck, E. M., Trombetta, J. J., Weitz, D. A., Sanes, J. R., Shalek, A. K., Regev, A. & McCarroll, S. A. Highly Parallel Genome-wide Expression Profiling of Individual Cells Using Nanoliter Droplets. *Cell* **161**, 1202–1214 (2015).

49. Stuart, T., Butler, A., Hoffman, P., Hafemeister, C., Papalexi, E., Mauck, W. M., Hao, Y., Stoeckius, M., Smibert, P. & Satija, R. Comprehensive Integration of Single-Cell Data. *Cell* **177**, 1888-1902.e21 (2019).

50. Tsuyuzaki, K., Sato, H., Sato, K. & Nikaido, I. Benchmarking principal component analysis for large-scale single-cell RNA-sequencing. *Genome Biol.* **21**, 1–17 (2020).

51. Yu, G., Wang, L.-G., Han, Y. & He, Q.-Y. clusterProfiler: an R package for comparing biological themes among gene clusters. *OMICS* **16**, 284–7 (2012).

52. McInnes, L., Healy, J. & Melville, J. UMAP: Uniform Manifold Approximation and Projection for Dimension Reduction. (2018).

53. Qiu, X., Mao, Q., Tang, Y., Wang, L., Chawla, R., Pliner, H. A. & Trapnell, C. Reversed graph embedding resolves complex single-cell trajectories. *Nat. Methods* **14**, 979–982 (2017).

54. Trapnell, C., Cacchiarelli, D., Grimsby, J., Pokharel, P., Li, S., Morse, M., Lennon, N. J., Livak, K. J., Mikkelsen, T. S. & Rinn, J. L. The dynamics and regulators of cell fate decisions are revealed by pseudotemporal ordering of single cells. *Nat. Biotechnol.* **32**, 381–386 (2014).

55. Satija, R. Cell cycle scoring and regression. https://satijalab.org/seurat/v3.1/cell_cycle_vignette.html.

56. Tirosh, I., Izar, B., Prakadan, S. M., Wadsworth, M. H., Treacy, D., Trombetta, J. J., Rotem, A., Rodman, C., Lian, C., Murphy, G., Fallahi-Sichani, M., Dutton-Regester, K., Lin, J. R., Cohen, O., Shah, P., Lu, D., Genshaft, A. S., Hughes, T. K., Ziegler, C. G. K., Kazer, S. W., Gaillard, A., Kolb, K. E., Villani, A. C., Johannessen, C. M., Andreev, A. Y., Van Allen, E. M., Bertagnolli, M., Sorger, P. K., Sullivan, R. J., Flaherty, K. T., Frederick, D. T., Jané-Valbuena, J., Yoon, C. H., Rozenblatt-Rosen, O., Shalek, A. K., Regev, A. & Garraway, L. A. Dissecting the multicellular ecosystem of metastatic melanoma by single-cell RNA-seq. *Science (80-.).* **352**, 189–196 (2016).

57. Tucker, N. R., Chaffin, M., Fleming, S. J., Hall, A. W., Parsons, V. A., Bedi, K. C., Akkad, A.-D., Herndon, C. N., Arduini, A., Papangeli, I., Roselli, C., Aguet, F., Choi, S. H., Ardlie, K. G., Babadi, M., Margulies, K. B., Stegmann, C. M. & Ellinor, P. T. Transcriptional and Cellular Diversity of the Human Heart. *Circulation* **142**, 466–482 (2020).

58. Alvarez, R., Wang, B. J., Quijada, P. J., Avitabile, D., Ho, T., Shaitrit, M., Chavarria, M., Firouzi, F., Ebeid, D., Monsanto, M. M., Navarrete, N., Moshref, M., Siddiqi, S., Broughton, K. M., Bailey, B. A., Gude, N. A. & Sussman, M. A. Cardiomyocyte cell cycle dynamics and proliferation revealed through cardiac-specific transgenesis of fluorescent ubiquitinated cell cycle indicator (FUCCI). *J. Mol. Cell. Cardiol.* **127**, 154–164 (2019).

59. Coppé, J.-P., Desprez, P.-Y., Krtolica, A. & Campisi, J. The senescence-associated secretory phenotype: the dark side of tumor suppression. *Annu. Rev. Pathol.* **5**, 99–118 (2010).

60. Lewis-McDougall, F. C., Ruchaya, P. J., Domenjo-Vila, E., Teoh, T. S., Prata, L., Cottle, B. J., Clark, J. E., Punjabi, P. P., Awad, W., Torella, D., Tchkonia, T., Kirkland, J. L. & Ellison-Hughes, G. M. Aged-senescent cells contribute to impaired heart regeneration. *Aging Cell* **18**, e12931 (2019).

61. Rodan, L. H., Anyane-Yeboa, K., Chong, K., Klein Wassink-Ruiter, J. S., Wilson, A., Smith, L., Kothare, S. V., Rajabi, F., Blaser, S., Ni, M., DeBerardinis, R. J., Poduri, A. & Berry, G. T. Gain-of-function variants in the *ODC1* gene cause a syndromic neurodevelopmental disorder associated with macrocephaly, alopecia, dysmorphic features, and neuroimaging abnormalities. *Am. J. Med. Genet. Part A* **176**, 2554–2560 (2018).

62. Mohsin, S., Khan, M., Nguyen, J., Alkatib, M., Siddiqi, S., Hariharan, N., Wallach, K., Monsanto, M., Gude, N., Dembitsky, W. & Sussman, M. A. Rejuvenation of Human Cardiac Progenitor Cells With Pim-1 Kinase. *Circ. Res.* **113**, 1169–1179 (2013).

63. Bujak, M. & Frangogiannis, N. G. The role of IL-1 in the pathogenesis of heart disease. *Archivum Immunologiae et Therapiae Experimentalis* vol. 57 165–176 (2009).

64. Kasner, M., Westermann, D., Lopez, B., Gaub, R., Escher, F., Kühl, U., Schultheiss, H. P. & Tschpe, C. Diastolic tissue doppler indexes correlate with the degree of collagen expression and cross-linking in heart failure and normal ejection fraction. *J. Am. Coll. Cardiol.* **57**, 977–985 (2011).

65. Zile, M. R., Baicu, C. F., Ikonomidis, J. S., Stroud, R. E., Nietert, P. J., Bradshaw, A. D., Slater, R., Palmer, B. M., Van Buren, P., Meyer, M., Redfield, M. M., Bull, D. A., Granzier, H. L. & LeWinter, M. M. Myocardial stiffness in patients with heart failure and a preserved ejection fraction contributions of collagen and titin. *Circulation* **131**, 1247–1259 (2015).

66. Ambardekar, A. V., Weiser-Evans, M. C. M., Li, M., Purohit, S. N., Aftab, M., Reece, T. B. & Moulton, K. S. Coronary Artery Remodeling and Fibrosis With Continuous-Flow Left Ventricular Assist Device Support. *Circ. Heart Fail.* **11**, e004491 (2018).

67. Fu, X., Liu, Q., Li, C., Li, Y. & Wang, L. Cardiac Fibrosis and Cardiac Fibroblast Lineage-Tracing: Recent Advances. *Frontiers in Physiology* vol. 11 (2020).

68. Snider, P., Standley, K. N., Wang, J., Azhar, M., Doetschman, T. & Conway, S. J. Origin of cardiac fibroblasts and the role of periostin. *Circ. Res.* **105**, 934–47 (2009).

69. Fu, W. bin, Wang, W. E. & Zeng, C. yu. Wnt signaling pathways in myocardial infarction and the therapeutic effects of Wnt pathway inhibitors. *Acta Pharmacologica Sinica* vol. 40 9–12 (2019).

70. Dodig, S., Čepelak, I. & Pavić, I. Hallmarks of senescence and aging. *Biochemia Medica* vol. 29 (2019).

71. Hariharan, N. & Sussman, M. A. Cardiac Aging – Getting to the Stem of the Problem. *J. Mol. Cell. Cardiol.* **83**, 32 (2015).

72. Pole, A., Dimri, M. & P. Dimri, G. Oxidative stress, cellular senescence and ageing. *AIMS Mol. Sci.* **3**, 300–324 (2016).

73. Carroll, B. & Korolchuk, V. I. Nutrient sensing, growth and senescence. *FEBS J.* **285**, 1948–1958 (2018).

74. Rajah, M. N., Bastianetto, S., Bromley-Brits, K., Cools, R., D'Esposito, M., Grady, C. L., Poirier, J., Quirion, R., Raz, N., Rogaeva, E., Song, W. & Pruessner, J. Biological changes

associated with healthy versus pathological aging: A symposium review. *Ageing Research Reviews* vol. 8 140–146 (2009).

75. Chen, H., Li, Y. & Tollefsbol, T. O. Cell senescence culturing methods. *Methods Mol. Biol.* **1048**, 1–10 (2013).

76. Noren Hooten, N. & Evans, M. K. Techniques to induce and quantify cellular senescence. *J. Vis. Exp.* **2017**, 55533 (2017).

77. Waaijer, M. E. C., Gunn, D. A., van Heemst, D., Eline Slagboom, P., Sedivy, J. M., Dirks, R. W., Tanke, H. J., Westendorp, R. G. J. & Maier, A. B. Do senescence markers correlate in vitro and in situ within individual human donors? *Aging (Albany. NY).* **10**, 278–289 (2018).

78. Dimri, G. P., Lee, X., Basile, G., Acosta, M., Scott, G., Roskelley, C., Medrano, E. E., Linskens, M., Rubelj, I., Pereira-Smith, O., Peacocke, M. & Campisi, J. A biomarker that identifies senescent human cells in culture and in aging skin in vivo. *Proc. Natl. Acad. Sci. U. S. A.* **92**, 9363–9367 (1995).

79. Sharpless, N. E. & Sherr, C. J. Forging a signature of in vivo senescence. *Nature Reviews Cancer* vol. 15 397–408 (2015).

80. Olariu, V., Harrison, N. J., Coca, D., Gokhale, P. J., Baker, D., Billings, S., Kadirkamanathan, V. & Andrews, P. W. Modeling the evolution of culture-adapted human embryonic stem cells. *Stem Cell Res.* **4**, 50–56 (2010).

81. Dong, Q., Wei, L., Zhang, M. Q. & Wang, X. Regulatory RNA binding proteins contribute to the transcriptome-wide splicing alterations in human cellular senescence. *Aging (Albany. NY).* **10**, 1489–1505 (2018).

82. Deschênes, M. & Chabot, B. The emerging role of alternative splicing in senescence and aging. *Aging Cell* vol. 16 918–933 (2017).

83. Harries, L. W., Hernandez, D., Henley, W., Wood, A. R., Holly, A. C., Bradley-Smith, R. M., Yaghootkar, H., Dutta, A., Murray, A., Frayling, T. M., Guralnik, J. M., Bandinelli, S., Singleton, A., Ferrucci, L. & Melzer, D. Human aging is characterized by focused changes in gene expression and deregulation of alternative splicing. *Aging Cell* **10**, 868–878 (2011).

84. Dorison, A., Ho, J. W. K., Wystub-Lis, K., Xaymardan, M., Farbehi, N., Patrick, R., Harvey, R. P., Nordon, R. E. & Janbandhu, V. Single-cell expression profiling reveals dynamic flux of cardiac stromal, vascular and immune cells in health and injury. *Elife* **8**, 1–39 (2019).

85. McLellan, M. A., Skelly, D. A., Dona, M. S. I., Squiers, G. T., Farrugia, G. E., Gaynor, T. L., Cohen, C. D., Pandey, R., Diep, H., Vinh, A., Rosenthal, N. A. & Pinto, A. R. High-Resolution Transcriptomic Profiling of the Heart During Chronic Stress Reveals Cellular Drivers of Cardiac Fibrosis and Hypertrophy. *Circulation* **142**, 1448–1463 (2020).

86. Perez-Gomez, A., Buxbaum, J. N. & Petrascheck, M. The aging transcriptome: read between the lines. *Current Opinion in Neurobiology* vol. 63 170–175 (2020).

87. Gaetani, R., Feyen, D. A. M., Doevendans, P. A., Gremmels, H., Forte, E., Fledderus, J. O., Ramjankhan, F. Z., Messina, E., Sussman, M. A., Giacomello, A. & Sluijter, J. P. G. Different types of cultured human adult Cardiac Progenitor Cells have a high degree of transcriptome similarity. *J. Cell. Mol. Med.* **18**, 2147–2151 (2014).

88. Kaur, G. & Cai, C. Current progress in the rejuvenation of aging stem/progenitor cells for improving the therapeutic effectiveness of myocardial repair. *Stem Cells International* vol. 2018 (2018).

89. Korski, K. I., Kubli, D. A., Wang, B. J., Khalafalla, F. G., Monsanto, M. M., Firouzi, F., Echeagaray, O. H., Kim, T., Adamson, R. M., Dembitsky, W. P., Gustafsson, Å. B. & Sussman, M. A. Hypoxia Prevents Mitochondrial Dysfunction and Senescence in Human c-Kit + Cardiac Progenitor Cells. *Stem Cells* (2019) doi:10.1002/stem.2970.

90. Kulandavelu, S., Karantalis, V., Fritsch, J., Hatzistergos, K. E., Loescher, V. Y., McCall, F., Wang, B., Bagno, L., Golpanian, S., Wolf, A., Grenet, J., Williams, A., Kupin, A., Rosenfeld, A., Mohsin, S., Sussman, M. A., Morales, A., Balkan, W. & Hare, J. M. Pim1 Kinase Overexpression Enhances ckit+ Cardiac Stem Cell Cardiac Repair Following Myocardial Infarction in Swine. *J. Am. Coll. Cardiol.* **68**, 2454–2464 (2016).

91. Li, J., Minami, I., Shiozaki, M., Yu, L., Yajima, S., Miyagawa, S., Shiba, Y., Morone, N., Fukushima, S., Yoshioka, M., Li, S., Qiao, J., Li, X., Wang, L., Kotera, H., Nakatsuji, N., Sawa, Y., Chen, Y. & Liu, L. Human Pluripotent Stem Cell-Derived Cardiac Tissue-like Constructs for Repairing the Infarcted Myocardium. *Stem Cell Reports* **9**, 1546–1559 (2017).

92. Voges, H. K., Mills, R. J., Elliott, D. A., Parton, R. G., Porrello, E. R. & Hudson, J. E. Development of a human cardiac organoid injury model reveals innate regenerative potential. *Dev.* **144**, 1118–1127 (2017).

93. Monsanto, M. M., Wang, B. J., Ehrenberg, Z. R., Echeagaray, O., White, K. S., Alvarez, R., Fisher, K., Sengphanith, S., Muliono, A., Gude, N. A. & Sussman, M. A. Enhancing myocardial repair with CardioClusters. *Nat. Commun.* **11**, 1–20 (2020).

94. Villarroel, M. A., Cha, A. E. & Vahratian, A. Electronic Cigarette Use Among U.S. Adults, 2018 Key findings Data from the National Health Interview Survey. (2018).

95. Wang, T. W. E-cigarette Use Among Middle and High School Students — United States, 2020. *MMWR. Morb. Mortal. Wkly. Rep.* **69**, 1310–1312 (2020).

96. Outbreak of Lung Injury Associated with the Use of E-Cigarette, or Vaping, Products | Electronic Cigarettes | Smoking & Tobacco Use | CDC.

https://www.cdc.gov/tobacco/basic_information/e-cigarettes/severe-lung-disease.html#epi-chart.

97. Blount, B. C., Karwowski, M. P., Shields, P. G., Morel-Espinosa, M., Valentin-Blasini, L., Gardner, M., Braselton, M., Brosius, C. R., Caron, K. T., Chambers, D., Corstvet, J., Cowan, E., De Jesús, V. R., Espinosa, P., Fernandez, C., Holder, C., Kuklenyik, Z., Kusovschi, J. D., Newman, C., Reis, G. B., Rees, J., Reese, C., Silva, L., Seyler, T., Song, M.-A., Sosnoff, C., Spitzer, C. R., Tevis, D., Wang, L., Watson, C., Wewers, M. D., Xia, B., Heitkemper, D. T., Ghinai, I., Layden, J., Briss, P., King, B. A., Delaney, L. J., Jones, C. M., Baldwin, G. T., Patel, A., Meaney-Delman, D., Rose, D., Krishnasamy, V., Barr, J. R., Thomas, J. & Pirkle, J. L. Vitamin E Acetate in Bronchoalveolar-Lavage Fluid Associated with EVALI. *N. Engl. J. Med.* **382**, 697–705 (2020).

98. Antoniewicz, L., Brynedal, A., Hedman, L., Lundbäck, M. & Bosson, J. A. Acute Effects of Electronic Cigarette Inhalation on the Vasculature and the Conducting Airways. *Cardiovasc. Toxicol.* **19**, 441–450 (2019).

99. Gonzalez, J. E. & Cooke, W. H. Acute effects of electronic cigarettes on arterial pressure and peripheral sympathetic activity in young nonsmokers. *Am. J. Physiol. - Hear. Circ. Physiol.* **320**, H248–H255 (2021).

100. Chaumont, M., De Becker, B., Zaher, W., Culié, A., Deprez, G., Mélot, C., Reyé, F., Van Antwerpen, P., Delporte, C., Debbas, N., Boudjeltia, K. Z. & Van De Borne, P. Differential Effects of E-Cigarette on Microvascular Endothelial Function, Arterial Stiffness and Oxidative Stress: A Randomized Crossover Trial. *Sci. Rep.* **8**, 1–9 (2018).

101. Qasim, H., Karim, Z. A., Rivera, J. O., Khasawneh, F. T. & Alshbool, F. Z. Impact of Electronic Cigarettes on the Cardiovascular System. *J. Am. Heart Assoc.* **6**, (2017).

102. Callahan-Lyon, P. Electronic cigarettes: human health effects. *Tob. Control* **23**, ii36–ii40 (2014).

103. Rigotti, N. A., Chang, Y., Tindle, H. A., Kalkhoran, S. M., Levy, D. E., Regan, S., Kelley, J. H. K., Davis, E. M. & Singer, D. E. Association of E-Cigarette Use With Smoking Cessation Among Smokers Who Plan to Quit After a Hospitalization. *https://doi.org/10.7326/M17-2048* **168**, 613–620 (2018).

104. Xu, X., Shrestha, S. S., Trivers, K. F., Neff, L., Armour, B. S. & King, B. A. U.S. healthcare spending attributable to cigarette smoking in 2014. *Prev. Med. (Baltim).* **150**, 106529 (2021).

105. 2014 Surgeon General's Report: The Health Consequences of Smoking—50 Years of Progress | CDC. https://www.cdc.gov/tobacco/data_statistics/sgr/50th-anniversary/index.htm#report.

106. Wehrli, F. W., Caporale, A., Langham, M. C. & Chatterjee, S. New Insights From MRI and

Cell Biology Into the Acute Vascular-Metabolic Implications of Electronic Cigarette Vaping. *Front. Physiol.* **0**, 492 (2020).

107. Smith, M., Gotway, M., Crotty Alexander, L. & Hariri, L. Vaping-related lung injury. *Virchows Arch.* **478**, 81–88 (2021).

108. Lilly, C., Khan, S., Waksmundzki-Silva, K. & Irwin, R. Vaping-Associated Respiratory Distress Syndrome: Case Classification and Clinical Guidance. *Crit. care Explor.* **2**, e0081 (2020).

109. Sussman, M. A. VAPIng into ARDS: Acute Respiratory Distress Syndrome and Cardiopulmonary Failure. *Pharmacol. Ther.* 108006 (2021) doi:10.1016/j.pharmthera.2021.108006.

110. Tsai, M., Byun, M. K., Shin, J. & Alexander, L. E. C. Effects of e-cigarettes and vaping devices on cardiac and pulmonary physiology. *J. Physiol.* **598**, 5039–5062 (2020).

111. Harvanko, A., CM, H., P, J. & NL, B. Characterization of Nicotine Salts in 23 Electronic Cigarette Refill Liquids. *Nicotine Tob. Res.* **22**, 1239–1243 (2020).

112. Kaur, G., Lungarella, G. & Rahman, I. SARS-CoV-2 COVID-19 susceptibility and lung inflammatory storm by smoking and vaping. *J. Inflamm. 2020 171* **17**, 1–8 (2020).

113. Amirahmadi, R., Childress, J., Patel, S. & Wagner, L.-A. Electric cigarette-related lung injury and cardiovascular insult. *BMJ Case Reports CP* **14**, e238352 (2021).

114. Sakla, N. M., Gattu, R., Singh, G. & Sadler, M. Vaping-associated acute respiratory distress syndrome. *Emerg. Radiol. 2019 271* **27**, 103–106 (2019).

115. MacDonald, A. & Middlekauff, H. R. Electronic cigarettes and cardiovascular health: what do we know so far? *Vasc. Health Risk Manag.* **15**, 159 (2019).

116. Garcia, P. D., Gornbein, J. A. & Middlekauff, H. R. Cardiovascular autonomic effects of electronic cigarette use: a systematic review. *Clin. Auton. Res.* **30**, 507 (2020).

117. Tarran, R., Barr, R. G., Benowitz, N. L., Bhatnagar, A., Chu, H. W., Dalton, P., Doerschuk, C. M., Drummond, M. B., Gold, D. R., Goniewicz, M. L., Gross, E. R., Hansel, N. N., Hopke, P. K., Kloner, R. A., Mikheev, V. B., Neczypor, E. W., Pinkerton, K. E., Postow, L., Rahman, I., Samet, J. M., Salathe, M., Stoney, C. M., Tsao, P. S., Widome, R., Xia, T., Xiao, D. & Wold, L. E. E-Cigarettes and Cardiopulmonary Health. *Function* **2**, 4 (2021).

118. Oakes, J. M., Xu, J., Morris, T. M., Fried, N. D., Pearson, C. S., Lobell, T. D., Gilpin, N. W., Lazartigues, E., Gardner, J. D. & Yue, X. Effects of Chronic Nicotine Inhalation on Systemic and Pulmonary Blood Pressure and Right Ventricular Remodeling in Mice. *Hypertension* 1305–1314 (2020) doi:10.1161/HYPERTENSIONAHA.119.14608.

119. Fried, N., TM, M., A, W., E, L., X, Y. & JD, G. Angiotensin II type 1 receptor mediates

pulmonary hypertension and right ventricular remodeling induced by inhaled nicotine. *Am. J. Physiol. Heart Circ. Physiol.* **320**, H1526–H1534 (2021).

120. Jia, G., Z, M., C, L., X, M., J, G., J, L., R, G., Z, Y., T, C., B, L., W, L., H, D., WB, L., X, J., J, Z., ZX, W., J, C. & Y, W. Nicotine induces cardiac toxicity through blocking mitophagic clearance in young adult rat. *Life Sci.* **257**, (2020).

121. Mayyas, F., H, A., KH, A., O, K., A, S. & T, E. Comparison of the cardiac effects of electronic cigarette aerosol exposure with waterpipe and combustible cigarette smoke exposure in rats. *Life Sci.* **251**, (2020).

122. Miller, C., H, S., D, L. & ML, G. Cross-Sectional Associations of Smoking and E-cigarette Use with Self-Reported Diagnosed Hypertension: Findings from Wave 3 of the Population Assessment of Tobacco and Health Study. *Toxics* **9**, (2021).

123. El-Mahdy, M., EM, M., MG, E., MS, E., TM, A. & JL, Z. Long-term electronic cigarette exposure induces cardiovascular dysfunction similar to tobacco cigarettes: role of nicotine and exposure duration. *Am. J. Physiol. Heart Circ. Physiol.* **320**, H2112–H2129 (2021).

124. Raymond, B. H., Collette-Merrill, K., Harrison, R. G., Jarvis, S. & Rasmussen, R. J. The nicotine content of a sample of E-cigarette liquid manufactured in the United States. *J. Addict. Med.* **12**, 127–131 (2018).

125. Abouassali, O., Chang, M., Chidipi, B., Martinez, J. L., Reiser, M., Kanithi, M., Soni, R., McDonald, T. V., Herweg, B., Saiz, J., Calcul, L. & Noujaim, S. F. In vitro and in vivo cardiac toxicity of flavored electronic nicotine delivery systems. *https://doi.org/10.1152/ajpheart.00283.2020* **320**, H133–H143 (2021).

126. Cheng, T. Chemical evaluation of electronic cigarettes. *Tob. Control* **23 Suppl 2**, (2014).

127. Zhao, L., W, D., J, C., J, S., MT, K. & RA, K. Acute administration of nicotine induces transient elevation of blood pressure and increases myocardial infarct size in rats. *Heliyon* **6**, (2020).

128. Hasan, K. M., Friedman, T. C., Parveen, M., Espinoza-Derout, J., Bautista, F., Razipour, M. M., Shao, X. M., Jordan, M. C., Roos, K. P., Mahata, S. K. & Sinha-Hikim, A. P. Electronic cigarettes cause alteration in cardiac structure and function in diet-induced obese mice. *PLoS One* **15**, e0239671 (2020).

129. Messner, B. & Bernhard, D. Smoking and Cardiovascular Disease. *Arterioscler. Thromb. Vasc. Biol.* **34**, 509–515 (2014).

130. Sumartiningsih, S., Lin, H. F. & Lin, J. C. Cigarette smoking blunts exercise-induced heart rate response among young adult male smokers. *Int. J. Environ. Res. Public Health* **16**, (2019).

131. George, J., Hussain, M., Vadiveloo, T., Ireland, S., Hopkinson, P., Struthers, A. D., Donnan, P. T., Khan, F. & Lang, C. C. Cardiovascular Effects of Switching From Tobacco Cigarettes to Electronic Cigarettes. *J. Am. Coll. Cardiol.* **74**, 3112–3120 (2019).

132. Haptonstall, K., Y, C., R, M., K, N., E, T., K, L., I, R., J, G. & HR, M. Differential effects of tobacco cigarettes and electronic cigarettes on endothelial function in healthy young people. *Am. J. Physiol. Heart Circ. Physiol.* **319**, H547–H556 (2020).

133. Rao, P., Liu, J. & Springer, M. L. JUUL and Combusted Cigarettes Comparably Impair Endothelial Function. *Tob. Regul. Sci.* **6**, 30 (2020).

134. Chatterjee, S., Caporale, A., Tao, J. Q., Guo, W., Johncola, A., Strasser, A. A., Leone, F. T., Langham, M. C. & Wehrli, F. W. Acute e-cig inhalation impacts vascular health: a study in smoking naïve subjects. *https://doi.org/10.1152/ajpheart.00628.2020* **320**, H144–H158 (2021).

135. Kuntic, M., M, O., S, S., S, K.-S., P, S., S, K., K, F., K, V.-M., MT, B. J., M, K., K, F., A, A. Z., V, B., O, H., S, D., F, V., T, G., R, H., T, H., FP, S., JF, K., A, D. & T, M. Short-term e-cigarette vapour exposure causes vascular oxidative stress and dysfunction: evidence for a close connection to brain damage and a key role of the phagocytic NADPH oxidase (NOX-2). *Eur. Heart J.* **41**, 2472-2483A (2020).

136. E, K., AS, V., Z, S., A, Z., K, P., G, L. & D, K. The flavoring and not the nicotine content is a decisive factor for the effects of refill liquids of electronic cigarette on the redox status of endothelial cells. *Toxicol. reports* **7**, 1095–1102 (2020).

137. Jaleel, Z., E, B., C, T., P, M., S, M., HP, G., NA, C., M, P. & J, S. Association of vaping with decreased vascular endothelial growth factor expression and decreased microvessel density in cutaneous wound healing tissue in rats. *Wound Repair Regen.* (2021) doi:10.1111/WRR.12945.

138. Sahota, A., S, N., A, J., C, G., M, W., ZA, F. & V, M. Atherosclerosis inflammation and burden in young adult smokers and vapers measured by PET/MR. *Atherosclerosis* **325**, 110–116 (2021).

139. Li, J., L, H., WD, C., MS, T., H, S., J, H., B, K., TJ, R., H, Z., MB, S., L, T. T. Le, L, Z., K, P., C, L. & H, W. Electronic Cigarettes Induce Mitochondrial DNA Damage and Trigger TLR9 (Toll-Like Receptor 9)-Mediated Atherosclerosis. *Arterioscler. Thromb. Vasc. Biol.* **41**, 839–853 (2021).

140. Franzen, K. F., Willig, J., Cayo Talavera, S., Meusel, M., Sayk, F., Reppel, M., Dalhoff, K., Mortensen, K. & Droemann, D. E-cigarettes and cigarettes worsen peripheral and central hemodynamics as well as arterial stiffness: A randomized, double-blinded pilot study. *Vasc. Med. (United Kingdom)* **23**, 419–425 (2018).

141. Münzel, T., Hahad, O., Kuntic, M., Keaney, J. F., Deanfield, J. E. & Daiber, A. Effects of

tobacco cigarettes, e-cigarettes, and waterpipe smoking on endothelial function and clinical outcomes. *Eur. Heart J.* **41**, 4057–4070 (2020).

142. Münzel, T., GG, C., C, M., NR, B., V, F. & JC, K. Impact of Oxidative Stress on the Heart and Vasculature: Part 2 of a 3-Part Series. *J. Am. Coll. Cardiol.* **70**, 212–229 (2017).

143. Basma, H., S, T., K, D., F, Q., S, R. & BD, L. Electronic cigarette extract induced toxic effect in iPS-derived cardiomyocytes. *BMC Cardiovasc. Disord.* **20**, (2020).

144. Chaumont, M., P, van de B., A, B., A, V. M., G, D., J, U., E, S., R, B., Q, de H., W, Z. & N, D. Fourth generation e-cigarette vaping induces transient lung inflammation and gas exchange disturbances: results from two randomized clinical trials. *Am. J. Physiol. Lung Cell. Mol. Physiol.* **316**, L705–L719 (2019).

145. MC, M., CT, L., BH, G., CY, C., HY, T., R, Y., MJ, H., N, B., LZ, S., P, P., N, P., R, S., BE, G., I, L., MJ, C., DB, C. & F, K. Electronic cigarettes disrupt lung lipid homeostasis and innate immunity independent of nicotine. *J. Clin. Invest.* **129**, 4290–4304 (2019).

146. Muthumalage, T., Lamb, T., Friedman, M. R. & Rahman, I. E-cigarette flavored pods induce inflammation, epithelial barrier dysfunction, and DNA damage in lung epithelial cells and monocytes. *Sci. Reports 2019 91* **9**, 1–11 (2019).

147. SE, P. Testing for lipid-laden macrophages in bronchoalveolar lavage fluid to diagnose vaping-associated pulmonary injury. Are we there yet? *J. Am. Soc. Cytopathol.* **9**, 1–8 (2020).

148. PG, S., MA, S., JL, F., TM, B., JP, M., SA, R., DY, W., R, R., T, E., MD, W. & K, S. Lipid laden macrophages and electronic cigarettes in healthy adults. *EBioMedicine* **60**, (2020).

149. Szafran, B. N., Pinkston, R., Perveen, Z., Ross, M. K., Morgan, T., Paulsen, D. B., Penn, A. L., Kaplan, B. L. F. & Noël, A. Electronic-Cigarette Vehicles and Flavoring Affect Lung Function and Immune Responses in a Murine Model. *Int. J. Mol. Sci.* **21**, 1–22 (2020).

150. KJ, M., FJ, S. & EA, F. Macrophages in atherosclerosis: a dynamic balance. *Nat. Rev. Immunol.* **13**, 709–721 (2013).

151. Kelesidis, T., E, T., S, A., K, L., R, H., J, G. & HR, M. Elevated Cellular Oxidative Stress in Circulating Immune Cells in Otherwise Healthy Young People Who Use Electronic Cigarettes in a Cross-Sectional Single-Center Study: Implications for Future Cardiovascular Risk. *J. Am. Heart Assoc.* **9**, (2020).

152. Benowitz, N., G, S. H., N, N., N, A., JJ, Z., AM, H., CS, C. & P, J. Twenty-Four-Hour Cardiovascular Effects of Electronic Cigarettes Compared With Cigarette Smoking in Dual Users. *J. Am. Heart Assoc.* **9**, (2020).

153. Lee, W. H., Ong, S. G., Zhou, Y., Tian, L., Bae, H. R., Baker, N., Whitlatch, A.,

Mohammadi, L., Guo, H., Nadeau, K. C., Springer, M. L., Schick, S. F., Bhatnagar, A. & Wu, J. C. Modeling Cardiovascular Risks of E-Cigarettes With Human-Induced Pluripotent Stem Cell–Derived Endothelial Cells. *J. Am. Coll. Cardiol.* **73**, 2722–2737 (2019).

154. Kaur, G., Lungarella, G. & Rahman, I. SARS-CoV-2 COVID-19 susceptibility and lung inflammatory storm by smoking and vaping. *J. Inflamm. 2020 171* **17**, 1–8 (2020).

155. Lan, Y., Liu, W. & Zhou, Y. Right Ventricular Damage in COVID-19: Association Between Myocardial Injury and COVID-19. *Front. Cardiovasc. Med.* **0**, 82 (2021).

156. Angelidis, I., Simon, L. M., Fernandez, I. E., Strunz, M., Mayr, C. H., Greiffo, F. R., Tsitsiridis, G., Ansari, M., Graf, E., Strom, T.-M., Nagendran, M., Desai, T., Eickelberg, O., Mann, M., Theis, F. J. & Schiller, H. B. An atlas of the aging lung mapped by single cell transcriptomics and deep tissue proteomics. *Nat. Commun. 2019 101* **10**, 1–17 (2019).

157. Reyfman, P. A., Walter, J. M., Joshi, N., Anekalla, K. R., McQuattie-Pimentel, A. C., Chiu, S., Fernandez, R., Akbarpour, M., Chen, C. I., Ren, Z., Verma, R., Abdala-Valencia, H., Nam, K., Chi, M., Han, S. H., Gonzalez-Gonzalez, F. J., Soberanes, S., Watanabe, S., Williams, K. J. N., Flozak, A. S., Nicholson, T. T., Morgan, V. K., Winter, D. R., Hinchcliff, M., Hrusch, C. L., Guzy, R. D., Bonham, C. A., Sperling, A. I., Bag, R., Hamanaka, R. B., Mutlu, G. M., Yeldandi, A. V., Marshall, S. A., Shilatifard, A., Amaral, L. A. N., Perlman, H., Sznajder, J. I., Christine Argento, A., Gillespie, C. T., Dematte, J., Jain, M., Singer, B. D., Ridge, K. M., Lam, A. P., Bharat, A., Bhorade, S. M., Gottardi, C. J., Scott Budinger, G. R. & Misharin, A. V. Single-cell transcriptomic analysis of human lung provides insights into the pathobiology of pulmonary fibrosis. *Am. J. Respir. Crit. Care Med.* **199**, 1517–1536 (2019).

158. Duclos, G. E., Teixeira, V. H., Autissier, P., Gesthalter, Y. B., Reinders-Luinge, M. A., Terrano, R., Dumas, Y. M., Liu, G., Mazzilli, S. A., Brandsma, C. A., van den Berge, M., Janes, S. M., Timens, W., Lenburg, M. E., Spira, A., Campbell, J. D. & Beane, J. Characterizing smoking-induced transcriptional heterogeneity in the human bronchial epithelium at single-cell resolution. *Sci. Adv.* **5**, 1–12 (2019).

159. Forte, E., Skelly, D. A., Chen, M., Daigle, S., Morelli, K. A., Hon, O., Philip, V. M., Costa, M. W., Rosenthal, N. A. & Furtado, M. B. Dynamic Interstitial Cell Response during Myocardial Infarction Predicts Resilience to Rupture in Genetically Diverse Mice. *Cell Rep.* **30**, 3149-3163.e6 (2020).

160. Molenaar, B., Timmer, L. T., Droog, M., Perini, I., Versteeg, D., Kooijman, L., Monshouwer-Kloots, J., de Ruiter, H., Gladka, M. M. & van Rooij, E. Single-cell transcriptomics following ischemic injury identifies a role for B2M in cardiac repair. *Commun. Biol.* **4**, 1–15 (2021).

161. Tyser, R. C. V., Ibarra-Soria, X., McDole, K., Jayaram, S. A., Godwin, J., Brand, T. A. H. V. Den, Miranda, A. M. A., Scialdone, A., Keller, P. J., Marioni, J. C. & Srinivas, S. Characterization of a common progenitor pool of the epicardium and myocardium. *Science*

(80-.). **371**, 1–18 (2021).

162. Echeagaray, O., Kim, T., Casillas, A., Monsanto, M. & Sussman, M. Transcriptional features of biological age maintained in human cultured cardiac interstitial cells. *Genomics* **113**, 3705–3717 (2021).

163. H, S., Y, Z., L, F., H, C. & G, G. scMCA: A Tool to Define Mouse Cell Types Based on Single-Cell Digital Expression. *Methods Mol. Biol.* **1935**, 91–96 (2019).

164. Han, X., Wang, R., Zhou, Y., Fei, L., Sun, H., Lai, S., Saadatpour, A., Zhou, Z., Chen, H., Ye, F., Huang, D., Xu, Y., Huang, W., Jiang, M., Jiang, X., Mao, J., Chen, Y., Lu, C., Xie, J., Fang, Q., Wang, Y., Yue, R., Li, T., Huang, H., Orkin, S. H., Yuan, G.-C., Chen, M. & Guo, G. Mapping the Mouse Cell Atlas by Microwell-Seq. *Cell* **172**, 1091-1107.e17 (2018).

165. Winkels, H., Ehinger, E., Vassallo, M., Buscher, K., Dinh, H. Q., Kobiyama, K., Hamers, A. A. J., Cochain, C., Vafadarnejad, E., Saliba, A., Zernecke, A., Pramod, A. B., Ghosh, A. K., Michel, N. A., Hoppe, N., Hilgendorf, I., Zirlik, A., Hedrick, C. C., Ley, K., Wolf, D. & Rna-sequencing, A. D. S. Atlas of the Immune Cell Repertoire in Mouse and Mass Cytometry. (2018) doi:10.1161/CIRCRESAHA.117.312513.

166. Yoshida, K., Gowers, K. H. C., Lee-Six, H., Chandrasekharan, D. P., Coorens, T., Maughan, E. F., Beal, K., Menzies, A., Millar, F. R., Anderson, E., Clarke, S. E., Pennycuick, A., Thakrar, R. M., Butler, C. R., Kakiuchi, N., Hirano, T., Hynds, R. E., Stratton, M. R., Martincorena, I., Janes, S. M. & Campbell, P. J. Tobacco smoking and somatic mutations in human bronchial epithelium. *Nat. 2020 5787794* **578**, 266–272 (2020).

167. Zochios, V., Parhar, K., Tunnicliffe, W., Roscoe, A. & Gao, F. The Right Ventricle in ARDS. *Chest* **152**, 181–193 (2017).

168. Repessé, X. & Vieillard-Baron, A. Right heart function during acute respiratory distress syndrome Historical and physiological background. *Ann Transl Med* **5**, 295 (2017).

169. Arrigo, M., Huber, L. C., Winnik, S., Mikulicic, F., Guidetti, F., Frank, M., Flammer, A. J. & Ruschitzka, F. Right Ventricular Failure: Pathophysiology, Diagnosis and Treatment. *Card. Fail. Rev.* **5**, 140–146 (2019).

170. Esquer, C., Echeagaray, O., Firouzi, F., Savko, C., Shain, G., Bose, P., Rieder, A., Rokaw, S., Witon-Paulo, A., Gude, N. & Sussman, M. A. Fundamentals of vaping-associated pulmonary injury leading to severe respiratory distress. *Life Sci. Alliance* **5**, e202101246 (2022).

171. Cuccia, A. F., Patel, M., Amato, M. S., Stephens, D. K., Yoon, S. N. & Vallone, D. M. Quitting e-cigarettes: Quit attempts and quit intentions among youth and young adults. *Prev. Med. Reports* **21**, 2211–3355 (2021).

172. Amin, A. A., Haught, E. & Mousattat, Y. Do Not Huff, Puff, or Vape That Stuff: Interstitial Airspace Disease in a Teenager. *Case Rep. Pediatr.* **2020**, 1–4 (2020).

173. Fairchild, A., Healton, C., Curran, J., Abrams, D. & Bayer, R. Evidence, alarm, and the debate over e-cigarettes. *Science (80-.).* **366**, 1318–1320 (2019).

174. Kreslake, J. M., Diaz, M. C., Shinaba, M., Vallone, D. M. & Hair, E. C. Youth and young adult risk perceptions and behaviours in response to an outbreak of e-cigarette/vaping-associated lung injury (EVALI) in the USA. *Tob. Control* **31**, 88–97 (2022).

175. Casey, A. M., Muise, E. D. & Crotty Alexander, L. E. Vaping and e-cigarette use. Mysterious lung manifestations and an epidemic. *Curr. Opin. Immunol.* **66**, 143 (2020).

176. Balmes, J. R. Vaping-induced acute lung injury: An epidemic that could have been prevented. *Am. J. Respir. Crit. Care Med.* **200**, 1342–1344 (2019).

177. Chen, J., English, S., Ogilvie, J. A., Siu, M. K. M., Tammara, A. & Haas, C. J. All up in smoke: vaping-associated lung injury. *J. Community Hosp. Intern. Med. Perspect.* **10**, 571 (2020).

178. Hartmann-Boyce, J., McRobbie, H., Lindson, N., Bullen, C., Begh, R., Theodoulou, A., Notley, C., Rigotti, N. A., Turner, T., Butler, A. R., Fanshawe, T. R. & Hajek, P. Electronic cigarettes for smoking cessation. *Cochrane Database Syst. Rev.* **2021**, (2020).

179. Smith, K. E., Ikegwuonu, T., Weishaar, H. & Hilton, S. Evidence use in E-cigarettes debates: scientific showdowns in a 'wild west' of research. *BMC Public Health* **21**, 1–16 (2021).

180. McCausland, K., Maycock, B., Leaver, T., Wolf, K., Freeman, B. & Jancey, J. E-Cigarette Advocates on Twitter: Content Analysis of Vaping-Related Tweets. *JMIR Public Heal. Surveill 2020;6(4)e17543 https//publichealth.jmir.org/2020/4/e17543* **6**, e17543 (2020).

181. Akkanti, B. H., Hussain, R., Patel, M. K., Patel, J. A., Dinh, K., Zhao, B., Elzamly, S., Pelicon, K., Petek, K., Salas De Armas, I. A., Akay, M., Kar, B., Gregoric, I. D. & Buja, L. M. Deadly combination of Vaping-lnduced lung injury and Influenza: case report. *Diagn. Pathol.* **15**, (2020).

182. Al-abdouh, A., Phillips, E. & Allison, M. G. E-Cigarette or Vaping Product Use-Associated Lung Injury: A Severe Case That Responded to Corticosteroid Treatment. *Cureus* **12**, (2020).

183. Cecchini, M. J., Mukhopadhyay, S., Arrossi, A. V., Beasley, M. B., Butt, Y. M., Jones, K. D., Pambuccian, S., Mehrad, M., Monaco, S. E., Saqi, A., Smith, M. L., Tazelaar, H. D. & Larsen, B. T. E-Cigarette or Vaping Product Use-Associated Lung Injury: A Review for Pathologists. *Arch. Pathol. Lab. Med.* **144**, 1490–1500 (2020).

184. Chapman, R., Tweed, C. D. & Moonsie, I. Lung injury from e-cigarette use: a foul and pestilent congregation of vapours. *BMJ Case Reports CP* **13**, e237338 (2020).

185. Choi, H., Lin, Y., Race, E. & Macmurdo, M. G. Electronic cigarettes and alternative methods of vaping. *Ann. Am. Thorac. Soc.* **18**, 191–199 (2021).

186. Vogel, D. J., Fabbri, A., Falvo, A., Powell-Tuck, J., Desai, N., Vasques, F., Meadows, C., Ioannou, N., Glover, G., Brame, A., Sherren, P., Retter, A., Rajani, R. & Camporota, L. Assessment of Right Ventricular Function With CT and Echocardiography in Patients With Severe Acute Respiratory Distress Syndrome on Extracorporeal Membrane Oxygenation. *Crit. Care Explor.* **3**, e0345 (2021).

187. Balfour, D. J. K., Benowitz, N. L., Colby, S. M., Hatsukami, D. K., Lando, H. A., Leischow, S. J., Lerman, C., Mermelstein, R. J., Niaura, R., Perkins, K. A., Pomerleau, O. F., Rigotti, N. A., Swan, G. E., Warner, K. E. & West, R. Balancing Consideration of the Risks and Benefits of E-Cigarettes. *https://doi.org/10.2105/AJPH.2021.306416* **111**, 1661–1672 (2021).

188. Doxbeck, C. R. & Osberg, T. M. It's Not All Smoke and Mirrors: The Role of Social Norms, Alcohol Use, and Pandemic Partying in e-Cigarette Use During COVID-19. *https://doi.org/10.1080/10826084.2021.1942058* **56**, 1551–1558 (2021).

189. McAlinden, K. D., Lu, W., Eapen, M. S. & Sohal, S. S. Electronic cigarettes: Modern instruments for toxic lung delivery and posing risk for the development of chronic disease. *Int. J. Biochem. Cell Biol.* **137**, (2021).

190. Ruppel, T., Alexander, B. & Mayrovitz, H. N. Assessing Vaping Views, Usage, and Vaping-Related Education Among Medical Students: A Pilot Study. *Cureus* **13**, (2021).

191. McCausland, K., Maycock, B., Leaver, T., Wolf, K., Freeman, B. & Jancey, J. "Is it banned? Is it illegal?": Navigating Western Australia's regulatory environment for e-cigarettes. *Int. J. Drug Policy* **94**, 103177 (2021).

192. Sarles, S. E., Hensel, E. C., Robinson, R. J., Doherty, E., Nicholson, E. & O'donnell, D. Surveillance of U.S. Corporate Filings Provides a Proactive Approach to Inform Tobacco Regulatory Research Strategy. *Int. J. Environ. Res. Public Heal. 2021, Vol. 18, Page 3067* **18**, 3067 (2021).

193. Abouassali, O., Chang, M., Chidipi, B., Martinez, J. L., Reiser, M., Kanithi, M., Soni, R., McDonald, T. V., Herweg, B., Saiz, J., Calcul, L. & Noujaim, S. F. In vitro and in vivo cardiac toxicity of flavored electronic nicotine delivery systems. *https://doi.org/10.1152/ajpheart.00283.2020* **320**, H133–H143 (2021).

194. Scott, A., Lugg, S. T., Aldridge, K., Lewis, K. E., Bowden, A., Mahida, R. Y., Grudzinska, F. S., Dosanjh, D., Parekh, D., Foronjy, R., Sapey, E., Naidu, B. & Thickett, D. R. Pro-inflammatory effects of e-cigarette vapour condensate on human alveolar macrophages. *Thorax* **73**, 1161–1169 (2018).

195. Pinkston, R., Zaman, H., Hossain, E., Penn, A. L. & Noël, A. Cell-specific toxicity of short-term JUUL aerosol exposure to human bronchial epithelial cells and murine macrophages exposed at the air–liquid interface. *Respir. Res.* **21**, 1–15 (2020).

196. Singh, A. V., Maharjan, R. S., Kromer, C., Laux, P., Luch, A., Vats, T., Chandrasekar, V., Dakua, S. P. & Park, B. W. Advances in Smoking Related In Vitro Inhalation Toxicology: A Perspective Case of Challenges and Opportunities from Progresses in Lung-on-Chip Technologies. *Chem. Res. Toxicol.* **34**, 1984–2002 (2021).

197. Herr, C., Tsitouras, K., Niederstraßer, J., Backes, C., Beisswenger, C., Dong, L., Guillot, L., Keller, A. & Bals, R. Cigarette smoke and electronic cigarettes differentially activate bronchial epithelial cells. *Respir. Res.* **21**, 1–13 (2020).

198. Rayner, R. E., Makena, P., Prasad, G. L. & Cormet-Boyaka, E. Cigarette smoke preparations, not electronic nicotine delivery system preparations, induce features of lung disease in a 3D lung repeat-dose model. *Am. J. Physiol. Lung Cell. Mol. Physiol.* **320**, L276–L287 (2021).

199. Moshensky, A., Du, M., Shin, J., Advani, I., Gunge, D., Mathew, D., Alkolla, R., Du, A., Javier, C., Ma, L., Tran, A., Nguyen, N., Olay, J., Nilaad, S., Ding, J., Najhawan, M., Watrous, J. D., Bojanowksi, C. M., Jain, M., Christiani, D. C. & Alexander, L. E. C. Vaping-induced metabolomic signatures in the circulation of mice are driven by device type, e-liquid, exposure duration and sex. *ERJ Open Res.* **7**, 00229–02021 (2021).

200. Shi, H., Fan, X., Horton, A., Haller, S. T., Kennedy, D. J., Schiefer, I. T., Dworkin, L., Cooper, C. J. & Tian, J. The Effect of Electronic-Cigarette Vaping on Cardiac Function and Angiogenesis in Mice. *Sci. Reports 2019 91* **9**, 1–9 (2019).

201. Alasmari, F., Crotty Alexander, L. E., Drummond, C. A. & Sari, Y. A computerized exposure system for animal models to optimize nicotine delivery into the brain through inhalation of electronic cigarette vapors or cigarette smoke. *Saudi Pharm. J. SPJ* **26**, 622 (2018).

202. Dphil, N. E. & Eyal, N. Rescuing Vapers Versus Rescuing Smokers: The Ethics. *Nicotine Tob. Res.* **23**, 26–31 (2021).

203. Grill, K. E-cigarettes: The Long-Term Liberal Perspective. *Nicotine Tob. Res.* **23**, 9–13 (2021).

204. Lee, Y. H., Gawron, M. & Goniewicz, M. L. Changes in puffing behavior among smokers who switched from tobacco to electronic cigarettes. *Addict. Behav.* **48**, 1–4 (2015).

205. Mikheev, V. B., Buehler, S. S., Brinkman, M. C., Granville, C. A., Lane, T. E., Ivanov, A., Cross, K. M. & Clark, P. I. The Application of Commercially Available Mobile Cigarette Topography Devices for E-cigarette Vaping Behavior Measurements. *Nicotine Tob. Res.* **22**, 681–688 (2020).

206. Bertr, Dautzenberg & Bricard, D. Real-Time Characterization of E-Cigarettes Use: The 1 Million Puffs Study. *J. Addict. Res. Ther. 2015 62* **6**, 1–5 (2015).

207. Farsalinos, K. E., Romagna, G., Tsiapras, D., Kyrzopoulos, S. & Voudris, V. Evaluation of Electronic Cigarette Use (Vaping) Topography and Estimation of Liquid Consumption: Implications for Research Protocol Standards Definition and for Public Health Authorities' Regulation. *Int. J. Environ. Res. Public Heal. 2013, Vol. 10, Pages 2500-2514* **10**, 2500–2514 (2013).

208. Pfeiffer, J. A., Tompkins, L. K., Hart, J. L., Kesh, A., Groom, A., Vu, T. H. T., Ma, J. Z., Landry, R., Payne, T. J., Giachello, A. L., Robertson, R. M. & Walker, K. L. Relationship between population characteristics, e-cigaretteand tobacco-related perceptions, and likelihood of ever usinge-cigarettes. *Tob. Prev. Cessat.* **6**, 1–12 (2020).

209. Levy, D. T., Sánchez-Romero, L. M., Douglas, C. E. & Sweanor, D. T. An Analysis of the Altria-Juul Labs Deal: Antitrust and Population Health Implications. *J. Compet. Law Econ.* **17**, 458–492 (2021).

210. Patel, M., Cuccia, A., Willett, J., Zhou, Y., Kierstead, E. C., Czaplicki, L., Schillo, B., Hair, E. C. & Vallone, D. JUUL use and reasons for initiation among adult tobacco users. *Tob. Control* **28**, 681–684 (2019).

211. Talih, S., Salman, R., El-Hage, R., Karam, E., Karaoghlanian, N., El-Hellani, A., Saliba, N. & Shihadeh, A. Characteristics and toxicant emissions of JUUL electronic cigarettes. *Tob. Control* **28**, 678–680 (2019).

212. Groom, A. L., Vu, T. H. T., Kesh, A., Hart, J. L., Walker, K. L., Giachello, A. L., Sears, C. G., Tompkins, L. K., Mattingly, D. T., Landry, R. L., Robertson, R. M. & Payne, T. J. Correlates of youth vaping flavor preferences. *Prev. Med. Reports* **18**, 101094 (2020).

213. Landry, R. L., Groom, A. L., Vu, T. H. T., Stokes, A. C., Berry, K. M., Kesh, A., Hart, J. L., Walker, K. L., Giachello, A. L., Sears, C. G., McGlasson, K. L., Tompkins, L. K., Mattingly, D. T., Robertson, R. M. & Payne, T. J. The role of flavors in vaping initiation and satisfaction among U.S. adults. *Addict. Behav.* **99**, 106077 (2019).

214. Algiers, O., Wang, Y. & Laestadius, L. Content Analysis of U.S. Newspaper Coverage of Causes and Solutions to Vaping-Associated Lung Injury. *https://doi.org/10.1080/10826084.2021.1883663* **56**, 522–528 (2021).

215. Trivers, K. F., Watson, C. V., Neff, L. J., Jones, C. M. & Hacker, K. Tetrahydrocannabinol

(THC)-containing e-cigarette, or vaping, product use behaviors among adults after the onset of the 2019 outbreak of e-cigarette, or vaping, product use-associated lung injury (EVALI). *Addict. Behav.* **121**, 106990 (2021).

216. Diaban, F., Bunaye, Z., Vaziri, J. & Plisco, M. Vaping Induced Lung Injury Complicated by Right Ventricular Failure Leading to ECMO. *ATS 2020 Int. Conf. Am. Thorac. Soc. Int. Conf. Meet. Abstr.* A1959–A1959 (2020) doi:10.1164/AJRCCM-CONFERENCE.2020.201.1_MEETINGABSTRACTS.A1959.

217. Gay, B., Field, Z., Patel, S., Alvarez, R. M., Nasser, W., Madruga, M. & Carlan, S. J. Vaping-Induced Lung Injury: A Case of Lipoid Pneumonia Associated with E-Cigarettes Containing Cannabis. *Case Rep. Pulmonol.* **2020**, (2020).

218. Sood, S. B., Weatherly, A. J., Smith, A. H., Murphy, M. A., Conrad, S. J. & Bichell, D. P. Vaping Contributing to Postoperative Acute Respiratory Distress Syndrome. *Ann. Thorac. Surg.* **112**, e169–e171 (2021).

219. Fryman, C., Lou, B., Weber, A. G., Steinberg, H. N., Khanijo, S., Iakovou, A. & Makaryus, M. R. Acute Respiratory Failure Associated With Vaping. *Chest* **157**, e63–e68 (2020).

220. Kalantary, A., Abdelazeem, B., Shams, N., Pratiti, R. & Al-Sanouri, I. Coagulopathy and Acute Respiratory Distress Syndrome: Dual Complications of E-Cigarette-Associated Lung Injury. *Cureus* **13**, (2021).

221. Radicioni, G., Cao, R., Carpenter, J., Ford, A. A., Wang, T. T., Li, Y. & Kesimer, M. The innate immune properties of airway mucosal surfaces are regulated by dynamic interactions between mucins and interacting proteins: the mucin interactome. *Mucosal Immunol.* **9**, 1442 (2016).

222. Reidel, B., Radicioni, G., Clapp, P. W., Ford, A. A., Abdelwahab, S., Rebuli, M. E., Haridass, P., Alexis, N. E., Jaspers, I. & Kesimer, M. E-cigarette use causes a unique innate immune response in the lung, involving increased neutrophilic activation and altered mucin secretion. *Am. J. Respir. Crit. Care Med.* **197**, 492–501 (2018).

223. Post, S., Heijink, I. H., Hesse, L., Koo, H. K., Shaheen, F., Fouadi, M., Kuchibhotla, V. N. S., Lambrecht, B. N., Van Oosterhout, A. J. M., Hackett, T. L. & Nawijn, M. C. Characterization of a lung epithelium specific E-cadherin knock-out model: Implications for obstructive lung pathology. *Sci. Reports 2018 81* **8**, 1–12 (2018).

224. Frey, A., Lunding, L. P., Ehlers, J. C., Weckmann, M., Zissler, U. M. & Wegmann, M. More Than Just a Barrier: The Immune Functions of the Airway Epithelium in Asthma Pathogenesis. *Front. Immunol.* **11**, 761 (2020).

225. Nawijn, M. C., Hackett, T. L., Postma, D. S., van Oosterhout, A. J. M. & Heijink, I. H. E-cadherin: gatekeeper of airway mucosa and allergic sensitization. *Trends Immunol.* **32**, 248–255 (2011).

226. Sidhaye, V. K., Schweitzer, K. S., Caterina, M. J., Shimoda, L. & King, L. S. Shear stress regulates aquaporin-5 and airway epithelial barrier function. *Proc. Natl. Acad. Sci.* **105**, 3345–3350 (2008).

227. Hemler, M. E. Specific tetraspanin functions. *J. Cell Biol.* **155**, 1103–1108 (2001).

228. Termini, C. M. & Gillette, J. M. Tetraspanins function as regulators of cellular signaling. *Front. Cell Dev. Biol.* **5**, 34 (2017).

229. Wong, A. H. & Tran, T. CD151 in Respiratory Diseases. *Front. Cell Dev. Biol.* **8**, 64 (2020).

230. Christensen, J. E., Andreasen, S., Christensen, J. P. & Thomsen, A. R. CD11b expression as a marker to distinguish between recently activated effector CD8+ T cells and memory cells. *Int. Immunol.* **13**, 593–600 (2001).

231. Khan, S. Q., Khan, I. & Gupta, V. CD11b activity modulates pathogenesis of lupus nephritis. *Front. Med.* **5**, 52 (2018).

232. Cremades, M. J., Menéndez, R., Rubio, V. & Sanchis, J. Fibronectin in Bronchoalveolar Lavage Fluid in Lung Cancer: Tumor or Inflammatory Marker? *Respiration* **65**, 178–182 (1998).

233. Limper, A. H. & Roman, J. Fibronectin: A Versatile Matrix Protein with Roles in Thoracic Development, Repair and Infection. *Chest* **101**, 1663–1673 (1992).

234. Sakla, N. M., Gattu, R., Singh, G. & Sadler, M. Vaping-associated acute respiratory distress syndrome. *Emerg. Radiol.* **27**, 103–106 (2020).

235. Smith, M. L., Gotway, M. B., Crotty Alexander, L. E. & Hariri, L. P. Vaping-related lung injury. *Virchows Arch.* **478**, 1 (2021).

236. Mikolka, P., Kosutova, P., Balentova, S., Cierny, D., Kopincova, J., Kolomaznik, M., Adamkov, M., Calkovska, A. & Mokra, D. Early cardiac injury in acute respiratory distress syndrome: comparison of two experimental models. *Physiol. Res.* **69**, S421–S432 (2020).

237. Matute-Bello, G., Frevert, C. W. & Martin, T. R. Animal models of acute lung injury. *Am. J. Physiol. - Lung Cell. Mol. Physiol.* **295**, 379–399 (2008).

238. Edmonds, P. J., Copeland, C., Conger, A. & Richmond, B. W. Vaping-induced diffuse alveolar hemorrhage. *Respir. Med. Case Reports* **29**, 100996 (2020).

239. Mecham, R. P. Elastin in Lung Development and Disease Pathogenesis. *Matrix Biol.* **73**, 6 (2018).

240. Reddel, C. J., Weiss, A. S. & Burgess, J. K. Elastin in asthma. *Pulm. Pharmacol. Ther.* **25**,

144–153 (2012).

241. Tellez, C. S., Juri, D. E., Phillips, L. M., Do, K., Yingling, C. M., Thomas, C. L., Dye, W. W., Wu, G., Kishida, S., Kiyono, T. & Belinsky, S. A. Cytotoxicity and Genotoxicity of E-Cigarette Generated Aerosols Containing Diverse Flavoring Products and Nicotine in Oral Epithelial Cell Lines. *Toxicol. Sci.* **179**, 220–228 (2021).

242. ArRejaie, A. S., Al-Aali, K. A., Alrabiah, M., Vohra, F., Mokeem, S. A., Basunbul, G., Alrahlah, A. & Abduljabbar, T. Proinflammatory cytokine levels and peri-implant parameters among cigarette smokers, individuals vaping electronic cigarettes, and non-smokers. *J. Periodontol.* **90**, 367–374 (2019).

243. Phan, S. H. & Kunkel, S. L. Lung Cytokine Production in Bleomycin-Induced Pulmonary Fibrosis. *http://dx.doi.org/10.3109/01902149209020649* **18**, 29–43 (2009).

244. Tang, M. shong, Wu, X. R., Lee, H. W., Xia, Y., Deng, F. M., Moreira, A. L., Chen, L. C., Huang, W. C. & Lepor, H. Electronic-cigarette smoke induces lung adenocarcinoma and bladder urothelial hyperplasia in mice. *Proc. Natl. Acad. Sci. U. S. A.* **116**, 21727–21731 (2019).

245. Shacter, E. & Weitzman, S. A. Chronic inflammation and cancer. *Oncology (Williston Park, N.Y.)* vol. 16 (2002).

246. Haswell, L. E., Baxter, A., Banerjee, A., Verrastro, I., Mushonganono, J., Adamson, J., Thorne, D., Gaça, M. & Minet, E. Reduced biological effect of e-cigarette aerosol compared to cigarette smoke evaluated in vitro using normalized nicotine dose and RNA-seq-based toxicogenomics. *Sci. Reports 2017 71* **7**, 1–16 (2017).

247. Lee, K. M., Hoeng, J., Harbo, S., Kogel, U., Gardner, W., Oldham, M., Benson, E., Talikka, M., Kondylis, A., Martin, F., Titz, B., Ansari, S., Trivedi, K., Guedj, E., Elamin, A., Ivanov, N. V., Vanscheeuwijck, P., Peitsch, M. C. & McKinney, W. J. Biological changes in C57BL/6 mice following 3 weeks of inhalation exposure to cigarette smoke or e-vapor aerosols. *Inhal. Toxicol.* **30**, 553–567 (2018).

248. Park, H. R., O'Sullivan, M., Vallarino, J., Shumyatcher, M., Himes, B. E., Park, J. A., Christiani, D. C., Allen, J. & Lu, Q. Transcriptomic response of primary human airway epithelial cells to flavoring chemicals in electronic cigarettes. *Sci. Reports 2019 91* **9**, 1–11 (2019).

249. Phillips, G., Czekala, L., Behrsing, H. P., Amin, K., Budde, J., Stevenson, M., Wieczorek, R., Walele, T. & Simms, L. Acute electronic vapour product whole aerosol exposure of 3D human bronchial tissue results in minimal cellular and transcriptomic responses when compared to cigarette smoke: *https://doi.org/10.1177/2397847320988496* **5**, 239784732098849 (2021).

250. Shen, Y., Wolkowicz, M. J., Kotova, T., Fan, L. & Timko, M. P. Transcriptome sequencing

reveals e-cigarette vapor and mainstream-smoke from tobacco cigarettes activate different gene expression profiles in human bronchial epithelial cells. *Sci. Reports 2016 61* **6**, 1–17 (2016).

251. Menon, D., Innes, A., Oakley, A. J., Dahlstrom, J. E., Jensen, L. M., Brüstle, A., Tummala, P., Rooke, M., Casarotto, M. G., Baell, J. B., Nguyen, N., Xie, Y., Cuellar, M., Strasser, J., Dahlin, J. L., Walters, M. A., Burgio, G., O'Neill, L. A. J. & Board, P. G. GSTO1-1 plays a pro-inflammatory role in models of inflammation, colitis and obesity. *Sci. Reports 2017 71* **7**, 1–15 (2017).

252. Li, K., Li, M., Li, W., Yu, H., Sun, X., Zhang, Q., Li, Y., Li, X., Li, Y., Abel, E. D., Wu, Q. & Chen, H. Airway epithelial regeneration requires autophagy and glucose metabolism. (2019) doi:10.1038/s41419-019-2111-2.

253. Li, L., Wei, Y., Van Winkle, L., Zhang, Q., Zhou, X., Hu, J., Xie, F., Kluetzman, K. & Ding, X. Generation and characterization of a Cyp2f2-null mouse and studies on the role of CYP2F2 in naphthalene-induced toxicity in the lung and nasal olfactory mucosa. *J. Pharmacol. Exp. Ther.* **339**, 62–71 (2011).

254. Faiz, A., van den Berge, M., Vermeulen, C. J., ten Hacken, N. H. T., Guryev, V. & Pouwels, S. D. AGER expression and alternative splicing in bronchial biopsies of smokers and never smokers. *Respir. Res. 2019 201* **20**, 1–4 (2019).

255. Lee, H., Lee, J., Hong, S.-H., Rahman, I. & Yang, S.-R. Inhibition of RAGE Attenuates Cigarette Smoke-Induced Lung Epithelial Cell Damage via RAGE-Mediated Nrf2/DAMP Signaling. *Front. Pharmacol.* **9**, (2018).

256. Sanders, K. A., Delker, D. A., Huecksteadt, T., Beck, E., Wuren, T., Chen, Y., Zhang, Y., Hazel, M. W. & Hoidal, J. R. RAGE is a Critical Mediator of Pulmonary Oxidative Stress, Alveolar Macrophage Activation and Emphysema in Response to Cigarette Smoke. *Sci. Reports 2019 91* **9**, 1–16 (2019).

257. Wang, T., Li, B., Nelson, C. E. & Nabavi, S. Comparative analysis of differential gene expression analysis tools for single-cell RNA sequencing data. *BMC Bioinforma. 2019 201* **20**, 1–16 (2019).

258. Beltrami, C. A., Finato, N., Rocco, M., Feruglio, G. A., Puricelli, C., Cigola, E., Sonnenblick, E. H., Olivetti, G. & Anversa, P. The cellular basis of dilated cardiomyopathy in humans. *J. Mol. Cell. Cardiol.* **27**, 291–305 (1995).

259. Gerdes, A. M. & Capasso, J. M. Structural remodeling and mechanical dysfunction of cardiac myocytes in heart failure. *J. Mol. Cell. Cardiol.* **27**, 849–856 (1995).

260. Camper-Kirby, D., Welch, S., Walker, A., Shiraishi, I., Setchell, K. D. R., Schaefer, E., Kajstura, J., Anversa, P. & Sussman, M. A. Myocardial Akt Activation and Gender. *Circ. Res.* **88**, 1020–1027 (2001).

261. Fischer, K. M., Cottage, C. T., Konstandin, M. H., Völkers, M., Khan, M. & Sussman, M. A. Pim-1 Kinase Inhibits Pathological Injury by Promoting Cardioprotective Signaling. *J. Mol. Cell. Cardiol.* **51**, 554 (2011).

262. Muraski, J. A., Rota, M., Misao, Y., Fransioli, J., Cottage, C., Gude, N., Esposito, G., Delucchi, F., Arcarese, M., Alvarez, R., Siddiqi, S., Emmanuel, G. N., Wu, W., Fischer, K., Martindale, J. J., Glembotski, C. C., Leri, A., Kajstura, J., Magnuson, N., Berns, A., Beretta, R. M., Houser, S. R., Schaefer, E. M., Anversa, P. & Sussman, M. A. Pim-1 regulates cardiomyocyte survival downstream of Akt. *Nat. Med. 2007 1312* **13**, 1467–1475 (2007).

263. Sussman, M. A. Mitochondrial integrity: preservation through Akt/Pim-1 kinase signaling in the cardiomyocyte. *Expert Rev. Cardiovasc. Ther.* **7**, 929 (2009).

264. Dutta, S. & Sengupta, P. Men and mice: Relating their ages. *Life Sci.* **152**, 244–248 (2016).

265. Flurkey, K., Currer, J. M. & Harrison, D. E. Mouse Models in Aging Research. *Mouse Biomed. Res.* **3**, 637–672 (2007).

266. Crowley, G., Kwon, S., Caraher, E. J., Haider, S. H., Lam, R., Batra, P., Melles, D., Liu, M. & Nolan, A. Quantitative lung morphology: semi-automated measurement of mean linear intercept. *BMC Pulm. Med.* **19**, (2019).

267. Gude, N. A., Firouzi, F., Broughton, K. M., Ilves, K., Nguyen, K. P., Payne, C. R., Sacchi, V., Monsanto, M. M., Casillas, A. R., Khalafalla, F. G., Wang, B. J., Ebeid, D., Alvarez, R., Dembitsky, W. P., Bailey, B. A., van Berlo, J. H. & Sussman, M. A. Cardiac c-Kit Biology Revealed by Inducible Transgenesis. *Circ. Res.* CIRCRESAHA.117.311828 (2018) doi:10.1161/CIRCRESAHA.117.311828.

268. Hafemeister, C. & Satija, R. Normalization and variance stabilization of single-cell RNA-seq data using regularized negative binomial regression. *Genome Biol. 2019 201* **20**, 1–15 (2019).

269. Edsgärd, D., Johnsson, P. & Sandberg, R. Identification of spatial expression trends in single-cell gene expression data. *Nat. Methods 2018 155* **15**, 339–342 (2018).

270. Liu, B., Li, Y. & Zhang, L. Analysis and Visualization of Spatial Transcriptomic Data. *Front. Genet.* **12**, 2852 (2022).

271. Fu, R., Gillen, A. E., Sheridan, R. M., Tian, C., Daya, M., Hao, Y., Hesselberth, J. R. & Riemondy, K. A. clustifyr: an R package for automated single-cell RNA sequencing cluster classification. *F1000Research 2020 9223* **9**, 223 (2020).

272. Sun, H., Zhou, Y., Fei, L., Chen, H. & Guo, G. scMCA: A tool to define mouse cell types based on single-cell digital expression. in *Methods in Molecular Biology* vol. 1935 91–96 (Humana Press Inc., 2019).

273. Diz, A. P., Carvajal-Rodríguez, A. & Skibinski, D. O. F. Multiple Hypothesis Testing in Proteomics: A Strategy for Experimental Work. *Mol. Cell. Proteomics* **10**, M110.004374 (2011).